COMPACT MICROSTRIP FILTER DESIGNS AND PHASED ARRAY FOR MULTIFUNCTION RADAR APPLICATIONS

A Dissertation

by

DONG JIN JUNG

Submitted to the Office of Graduate Studies of
Texas A&M University
in partial fulfillment of the requirements for the degree of

DOCTOR OF PHILOSOPHY

May 2012

Major Subject: Electrical Engineering

Compact Microstrip Filter Designs and Phased Array

for Multifunction Radar Applications

COMPACT MICROSTRIP FILTER DESIGNS AND PHASED ARRAY FOR MULTIFUNCTION RADAR APPLICATIONS

A Dissertation

by

DONG JIN JUNG

Submitted to the Office of Graduate Studies of
Texas A&M University
in partial fulfillment of the requirements for the degree of

DOCTOR OF PHILOSOPHY

Approved by:

Chair of Committee,	Kai Chang
Committee Members,	Kamran Entesari
	Laszlo B. Kish
	Kenith E. Meissner
Head of Department,	Costas N. Georghiades

May 2012

Major Subject: Electrical Engineering

ABSTRACT

Compact Microstrip Filter Designs and Phased Array for Multifunction Radar Applications. (May 2012)

Dong Jin Jung, B.S., Soonchunhyang University, Korea;
M.S., Texas A&M University
Chair of Advisory Committee: Dr. Kai Chang

This dissertation mainly discuses various microstrip bandpass filter (BPF) designs. The filter designs include: a coupled line BPF using nonuniform arbitrary image impedances, miniaturized BPF utilizing dumbbell shaped slot resonator (DSSR), BPF employing isosceles triangle shaped patch resonator (ITSPR), BPF with a complimentary split ring resonator (CSRR) and triple-band BPF (TBBPF). In the coupled line BPF designs, a capacitive gap-coupled BPF and parallel coupled line BPF are introduced, where two different arbitrary image impedances are applied for the designs. Based on the proposed equivalent circuit model, the coupled BPF's design equations are derived, and they are validated from comparisons of the calculated and simulated results. For a miniaturized BPF, the DSSR is utilized in the filter design. An equivalent circuit model of the DSSR is also presented and validated through simulations and measurements. The ITSPR is introduced for simple BPF and diplexer designs. The ITSPR's design equations, effective dielectric constant, and fractional bandwidth are discussed, and their validities are demonstrated from electromagnetic

(EM) simulations and measurements. The coupled type complementary split ring resonator (CSRR) is introduced for a compact direct-coupled BPF. The proposed unit cell of the resonator consists of two CSRRs, where gaps of outside rings face each other to achieve a strong cross coupling. For an analysis of the coupled CSRR, an equivalent circuit model is discussed and validated through circuit and EM simulations. Based on the coupled CSRR structure, two-/four- pole direct-coupled BPFs are designed, simulated, and measured. The TBBPF design using admittance inverters are presented. In the TBBPF design, the center frequencies and fractional bandwidths (FBW) of each passband can be adjustable.

Low cost phased array systems operating from 8 to 12 GHz are introduced. A phased array using a piezoelectric transducer (PET) phase shifter is designed and tested. Compared to the phased array using the PET phase shifter, another phased array utilizing 4-bit monolithic microwave integrated circuit (MMIC) phase shifters is demonstrated. Both phased array systems are simple and easy to fabricate.

DEDICATION

This dissertation is dedicated to my parents.

ACKNOWLEDGEMENTS

I would like to express my deepest gratitude to my advisor Dr. Kai Chang for his guidance and support with regards to my graduate studies and research at Texas A&M University. My appreciation goes out to Dr. Kamran Entesari, Dr. Laszlo B. Kish, and Dr. Kenith E. Meissner for serving as committee members for my dissertation. I would also like to thank Mr. Li at Texas A&M University for his helpful support in the development of the projects described in this dissertation. I also want to express my gratitude to my former advisor, Dr. Dal Ahn for his support with regards to my undergraduate studies. Thanks also go to all my friends and EML (Electromagnetic and Microwave Laboratory) colleagues.

Special thanks go to my parents, Mrs. Youngsoon Ahn and Mr. Hoonmo Jung, for their dedication, encouragement, and endless love.

Finally, I thank my God for his guidance and help.

NOMENCLATURE

BPF	Bandpass Filter
CMOS	Complementary Metal Oxide Semiconductor
CSRR	Complimentary Split Ring Resonator
CPW	Coplanar Waveguide
DBBPF	Dual-Band Bandpass Filter
DGS	Defected Ground Structure
DSSR	Dumbbell Shaped Slot Resonator
EM	Electromagnetic
ITSPR	Isosceles Triangle Shaped Patch Resonator
LNA	Low Noise Amplifier
LPF	Lowpass Filter
FBW	Fractional Bandwidth
PA	Power Amplifier
SIW	Substrate Integrated Waveguide
SPDT	Single Pole Double Throw
TBBPF	Triple-Band Bandpass Filter
TBR	Triple-Band Resonator

TABLE OF CONTENTS

Page

CHAPTER

LIST OF FIGURES

FIGURE Page

FIGURE Page

FIGURE Page

FIGURE Page

FIGURE Page

FIGURE Page

FIGURE Page

LIST OF TABLES

CHAPTER I

INTRODUCTION

Nowadays, wireless systems demand multifunction and multiband operation. Personal communication systems, for example, can now provide multiple functions and protocols, e.g., global positioning system (GPS), universal mobile telecommunications system (UMTS), personal communication systems (PCS), within a single RF front end. Throughout the current decade, tunable bandpass filters (BPFs), dual-band and triple-band BPFs have been attractive research topics because they can be favorably utilized in multiband and multifunctional wireless systems.

Most microwave and millimeter-wave filters are now fabricated using metallic waveguide or dielectric planar substrates. Even though a power handing capability and quality (*Q*) factor of the dielectric planar substrate circuits are lower than the metallic waveguide, the dielectric planar substrate has advantages of: easy fabrication, compact size, moderate loss, and high integration capability. For these reasons, the dielectric planar substrate is widely used for the filter designs in RF/microwave and millimeter-wave frequency ranges. Among the planar dielectric substrate, microstrip and coplanar waveguide (CPW) are popularly utilized in circuit designs. In [1], various microstrip filters for RF/microwave applications are well summarized. However, filters using the dielectric planar substrate normally provide a narrow bandwidth, where a fractional bandwidth (FBW) is less than 20 %. Thus, researches of increasing the bandwidth of the

---

This dissertation follows the style of *IEEE Transactions on Microwave Theory and Techniques*.

planar substrate filters have been interested by many researchers.

A BPF is one of the most widely used passive components in RF/microwave systems. Many filters have been developed to meet today's filter requirements including low-insertion loss, compact size, and low cost. Among planar type BPF circuits, parallel/end coupled line BPFs are frequently used because they are relatively simple to design and provide a reasonable performance. Their analysis and design formulas are well described in [1] and [2]. The parallel coupled line structure is particularly efficient for printed-circuit filter designs because it provides relatively large coupling for a given coupled line gap dimension. For these parallel/end coupled line BPF designs, understanding of the following theories are necessitated: image parameters, impedance and admittance inverters, and frequency transformation and impedance scaling from a prototype lowpass filter (LPF).

Including the parallel and end coupled lines, various microstrip resonators can be utilized in BPF designs [3]. An electromagnetic (EM) simulation examines for the external *Q* factors and coupling coefficients between two adjacent resonators. The BPF designs using the external *Q* and coupling coefficients are also based on prototype lowpass filter's element values. In the BPF designs utilizing microstrip resonators, simple microstrip structures are preferable for easy analysis and design. In general, geometrically complex microstrip passive circuits tend to be more dependent on computer aided electromagnetic (EM) simulation. On the other hand, simple circuit structures provide a relatively easy analytical solution. As a result, their performance can be predicted in the design process, and the design methodology can be less dependent on EM simulation.

As the frequency spectrum becomes increasingly crowded, a sharp frequency cutoff is necessary for overall system performance and interference prevention. Generally speaking, filters require several resonator sections to achieve high frequency selectivity. In BPF design, inserting multiple resonator sections makes it difficult to reduce the circuit size and insertion loss. The parallel/end coupled lines are not convenient for BPF miniaturization since each microstrip resonator is separated by several gaps, and the filter's performance is significantly affected by fabrication errors of these gaps. This leads to inevitable errors in design realization which will alter the filter's characteristics. Thus, a simple design which minimizes the number of resonators (and therefore gaps) is preferable for low loss and compact filters, but the filter design should also produce a sharp frequency cutoff. To meet these requirements, BPF designs employing slotted ground structures have been introduced by many researchers.

This dissertation is organized as follows. Section II provides backgrounds which are necessitated in BPF designs using impedance and admittance inverters. Mathematical expressions for an image impedance and image phase constant are also derived. Basic characteristics of the impedance and admittance inverters are introduced. Section III presents parallel and capacitive gap coupled line BPF designs using non-uniform arbitrary image impedances. The two different arbitrary image impedances are employed as the characteristic impedance of a transmission line in the BPF's equivalent circuit models. This ultimately results in the expressions of admittance inverters of the designing BPF. In Section IV, dual-band and triple-band BPF synthesis are introduced. Dual-band and triple-band lumped resonators are employed in the design, and these lumped resonators are realized on microstrip with admittance inverters. Section V presents a complimentary split ring resonator (CSRR) on the ground plane. By utilizing the CSRR, direct coupling BPF is designed. The equivalent circuit model of the CSRR is validated from circuit and EM simulations. Section VI introduces a dumbbell shaped slot resonator (DSSR) and its modeling. Based on the proposed DSSR, tunable DSSR and compact BPF are designed. In Section VII, isosceles triangle shaped patch resonator (ITSPR) is presented with analysis of the ITSPR. Using the proposed ITSPR, a diplexer is designed, simulated, and tested. Section VIII presents phased array system designs. Two different phased arrays for multifunctional radar applications are discussed. For a low cost phased array system, the phased arrays using piezoelectric transducer (PET) phase shifters and monolithic microwave integrated circuit (MMIC) phase shifters are fabricated and tested in the operating frequency band of 8 to 12 GHz.

CHAPTER II

BACKGROUND

2.1 Image Parameters

It is necessary to understand image parameters for analyzing two port microwave circuits. The image viewpoint for the analysis of circuits is a wave viewpoint much the same as the wave viewpoint commonly used for analysis of RF/microwave transmission lines [1]. In this section, two important image parameters, image impedance and image propagation constant are introduced based on two port circuit theory. In general, image impedance of a two-port network is defined as the impedance seen looking in to Port 1 (or Port 2) when Port 2 (or Port 1) is terminated with the image impedance of Port 2 (or Port1). The image impedances of Port 1 and 2 are not equal if the network is not symmetrical with respect to the ports. Fig. 2-1 illustrates infinite chain of identical networks used for defining image impedances and the image propagation function.

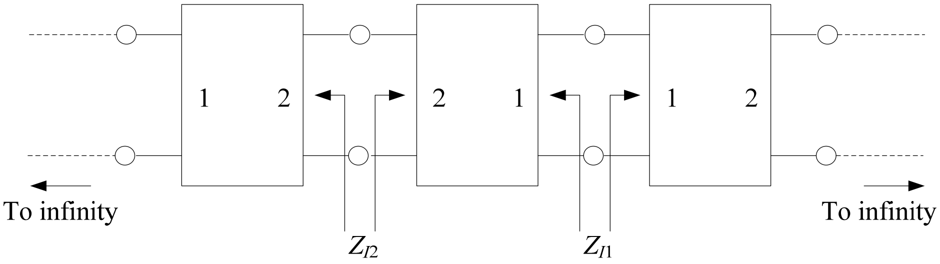

Fig. 2-1. Infinite chain of identical two-port networks used for defining image impedances and the image propagation function.

In Fig. 2-1, the two port network is assumed to be unsymmetrical with different impedance characteristics at Port 1 and Port 2. Since the chain of networks extends to infinity in each direction, the same impedance Z_{I1} (or Z_{I2}) is seen looking both left and right at a junction of the two ports. Therefore, there is no reflection of a wave propagating through junction, i.e., all perfectly matched between junctions. An expression for the image impedance can easily be derived using circuit parameters. Fig. 2-2 shows two networks are cascaded with terminated load impedance (Z_L), where Z_L is equal to the image impedance, Z_{I1}.

Fig. 2-2 (a) represents a two cascaded network. In reality, the number of networks could be increased, and simplified as Fig. 2-2 (b). In Fig. 2-2 (b), voltage and current of the resulting network can ne expressed as:

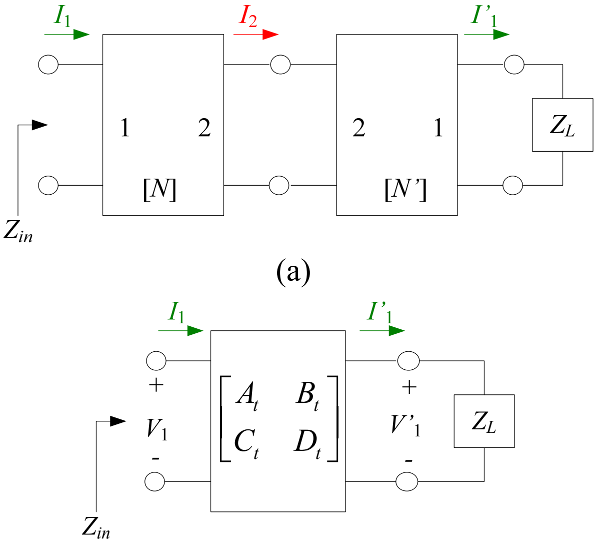

(a)

(b)

Fig. 2-2. Two cascaded networks with terminated load impedance, Z_L=Z_{I1}; (a) cascaded two port networks and (b) equivalent network.

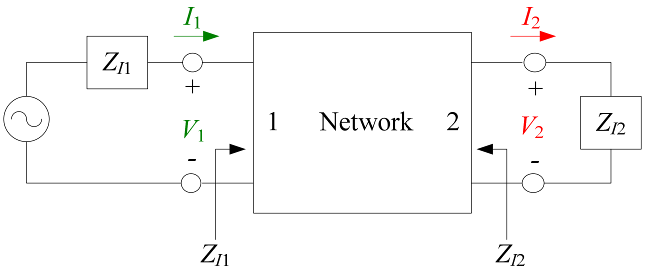

Fig. 2-3. Network terminated with image impedances at each port.

$$\begin{bmatrix} V_1 \\ I_1 \end{bmatrix} = \begin{bmatrix} A_t & B_t \\ C_t & D_t \end{bmatrix} \begin{bmatrix} V_1' \\ I_1' \end{bmatrix} \tag{2.1}$$

Then, the input impedance, Z_{in} is expressed as:

$$Z_{in} = \frac{V_1}{I_1} = \frac{A_t V_1' + B_t I_1'}{C_t V_1' + D_t I_1'} = \frac{A_t Z_L + B_t}{C_t Z_L + D_t} = \frac{A_t Z_{I1} + B_t}{C_t Z_{I1} + D_t} \tag{2.2}$$

The image impedances at Port 1 and 2 can be derived from Fig. 2-3. Input voltage and current in Fig. 2-3 are written as:

$$. \; V_1 = AV_2 + BI_2 \tag{2.3.a}$$

$$I_1 = CV_2 + DI_2 \tag{2.3.b}$$

Then, image impedance, Z_{I1} can be expressed:

$$Z_{I1} = \frac{V_1}{I_1} = \frac{AV_2 + BI_2}{CV_2 + DI_2} = \frac{AZ_{I2} + B}{CZ_{I2} + D} \tag{2.4}$$

Inverse matrix of Fig. 2-3 is written:

$$\begin{bmatrix} V_2 \\ I_2 \end{bmatrix} = \begin{bmatrix} A & B \\ C & D \end{bmatrix}^{-1} \begin{bmatrix} V_1 \\ I_1 \end{bmatrix} = \frac{1}{AD - BC} \begin{bmatrix} D & -B \\ -C & A \end{bmatrix} \begin{bmatrix} V_1 \\ I_1 \end{bmatrix} \tag{2.5}$$

Since *AD*-*BC*=1 for a reciprocal network, image impedance, Z_{I2} at Port 2 can be shown as:

$$Z_{I2} = -\frac{V_2}{I_2} = -\frac{DV_1 - BI_1}{-CV_1 + AI_1} = \frac{-DV_1 + BI_1}{-CV_1 + AI_1} \tag{2.6}$$

In Fig. 2-3, looking from Port 2 results in a reverse current direction of I_1, and this reverse current direction validates Z_{I1}=-(V_1/I_1). From this condition, image impedance in (2.6) can be rewritten as:

$$Z_{I2} = \frac{DZ_{I1} + B}{CZ_{I1} + A} \tag{2.7}$$

From (2.4) and (2.7), Z_{I1} and Z_{I2} can be presented as:

$$Z_{I1} = \frac{A\left(\dfrac{DZ_{I1} + B}{CZ_{I1} + A}\right) + B}{C\left(\dfrac{DZ_{I1} + B}{CZ_{I1} + A}\right) + D} = \sqrt{\frac{AB}{CD}} \tag{2.8.a}$$

$$Z_{I2} = \frac{A\left(\dfrac{DZ_{I2} + B}{CZ_{I2} + A}\right) + B}{C\left(\dfrac{DZ_{I2} + B}{CZ_{I2} + A}\right) + D} = \sqrt{\frac{BD}{AC}} \tag{2.8.b}$$

The expressions in (2.8.a) and (2.8.b) show the image impedance of two port network.

Image propagation constant is also one of the important image parameters, which defines the transmission through the network. From (2.5), voltage and current of reciprocal network (AD-BC=1), can be presented as:

$$V_2 = DV_1 - BI_1 = \left(D - B\frac{1}{Z_{I1}}\right)V_1 \tag{2.9.a}$$

$$I_2 = -CV_1 + AI_1 = \left(-CZ_{I1} + A\right)I_1 \tag{2.9.b}$$

Using (2.8.a) and (2.8.b), the expressions in (2.9.a) and (2.9.b) can be written as:

$$\frac{V_2}{V_1} = D - B\frac{\sqrt{CD}}{\sqrt{AB}} = \frac{\sqrt{D}}{\sqrt{A}}\left(\sqrt{AD} - \sqrt{BC}\right) \tag{2.10.a}$$

$$\frac{I_2}{I_1} = A - C\frac{\sqrt{AB}}{\sqrt{CD}} = \frac{\sqrt{A}}{\sqrt{D}}\left(\sqrt{AD} - \sqrt{BC}\right) \tag{2.10.b}$$

The equations in (2.10.a) and (2.10.a) are defined as transfer constant from Port 1 to Port 2. Similarly, from (2.3.a) and (2.3.b), the transfer constant from Port 2 to Port 1 can be obtained as:

$$\frac{V_1}{V_2} = \sqrt{\frac{A}{D}}\left(\sqrt{AD} + \sqrt{BC}\right) \tag{2.11.a}$$

$$\frac{I_1}{I_2} = \sqrt{\frac{D}{A}}\left(\sqrt{AD} + \sqrt{BC}\right) . \tag{2.11.b}$$

From (2.10) and (2.11), wave propagation functions are defined as:

$$\sqrt{AD} - \sqrt{BC} = e^{-\gamma} \tag{2.12.a}$$

$$\sqrt{AD} + \sqrt{BC} = e^{\gamma} . \tag{2.12.b}$$

where $\gamma=\alpha+j\beta$. (2.12.a) represents propagation from Port 1 to Port 2, and (2.12.b) from Port 2 to Port 1. Since $e^{-\gamma} = \cosh\gamma - \sinh\gamma$ and $e^{\gamma} = \cosh\gamma + \sinh\gamma$, one can immediately determine the expressions: $\cosh\gamma = \sqrt{AD}$ and $\sinh\gamma = \sqrt{BC}$. From this, the propagation constant can be derived as:

$$\gamma = \ln\left(\sqrt{AD} + \sqrt{BC}\right) = \tanh^{-1}\left(\sqrt{\frac{BC}{AD}}\right) . \tag{2.13}$$

The image propagation constant can be expressed in terms of voltage and current of a network. (2.11.a) can also be written as:

$$\frac{V_1}{V_2}=\sqrt{\frac{P_1}{P_2}}e^{\gamma}=\sqrt{\frac{I_1V_1}{I_2V_2}}e^{\gamma}=\sqrt{\frac{I_1\left(I_1Z_{I1}\right)}{I_2\left(I_2Z_{I2}\right)}}e^{\gamma} \tag{2.14}$$

where I_1=I_2. Then, (2.14) can be rewritten as:

$$e^{\gamma}=\frac{V_1}{V_2}\sqrt{\frac{Z_{I2}}{Z_{I1}}} \tag{2.15}$$

From (2.15), the image propagation constant (γ) in (2.13) can be shown as:

$$\gamma=\alpha+j\beta=\ln\left(\sqrt{\frac{V_1I_1}{V_2I_2}}\right) \tag{2.16}$$

This image propagation constant defines the transmission through the network as indicated in (2.14), only if the terminations mach the image impedances.

2.2 Image Parameters for Practical Circuit Structures

In this section, image parameters of some useful two port networks are introduced. These networks are especially necessary to understand filter designs using J or K inverters.

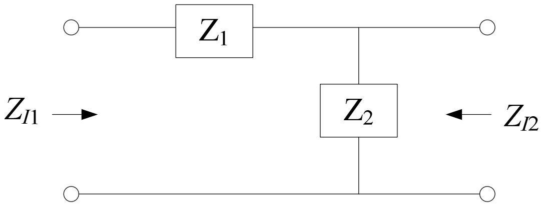

Fig. 2-4. An *L*-type network.

Fig. 2-4 shows an L-type network. From previous section, image impedance of a two port network can be derived as (2.8.a) and (2.8.b). *ABCD* matrix of Fig. 2-4 is presented as:

$$\begin{bmatrix} A & B \\ C & D \end{bmatrix} = \begin{bmatrix} 1+\frac{Z_1}{Z_2} & Z_1 \\ \frac{1}{Z_2} & 1 \end{bmatrix} \tag{2.17}$$

Then, Z_{I1} and Z_{I2} of Fig. 2-4 can be written as:

$$Z_{I1} = \sqrt{\frac{AB}{CD}} = \sqrt{Z_1\left(Z_1+Z_2\right)} \tag{2.18}$$

$$Z_{I2} = \sqrt{\frac{BD}{AC}} = \frac{Z_1 Z_2}{\sqrt{Z_1(Z_1+Z_2)}} \tag{2.19}$$

(2.18) and (2.19) represent the image impedances of L type network. From (2.13), image propagation constant, γ can be determined as:

$$\gamma = \coth^{-1}\sqrt{\frac{AD}{BC}} = \coth^{-1}\sqrt{1+\frac{Z_2}{Z_1}} \tag{2.20}$$

Fig. 2-5 depicts a symmetrical T-type network which consists of two different impedances. *ABCD* matrix of Fig. 2-5 is determined as:

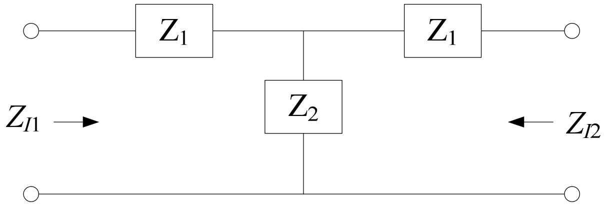

Fig. 2-5. A symmetrical T-type network.

$$\begin{bmatrix} A & B \\ C & D \end{bmatrix} = \begin{bmatrix} 1+\dfrac{Z_1}{Z_2} & Z_1\left(1+\dfrac{Z_1}{Z_2}\right)+Z_1 \\ \dfrac{1}{Z_2} & 1+\dfrac{Z_1}{Z_2} \end{bmatrix} \tag{2.21}$$

Since Fig. 2-5 is a symmetrical network, image impedance can be written as:

$$Z_{I1} = Z_{I2} = \sqrt{\frac{AB}{CD}} = \sqrt{\frac{BD}{AC}} = \sqrt{Z_1\left(Z_1+2Z_2\right)} \tag{2.22}$$

From two port network, the condition, $\cosh\gamma = \sqrt{AD}$ has been derived in the previous section. This condition leads to:

$$\cosh\gamma = \sqrt{AD} = \frac{e^{\gamma}+e^{-\gamma}}{2} = 1+\frac{Z_1}{Z_2} \tag{2.23}$$

Then, the image propagation constant of the T type network can simply be derived from (2.23):

$$\gamma = 2\sinh^{-1}\sqrt{\frac{Z_1}{2Z_2}} \tag{2.24}$$

Fig. 2-6 illustrates a symmetrical π-type network with admittance notations. *ABCD* matrix of Fig. 2-6 is obtained as:

$$\begin{bmatrix} A & B \\ C & D \end{bmatrix} = \begin{bmatrix} 1+\dfrac{Y_1}{Y_2} & \dfrac{1}{Y_2} \\ 2Y_1+\dfrac{Y_1^2}{Y_2} & 1+\dfrac{Y_1}{Y_2} \end{bmatrix} \tag{2.25}$$

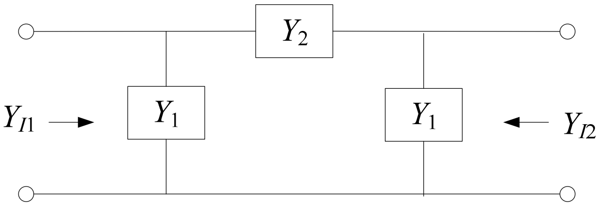

Fig. 2-6. A symmetrical π-type network.

In the similar manner shown in Fig. 2-5, image admittance can be found to be:

$$Y_{I1} = Y_{I2} = \sqrt{\frac{CD}{AB}} = \sqrt{\frac{AC}{BD}} = \sqrt{2Y_1Y_2 + Y_1^2} \tag{2.26}$$

The image propagation constant of Fig. 2-6 can also be determined as:

$$\gamma = 2\sinh^{-1}\sqrt{\frac{Y_1}{2Y_2}} \tag{2.27}$$

2.3 Special Image Properties of Lossless Network

In order to consider a network itself without load, z- and y-parameters can be utilized to express image parameters. When considering Fig. 2-3, it is assumed that the image impedances at each ends are not connected to the network. In this case, physically, z_{11} (z_{22}) is the input impedance at Port 1 (Port 2) when Port 2 (Port1) is open circuited. Similarly, y_{11} (y_{22}) is the admittance at Port 1 (Port 2) when Port 2 (Port1) is short-circuited. The z- and y-parameters can be expressed in terms of *ABCD* parameters, $z_{11}=A/C$, $y_{11}=D/B$, $z_{22}=D/C$, and $y_{22}=A/B$. From (2.8.a) and (2.8.b), image impedances can be rewritten as:

$$Z_{I1} = \sqrt{\frac{AB}{CD}} = \sqrt{\frac{z_{11}}{y_{11}}} \tag{2.28}$$

$$Z_{I2} = \sqrt{\frac{BD}{AC}} = \sqrt{\frac{z_{22}}{y_{22}}} \tag{2.29}$$

The equations in (2.28) and (2.29) imply that the image impedances derived from perfect matching condition of a network can be expressed using z- and y-parameters. This ultimately results in more practical method to measure any network.

From (2.13), the image propagation constant can be written as:

$$\gamma = \alpha + j\beta = \coth^{-1}\left(\sqrt{\frac{AD}{BC}}\right) = \coth^{-1}\sqrt{z_{11}y_{11}} \ . \tag{2.30}$$

For a lossless network, complex frequency, p can be assumed to be $p=j\omega$, which is pure sinusoid [1]. z_{11} and y_{11} can be expressed as:

$$z_{11} = j(X_{oc})_1 \tag{2.31}$$

$$y_{11} = \frac{1}{j\left(X_{sc}\right)_1} \tag{2.32}$$

where $j(X_{oc})_1$ is the impedance at Port 1 of the network with Port 2 open circuited, and $j(X_{sc})_1$ is the impedance at Port 1 with Port 2 short circuited. From (2.31) and (2.32), (2.28) and (2.30) can be written as:

$$Z_{I1} = \sqrt{-\left(X_{oc}\right)_1 (X_{sc})_1} \tag{2.33}$$

$$\gamma = \alpha + j\beta = \coth^{-1}\sqrt{\frac{(X_{oc})_1}{(X_{sc})_1}} \ . \tag{2.34}$$

Since the inverse, hyperbolic cotangent function in (2.34) is a multivalued function, (2.34) can be expressed as:

$$\gamma = \alpha + j\beta = \coth^{-1}\sqrt{\frac{(X_{oc})_1}{(X_{sc})_1}} + jn\pi \ . \tag{2.35}$$

When considering the image impedance in (2.33) and image phase constant in (2.35), two cases, i.e., passband and stopband, could be considered.

In passband, the expression in (2.33) must be real and positive, which means that $(X_{oc})_1$ and $(X_{sc})_1$ have opposite signs. At the same time, image impedance at Port 2 can be presented as:

$$Z_{I2} = \sqrt{-\left(X_{oc}\right)_2 (X_{sc})_2} \tag{2.36}$$

(2.36) must also be real and positive. Under the passband condition, (2.35) yields attenuation constant of zero (α=0) and propagation constant of:

$$\beta = -\cot^{-1}\sqrt{\left|\frac{(X_{oc})_1}{(X_{sc})_1}\right|} \tag{2.37}$$

For stopband, $(X_{oc})_1$ and $(X_{sc})_1$ have the same sign. Then, (2.33) and (2.36) are both purely imaginary, and they can be rewritten as:

$$Z_{I1} = \sqrt{-\left(X_{oc}\right)_1 (X_{sc})_1} = jX_{I1} \tag{2.38}$$

$$Z_{I2} = \sqrt{-\left(X_{oc}\right)_2 (X_{sc})_2} = jX_{I2} \tag{2.39}$$

In (2.38) and (2.39), X_{I1} and X_{I2} must have positive slopes versus frequency according to Foster's reactance theorem, which states that the reactance of a passive and lossless two port network always monotonically increases with frequency. If $(X_{oc})_1 > (X_{sc})_1$, (2.35) is used to obtain α and β [1]:

$$\alpha = \coth^{-1}\sqrt{\frac{(X_{oc})_1}{(X_{sc})_1}} \tag{2.40}$$

$$\beta = n\pi \tag{2.41}$$

If $(X_{oc})_1 < (X_{sc})_1$, the equivalent form of (2.35), which is shown in (2.41), is used to determine the α and β:

$$\gamma = \alpha + j\beta = \tanh^{-1}\sqrt{\frac{(X_{oc})_1}{(X_{sc})_1}} + j(2n-1)\frac{\pi}{2}\ . \tag{2.42}$$

$$\alpha = \tanh^{-1}\sqrt{\frac{(X_{oc})_1}{(X_{sc})_1}} \tag{2.43}$$

$$\beta = (2n-1)\frac{\pi}{2} \tag{2.44}$$

where α and β are in nepers and radians, respectively.

In fact, for the case of a uniform transmission line, the characteristic impedance of the line is also image impedance, and if γ is a propagation constant per unit length, then γl is the image propagation function for a line of length, l [1].

2.4 Inverter Theory

The concept of the image impedance and admittance shown in the previous sections can be applied to explain an inverter. In this section, the impedance and admittance inverters are discussed. K and J represent the impedance and admittance inverters, respectively. The inverters have the following characteristics: image impedance (or image admittance) is real in the operating frequency range, and their image phase is odd multiple of $\pm\pi/2$. Thus, if any two port network satisfies above characteristics, the network could be considered as the inverter. These characteristics can automatically be achieved if a symmetrical network shows:

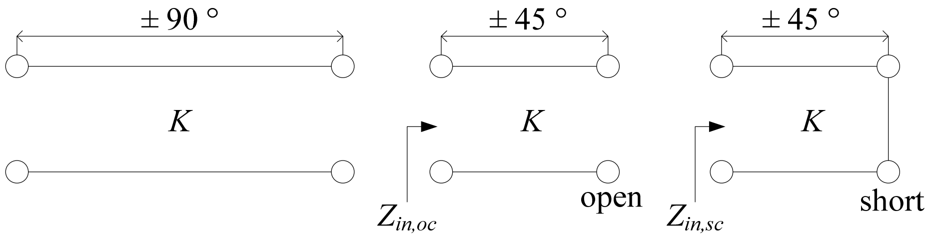

Fig. 2-7. A quarter-wavelength transmission line with open and short conditions.

$$\left(X_{1/2}\right)_{oc} = -\left(X_{1/2}\right)_{sc} \; . \tag{2.45}$$

where $(X_{1/2})_{oc}$ is the input reactance of the circuit when cut in half and the cut wires are left open-circuited, while $(X_{1/2})_{sc}$ is the corresponding reactance when the cut wires are shorted together. For example, the quarter-wavelength transmission line is the simplest form of inverters. Fig. 2-7 shows a quarter-wavelength transmission line with open and short conditions, where the line characteristic impedance is a real value (*K*). In Fig. 2-7, the input impedances of open and short circuited line can be written as:

$$Z_{in,oc} = -jK\cot(45°) = -jK \; . \tag{2.46}$$

$$Z_{in,oc} = jK\tan(45°) = jK \; . \tag{2.47}$$

Since the two equations in (2.46) and (2.47) satisfy the condition in (2.45), a quarter-wavelength transmission line can be used for an inverter.

K inverter operated like a quarter-wavelength transmission line with the characteristic impedance *K* (ohm) at all frequency and may have an image phase shift of ± 90º. *J* inverter also operates like a quarter-wavelength transmission line with the characteristic admittance J (mho) at all frequency and may have an image phase shift of

± 90º [1]. Figs. 2-8 (a) and (b) illustrate the basic characteristics of *K* and *J* inverters. In Figs. 2-8 (a) and (b), input impedance and admittance are expressed as:

$$Z_{in,k} = \frac{K^2}{Z_L} \ . \tag{2.48}$$

$$Y_{in,j} = \frac{J^2}{Y_L} \ . \tag{2.49}$$

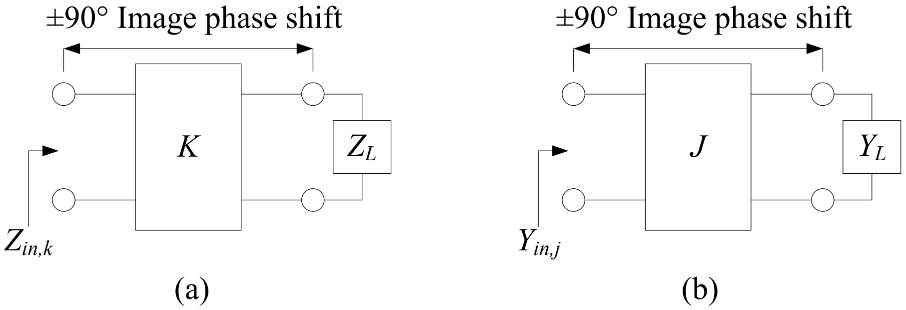

Fig. 2-8. Characteristics of (a) impedance and (b) admittance inverters.

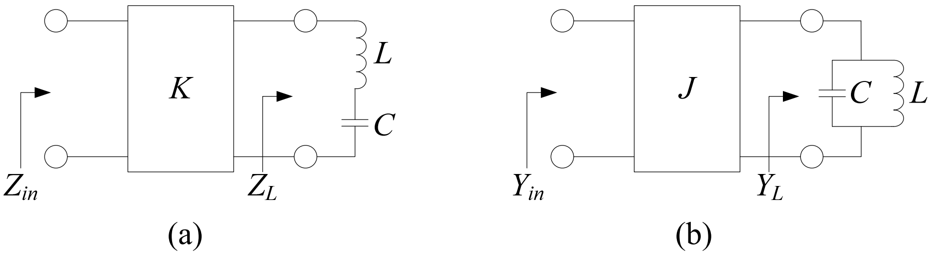

Fig. 2-9. Inverters with lumped *LC* resonators; (a) *K* and (b) *J* inverters.

Figs. 2-9 (a) and (b) depict *K* and *J* inverters with lumped *LC* resonators. In Fig. 2-9 (a), input impedance, Y_{in} can be written as:

$$Y_{in} = \frac{1}{Z_{in}} = \frac{Z_L}{K^2} = j\omega\frac{L}{K^2} + \frac{1}{j\omega C K^2} = j\omega C_T + \frac{1}{j\omega L_T} \tag{2.50}$$

where $C_T = L/K^2$ and $L_T = K^2C$. The equation in (2.50) implies that a series *LC* resonator in shunt can be seen as a parallel *LC* resonator in series. In Fig. 2-9 (b), input impedance, Z_{in} can be written as:

$$Z_{in} = \frac{1}{Y_{in}} = \frac{Y_L}{J^2} = j\omega\frac{C}{J^2} + \frac{1}{j\omega LJ^2} = j\omega L_T + \frac{1}{j\omega C_T} \tag{2.51}$$

where $L_T = C/J^2$ and $C_T = \mathrm{L}J^2$. The equation in (2.51) implies that a parallel *LC* resonator in shunt can be seen as a series *LC* resonator in series. By utilizing the inverters, the number of lumped *LC* resonators can be reduced, which ultimately provide an easy circuit realization with a distributed element.

The inverters can be realized by two different ways; one is a quarter-wavelength transmission line and the other is a lumped type circuit. Although the inverter properties are relatively narrow-band in nature, a quarter-wavelength line can be used satisfactorily as impedance or admittance inverter in narrow band filters [1]. The inverters between the resonators are essential in order to obtain a multiple-resonance response if all of the resonators are the same type, i.e., series type resonance or shunt type resonance. If resonators are connected without the inverters, the resonators would operate like a single series resonator or single shunt resonator with a slope parameter equal to the sum of the slop parameters of the individual resonators.

Except a quarter-wavelength transmission line, there are some other lumped circuits which operate as inverters. They provide an image phase shift of odd multiple of ± 90° and real image impedance over a much wider bandwidth than does a quarter-wavelength transmission line.

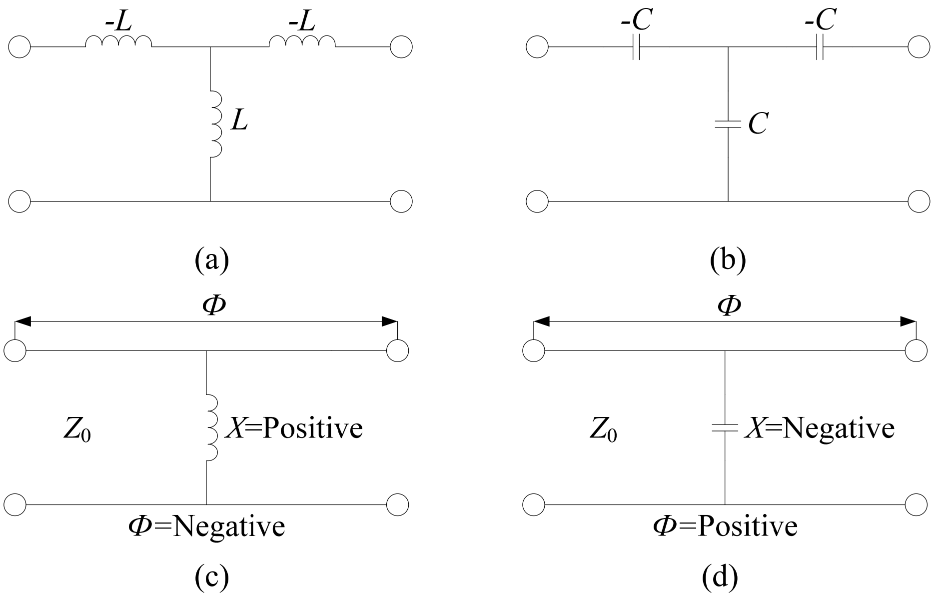

Fig. 2-10. Lumped circuits for *K* inverters.

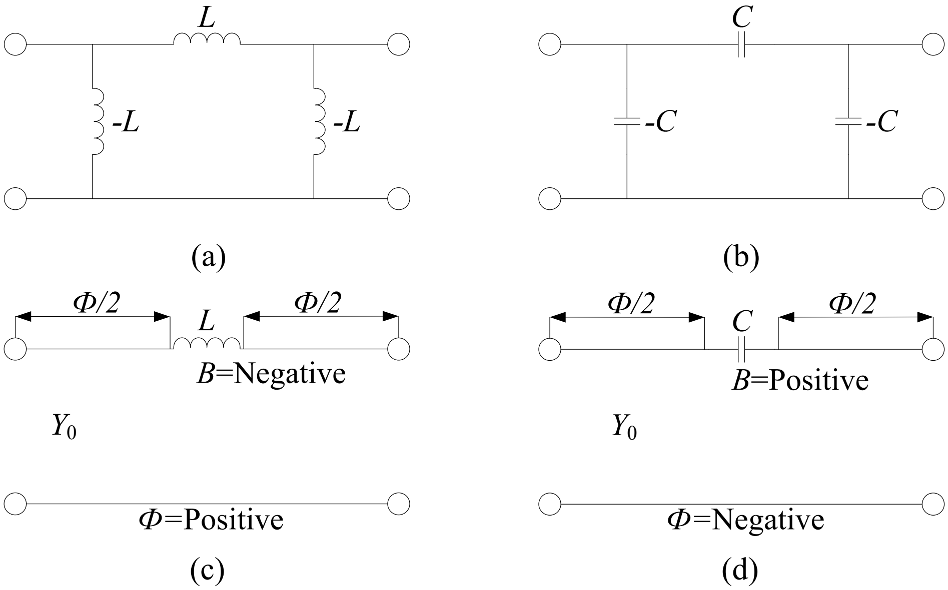

Fig. 2-11. Lumped circuits for *J* inverters.

Fig. 2-10 shows lumped circuits which are particularly useful as *K* inverters. The image impedances (*K*) for Figs. 2-10 (a)-(d) can simply be derived using the image parameter theory presented in the previous sections.

The image impedance, *K* of Fig. 2-10 (a) is:

$$K = \omega L \ . \tag{2.52}$$

The image impedance, *K* of Fig. 2-10 (b) is:

$$K = \frac{1}{\omega C} \ . \tag{2.53}$$

Figs. 2-10 (a) and (b) are particularly useful in circuits where the negative *L* and *C* can be absorbed into adjacent positive series elements of the same type so as to give a resulting circuit having all positive elements [1].

The image impedance, *K* and line length of Figs. 2-10 (c) and (d) is:

$$K = Z_0 \tan\left|\frac{\phi}{2}\right| \ . \tag{2.54}$$

$$\phi = -\tan^{-1}\frac{2X}{Z_0} \ . \tag{2.55}$$

where $\left|\frac{X}{Z_0}\right| = \frac{K}{Z_0\left\{1-\left(\frac{K}{Z_0}\right)^2\right\}}$.

Figs. 2-10 (c) and (d) are particularly useful in circuits where the line of positive or negative electrical length ϕ can be added or subtracted from adjacent lines of the same impedance. Figs. 2-10 (a) and (c) produce -90º image phase shift, and Figs. 2-10 (b) and (d) provide +90º image phase shift. The impedance inverter parameter *K* indicated in the Figs. 2-10 (a)-(d) is equal to the image impedance of the inverter network and is analogous to the characteristic impedance of a transmission line [1]. The mathematical derivations of Fig. 2-10 (a) and (c) are shown in Appendix I.

Fig. 2-11 presents lumped circuits which are particularly useful as J inverters. The image admittance (J) for Figs. 2-11 (a)-(d) can simply be derived using the image parameter theory presented in the previous sections.

The image admittance, J of Fig. 2-11 (a) is:

$$J = \frac{1}{\omega L} \ . \tag{2.56}$$

The image admittance, J of Fig. 2-11 (b) is:

$$J = \omega C \ . \tag{2.57}$$

The image admittance, J and line length of Figs. 2-11 (c) and (d) is:

$$J = Y_0 \tan\left|\frac{\phi}{2}\right| \ . \tag{2.58}$$

$$\phi = -\tan^{-1}\frac{2B}{Y_0} \ . \tag{2.59}$$

where $\left|\frac{B}{Y_0}\right| = \dfrac{J}{Y_0\left\{1-\left(\frac{J}{Y_0}\right)^2\right\}}$.

The expressions in (2.56)-(2.59) can be derived in a similar manner shown in Appendix A.

CHAPTER III

BPF DESIGNS USING NON-UNIFORM ARBITRARY IMAGE IMPEDANCES*

3.1 Introduction

A filter is one of the most essential components in RF/microwave system since it controls overall signal flows within a certain frequency band. Among planar type band-pass filter (BPF) circuits, parallel/end coupled line BPFs are frequently used because they are relatively simple to design and provide a reasonable performance. Their analysis and design formulas are well described in [4] and [5]. The parallel coupled line structure is particularly efficient for printed-circuit filter designs because it provides relatively large coupling for a given coupled line gap dimension [1]. However, a dielectric constant for the designs of these coupled type BPFs should be selected with care to obtain suitable filter dimensions which are reasonable for a conventional low resolution fabrication method. For an example, in the conventional parallel coupled line BPF design, the higher dielectric constant is used, the narrower coupled line width is acquired. On the other hand, in a low dielectric constant case, the coupled line's gap dimension can be too narrow to be fabricated. These narrow line widths and gaps are sometime not appropriate for the conventional low resolution etching process. Thus, an alternative design technique to adjust the line widths and gap dimensions is necessary.

In this chapter, a new design method using arbitrarily selected uniform or non-

---

*Parts of this chapter are reprinted with permission from D.-J. Jung and K. Chang, "Novel capacitive gap-coupled bandpass filter using non-uniform arbitrary image impedance," *Progress In Electromagnetics Research C*, vol. 26, pp. 111-121, 2012. Copyright 2012 EMW.

uniform image impedances is introduced for a parallel coupled line BPF, capacitive gap coupled line BPF, and hairpin BPF. Slope parameters for resonator's image impedance lines are derived from proposed BPF equivalent circuits. Using the slope parameters, equations for admittance inverters are also introduced. The proposed design methodology and equations are validated through simulation and measurement. The circuits are fabricated on Rogers 5880 with a substrate thickness of 0.508 mm and a dielectric constant of 2.2, and they are measured using an HP 8510 vector network analyzer.

3.2 Parallel Coupled Line BPF Using Nonuniform Arbitrary Image Impedances

The equivalent circuit model of a single section parallel coupled line in Fig. 3-1 (a) can be shown as Fig. 3-1 (b) under the condition of $\theta=\pi/2$. Z_{oe} and Z_{oo} in Fig. 3-1 (a) are the even and odd mode characteristic impedances, respectively. In Fig. 3-1 (b), J is the characteristic admittance of admittance inverter, and Y is the admittance of each line. Fig. 3-2 illustrates the proposed parallel coupled BPF using non-uniform image impedances (Z_1 and Z_2). These image impedances (Z_1 and Z_2) are arbitrarily chosen by a designer, where Z_1 could be greater than Z_2 or less than Z_2. Based on the well known theory in Figs. 3-1 (a) and (b), the equivalent circuit of the proposed parallel coupled BPF can be presented as Fig. 3-3. If a frequency is close to the resonant frequency ($\omega\approx\omega_o$), Y_a in Fig. 3-3 can be rewritten as (3.1).

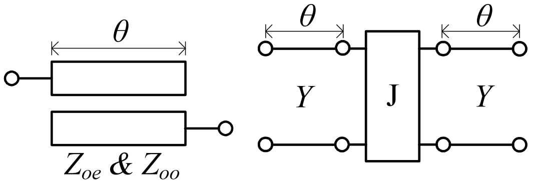

(a) (b)

Fig. 3-1 Microstrip (a) parallel coupled line and (b) its equivalent circuit.

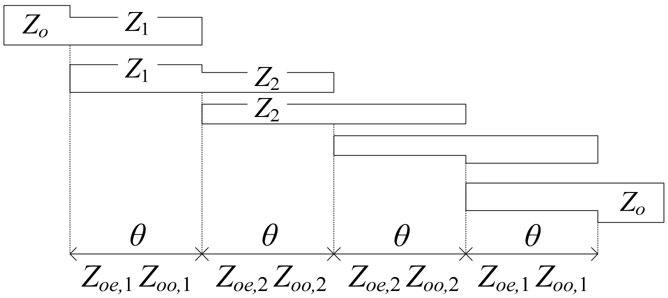

Fig. 3-2. Parallel coupled line BPF with non-uniform image impedances (Z_1 and Z_2).

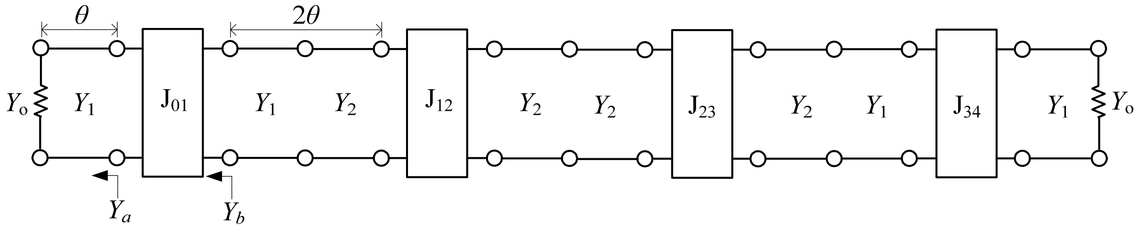

Fig. 3-3. Equivalent circuit model of the proposed parallel coupled line BPF using non-uniform image impedances.

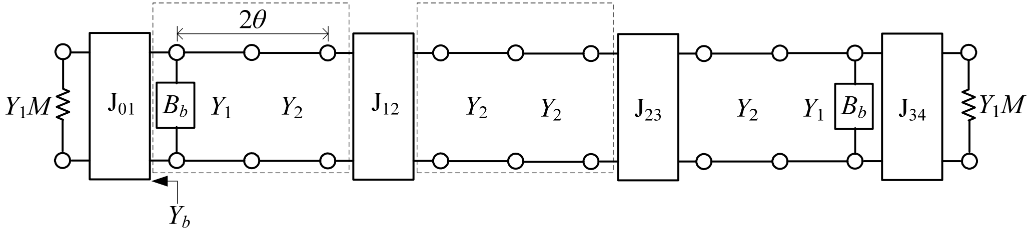

Fig. 3-4. Modified equivalent circuit model of Fig. 3-3.

The expression in (3.1) leads to (3.4) by substituting (3.2) and (3.3). Using (3.4), the input admittance, Y_b, shown in Fig. 3-3 can be expressed as (3.5). Thus, B_b in Fig. 3-4 can be derived as (3.6).

$$Y_a = Y_1 \left. \frac{\dfrac{Y_1}{Y_o} + j\dfrac{\pi}{2}\left(\dfrac{\omega-\omega_o}{\omega_o}\right)}{1 + j\dfrac{\pi}{2}\dfrac{Y_1}{Y_o}\left(\dfrac{\omega-\omega_o}{\omega_o}\right)} \right|_{\omega\approx\omega_o} \tag{3.1}$$

$$M = \frac{Y_1}{Y_o} \tag{3.2}$$

$$N = \frac{\pi}{2}\left(\frac{\omega-\omega_o}{\omega_o}\right) \tag{3.3}$$

$$Y_a = \frac{Y_1^2}{Y_o} + jY_1 N\left(1 - M^2\right) \tag{3.4}$$

$$Y_b = \frac{J_{01}^2}{Y_1 M}\left\{1 + jN\left(M - \frac{1}{M}\right)\right\} \tag{3.5}$$

$$B_b = \frac{J_{01}^2 N}{Y_1}\left(1 - \frac{1}{M^2}\right) \tag{3.6}$$

Since the expression in (3.5) is similar to (3.4), the equivalent circuit in Fig. 3-3 can be transformed as in Fig. 3-4. In order to obtain susceptances of the transmission line sections in Fig. 3-4, the first section can be modeled as in Fig. 3-5 (a) and the second section in Fig. 3-5 (b). The input admittances in Fig. 3-5 (a) and (b) are then written as (3.7)-(3.9). Thus, B_{r1} can be obtained by adding B_b, B_1, and B_2. B_{r2} can also be determined from (3.9).

$$Y_{in,1} = jY_1 \frac{\pi}{2}\left(\frac{\omega - \omega_o}{\omega_o}\right) = jB_1(\omega)\Big|_{\omega \approx \omega_o} \tag{3.7}$$

$$Y_{in,2} = jY_2 \frac{\pi}{2}\left(\frac{\omega - \omega_o}{\omega_o}\right) = jB_2(\omega)\Big|_{\omega \approx \omega_o} \tag{3.8}$$

$$Y_{in} = jY_2 \pi\left(\frac{\omega - \omega_o}{\omega_o}\right) = jB_{r2}(\omega)\Big|_{\omega \approx \omega_o} \tag{3.9}$$

The slope parameters of B_{r1} and B_{r2} can be expressed as (3.10) and (3.11), respectively.

$$b_{r1} = \frac{\omega_o}{2}\frac{dB_{r1}}{d\omega}\bigg|_{\omega=\omega_o} = \frac{\pi Y_1}{4}\left[\frac{J_{01}^2}{Y_1^2}\left(1 - \frac{1}{M^2}\right) + \frac{Y_2}{Y_1} + 1\right] \tag{3.10}$$

$$b_{r2} = \frac{\omega_o}{2}\frac{dB_{r2}}{d\omega}\bigg|_{\omega=\omega_o} = \frac{\pi}{2}Y_2 \tag{3.11}$$

Using (3.10) and (3.11), the proposed J-inverter expressions can be presented as (3.12) and (3.13).

$$J_{01} = J_{34} = \sqrt{\frac{\omega_{FB} Y_1 M \pi \left(Y_1 + Y_2\right)}{4 g_0 g_1 - \omega_{FB} \pi \left(M - 1/M\right)}} \tag{3.12}$$

$$J_{12} = J_{23} = \sqrt{\frac{\omega_{FB}^2}{g_1 g_2}\left[\frac{\pi^2 Y_1 Y_2}{8}\left\{\frac{J_{01}^2}{Y_1^2}\left(1 - \frac{1}{M^2}\right) + \frac{Y_2}{Y_1} + 1\right\}\right]} \tag{3.13}$$

where $\omega_o = \dfrac{\omega_2 + \omega_1}{2}$ and $\omega_{FB} = \dfrac{\omega_2 - \omega_1}{\omega_o}$.

Once the admittance inverters are found, even and odd mode characteristic impedances of the parallel coupled lines can be calculated using (3.14) and (3.15), respectively.

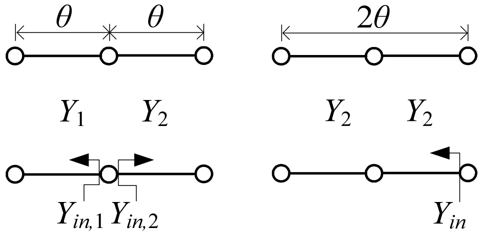

(a) (b)

Fig. 3-5. Transmission lines of (a) the first and (b) the second section.

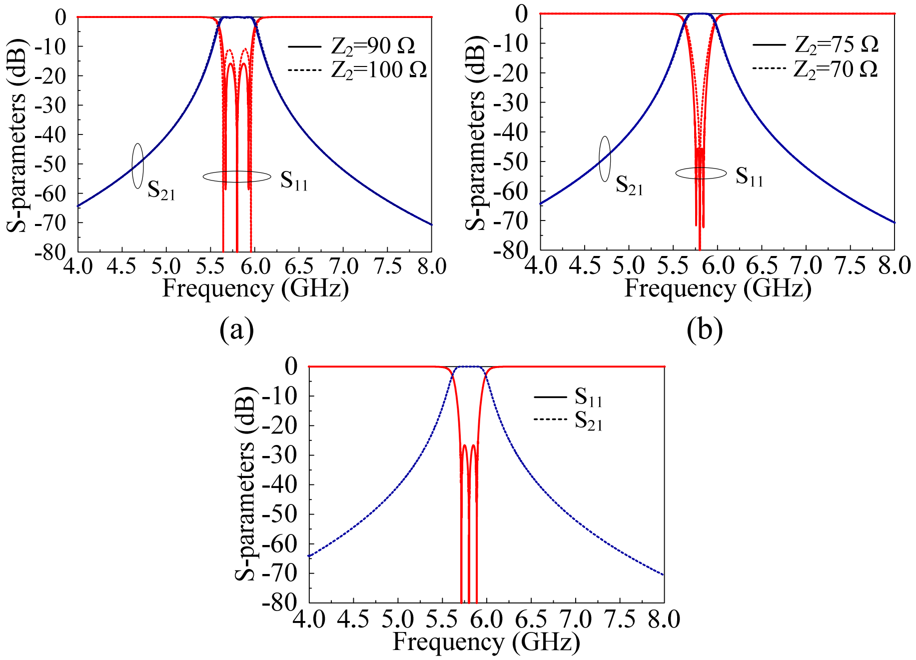

(a) (b)

(c)

Fig. 3-6. Proposed parallel coupled line BPF's simulated results with Z_1=80 Ω and (a) Z_2=90 & 100, (b) Z_2=70 & 75, and (c) Z_2=80 Ω.

$$Z_{oe} = Z\left[1 + JZ + (JZ)^2\right] \tag{3.14}$$

$$Z_{oo} = Z\left[1 - JZ + (JZ)^2\right] \tag{3.15}$$

The design methodology and equations for the proposed parallel coupled line BPF employing non-uniform arbitrary image impedances are validated through simulation and measurement. For the simulation and measurement, a BPF is designed using the parameters of lower cutoff frequency (f_1)=5.7 GHz, upper cutoff frequency (f_2)=5.9 GHz, N=3, and pass-band ripple=0.01 dB.

The simulated results in Fig. 3-6 illustrate S-parameters, where Z_1 is fixed at 80 Ω and Z_2 varies from 70 to 100 Ω. In Fig. 3-6 (a), a magnitude of S_{11} pass-band ripples increases as mismatch degree ($|Z_2\text{-}Z_1|$) becomes higher. In Fig. 3-6 (b), the magnitude of S_{11} ripples in the pass-band decreases along with the bandwidth as Z_2 is smaller than Z_1. In this case, it is also observed that the designed filter produces a single S_{11} pole in the pass-band when Z_2 is further decreased. Fig. 3-6 (c) shows the frequency response characteristic when Z_1=Z_2=80 Ω. This could be the uniform image impedance case of the parallel coupled line BPF [4]. As mentioned earlier, the image impedances (Z_1 and Z_2) can arbitrarily be set by a designer, but input/output port impedances (Z_0) is fixed at 50 Ω. From the study, it has been revealed that magnitude variations of pass-band S_{11} ripples are affected by the mismatch degree, $|Z_2\text{-}Z_1|$. When Z_2 is greater than Z_1, the mismatch degree of 20 Ω has shown a magnitude of 12 dB in a maximum return loss ripple.

Fig. 3-7 presents the simulated and measured results of the designed parallel coupled line BPF using non-uniform image impedances. Two different image impedances which are Z_1=70 Ω and Z_2=80 Ω are applied to the design, where input/output port impedances are fixed at 50 Ω. The simulated and measured insertion losses at the center frequency of 5.8 GHz are found as 0.3 and 1.6 dB, respectively. As shown in Fig. 3-7, the frequency responses of the simulated and measured results show good agreement.

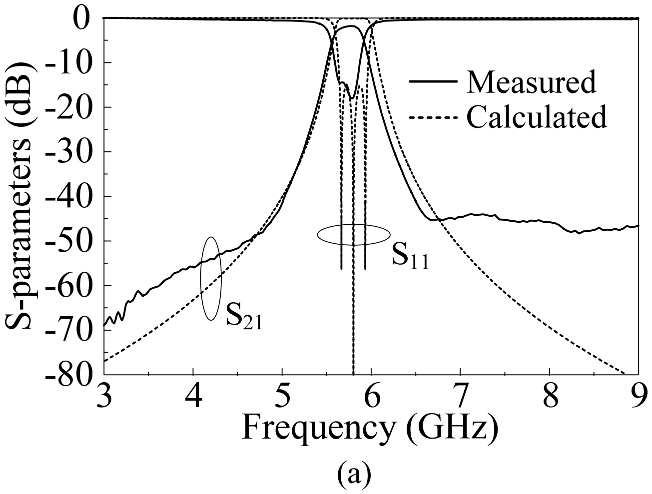

(a)

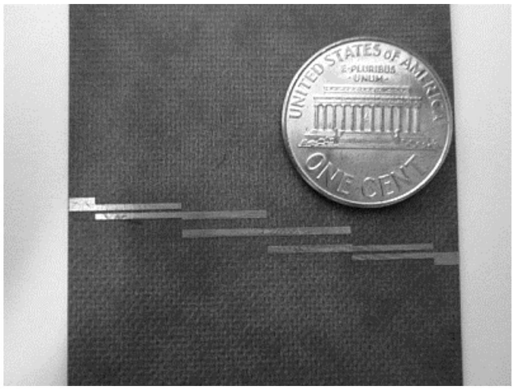

(b)

Fig. 3-7. Demonstration; (a) simulated and measured S-parameters of the proposed parallel coupled BPF using arbitrary image impedances of Z_1=70 Ω and Z_2=80 and (b) photo of the fabricated BPF.

3.3 Capacitive Gap Coupled BPF Using Uniform Arbitrary Image Impedance

A conventional parallel coupled line BPF design is well described in [1] and [4]. Another design method of the parallel coupled line BPF using uniform arbitrary image impedance has also been presented in [6]. A capacitive gap-coupled BPF, which utilizes an end coupled structure, has been reported in [5]. Based on these previous works in [5] and [6], a new design technique using arbitrary image impedance is introduced for a capacitive gap-coupled BPF. Fig. 3-8 (a) illustrates the conventional capacitive gap-coupled BPF consisting of transmission line resonators. In the conventional design, the resonator's characteristic impedance is set to 50 Ω of input/output feed line impedance. However, the proposed capacitive gap-coupled BPF in Fig. 3-8 (b) employs two additional microstrip lines, where Z_1 and θ_A are an arbitrary image impedance and line length, respectively. The arbitrary image impedance can be greater or smaller than port impedance (Z_0). Fig. 3-8 (b) can be modeled as Fig. 3-9 (a) to obtain its admittance inverter equivalent circuit, where $\theta_A = \Phi_A + \Phi_{0,1}/2$ (or $\Phi_{n,n+1}/2$) and $\theta_N = \Phi + \Phi_{N-1,N}/2 + \Phi_{N,N+1}/2$. In Fig. 3-9 (b), the input admittance (Y_A) can be expressed as (3.16) when the line length (Φ_A) is a quarter wavelength.

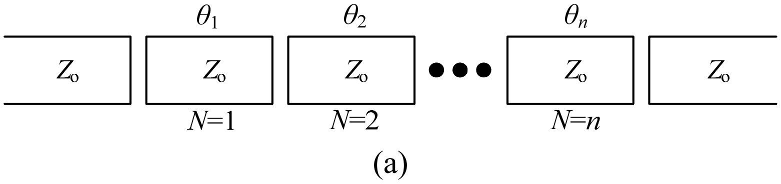

(a)

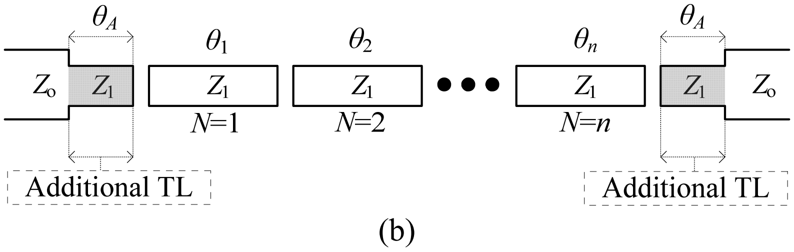

(b)

Fig. 3-8. Capacitive gap-coupled BPF; (a) conventional type and (b) proposed type with arbitrary image impedance (Z_1), where Z_1 can be greater or smaller than Z_0.

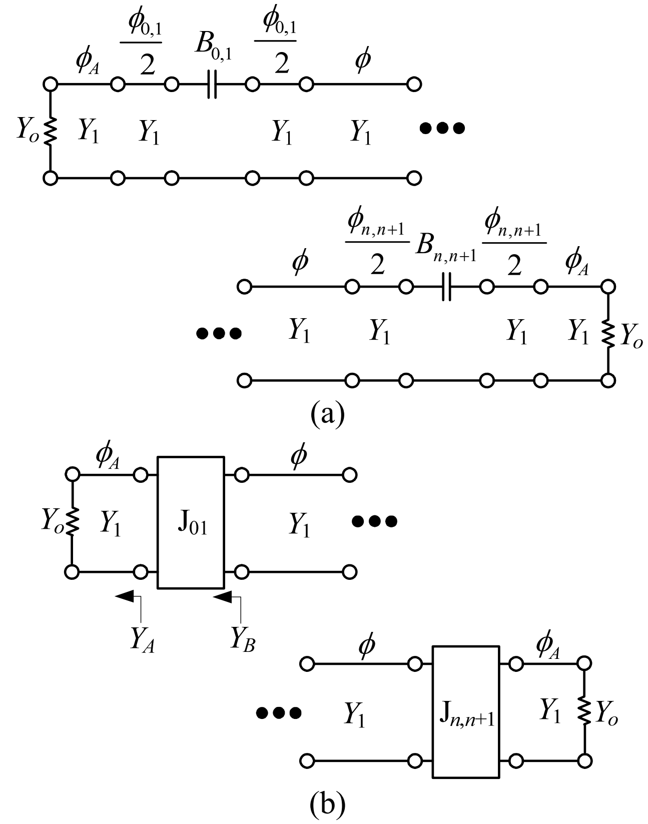

(a)

(b)

Fig. 3-9. Proposed equivalent circuit of Fig. 3-8 (b); (a) transmission line model with negative line lengths ($\Phi_{j,j+1}/2$) and (b) admittance inverter model with an arbitrary image admittance ($Y_1=1/Z_1$).

$$Y_A = Y_1 \frac{Y_o + jY_1 \tan\left(\dfrac{\pi\omega}{2\omega_o}\right)}{Y_1 + jY_o \tan\left(\dfrac{\pi\omega}{2\omega_o}\right)} \tag{3.16}$$

If $\omega \approx \omega_o$, (3.16) can be written as (3.17).

$$Y_A = Y_1 \left. \frac{\dfrac{Y_1}{Y_o} + j\dfrac{\pi}{2}\left(\dfrac{\omega-\omega_o}{\omega_o}\right)}{1 + j\dfrac{\pi}{2}\dfrac{Y_1}{Y_o}\left(\dfrac{\omega-\omega_o}{\omega_o}\right)} \right|_{\omega\approx\omega_o} \tag{3.17}$$

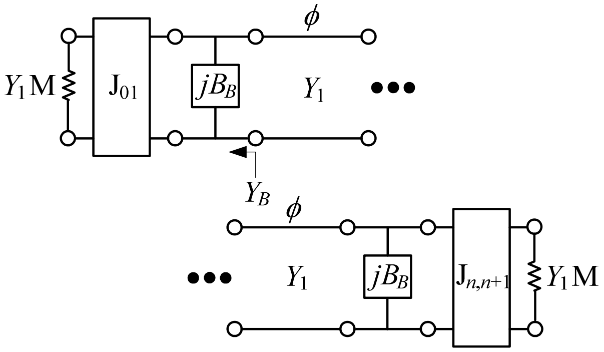

Fig. 3-10. Proposed equivalent circuit model from Fig. 3-9 (b).

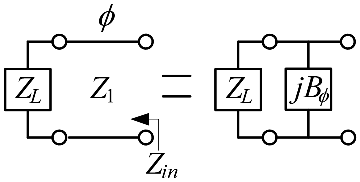

Fig. 3-11. Modeling of the transmission lines with a characteristic impedance of Z_1 and an electrical length of $\Phi=\pi$.

$$M = \frac{Y_1}{Y_o} \tag{3.18}$$

$$N = \frac{\pi}{2}\left(\frac{\omega-\omega_o}{\omega_o}\right) \tag{3.19}$$

Substituting (3.18) and (3.19) in (3.17), input admittance (Y_B) in Fig. 3-9 (b) can be written as (3.20).

$$Y_B = \frac{J_{01}^2}{Y_A} = \frac{J_{01}^2}{Y_1 M + jY_1 N\left(1-M^2\right)} = \frac{J_{01}^2}{Y_1 M} + jB_B \tag{3.20}$$

$$Z_{in} = Z_1\left[\frac{Z_L + jZ_1 \tan\left(\frac{\pi\omega}{\omega_o}\right)}{Z_1 + jZ_L \tan\left(\frac{\pi\omega}{\omega_o}\right)}\right] = \left[\frac{Z_L + jZ_1\pi\left(\frac{\omega-\omega_o}{\omega_o}\right)}{1 + j\frac{Z_L}{Z_1}\pi\left(\frac{\omega-\omega_o}{\omega_o}\right)}\right]_{\omega\approx\omega_o} \tag{3.21}$$

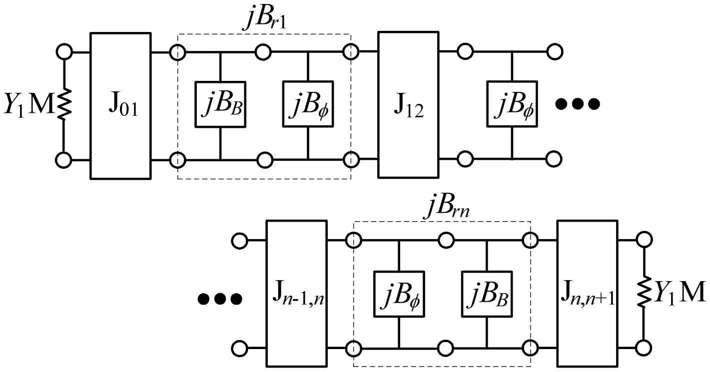

Fig. 3-12. Equivalent circuit model of Fig. 3-10.

From (3.20), the equivalent circuit shown in Fig. 3-9 (b) can be presented as Fig. 3-10. The line sections (Y_1 and Φ) in Fig. 3-10 can be modeled as Fig. 3-11. Input impedance (Z_{in}) in Fig. 3-11 can be expressed as (3.21). Since the resonators in Fig. 3-8 (b) have a relatively large impedance at each end, the condition $Z_L >> Z_1$, can be applied to (3.21) and this leads to (3.22).

$$Z_{in} = \frac{1}{Y_L + jY_1\pi\left(\dfrac{\omega-\omega_o}{\omega_o}\right)} = \frac{1}{Y_L + jB_\phi} \tag{3.22}$$

Thus, Fig. 3-10 can be shown as Fig. 3-12. From (3.20) and (3.22), B_{r1} in Fig. 3-12 can be expressed as (3.23), and the slope parameter of (3.23) is shown in (3.24). Other slope parameters of shunt susceptances in Fig. 3-12 can be calculated in (3.25), where j=2, 3, ⋯, n-1.

$$B_{r1} = B_B + B_\phi = \frac{J_{01}^2 N}{Y_1}\left(1 - \frac{1}{M^2}\right) + 2Y_1 N \tag{3.23}$$

$$b_{r1} = \frac{\omega_o}{2}\frac{dB_{r1}}{d\omega}\bigg|_{\omega=\omega_o} = \frac{\pi Y_1}{4}\left[\frac{J_{01}^2}{Y_1^2}\left(1-\frac{Y_o^2}{Y_1^2}\right)+2\right] \tag{3.24}$$

$$b_{rj} = \frac{\omega_o}{2}\frac{dB_{\phi}}{d\omega}\bigg|_{\omega=\omega_o} = \frac{\pi_1}{2}Y_1 \tag{3.25}$$

Substituting (3.24) and (3.25) into generalized BPF J-inverter equations leads to:

$$J_{01} = J_{n,n+1} = Y_1 \cdot \sqrt{\frac{\pi W}{2\omega_1' g_0 g_1 \left(Y_o/Y_1\right) - W\left(\pi/2\right)\left(1 - Y_o/Y_1\right)}} \tag{3.26}$$

$$J_{12} = J_{n-1,n} = \frac{Y_1 \pi W}{2\omega_1'} \cdot \sqrt{\frac{\left(J_{01}^2/Y_1^2\right)\left(1-Y_o^2/Y_1^2\right)+2}{2g_1g_2}} \tag{3.27}$$

$$J_{j,j+1} = \frac{Y_1 \pi W}{2\omega_1'} \cdot \sqrt{\frac{1}{g_j g_{j+1}}}\Bigg|_{j=2,3\cdots n-2} \tag{3.28}$$

where $\omega_o = \dfrac{2\omega_2\omega_1}{\omega_2+\omega_1}$ and $W = 2\left(\dfrac{\omega_2-\omega_1}{\omega_2+\omega_1}\right)$.

Using the new J-inverter equations in (3.26)-(3.28), the series capacitive susceptances and negative electrical lengths in Fig. 3-9 (a) can be found from (3.29) and (3.30). From (3.30), the electrical lengths of the resonators in Fig. 3-8 (b) can be shown as (3.31) and (3.32). From (3.29), the series coupling capacitance values can be determined by (3.33).

$$B_{j,j+1} = \left. \frac{J_{j,j+1}}{1 - \left(\frac{J_{j,j+1}}{Y_1} \right)^2} \right|_{j=0,\,1,\,\cdots n} \tag{3.29}$$

$$\phi_{j,j+1} = -\tan^{-1}\left. \left(\frac{2B_{j,j+1}}{Y_1} \right) \right|_{j=0,\,1,\,\cdots n} \tag{3.30}$$

$$\theta_A = \frac{\pi - \tan^{-1}\left(\frac{2B_{0,1}}{Y_1} \right)}{2} \tag{3.31}$$

$$\theta_j = \pi - \frac{1}{2}\left[\tan^{-1}\left(\frac{2B_{j-1,j}}{Y_1} \right) + \tan^{-1}\left(\frac{2B_{j,j+1}}{Y_1} \right) \right] \tag{3.32}$$

where j=1, 2, $\cdots$, n.

$$C_{j,j+1} = \left. \frac{B_{j,j+1}}{\omega_o} \right|_{j=0,\,1,\,\cdots n} \tag{3.33}$$

The capacitive-gap coupled BPF is designed using three different arbitrary image impedances (30, 50, and 100 ohm). The filter design parameters are as follow: lower cutoff (f_1): 5.7 GHz, upper cutoff (f_2): 5.9 GHz, N: 5, passband ripple: 0.01 dB, input/output port impedance (Z_o): 50 ohm. When the image impedance is 50 ohm, the conventional and proposed designs produce the same performance as shown in Figs. 3-13 (a) and (b). However, when the image impedance is not the same as the input/output port impedance, the proposed technique achieves better results as shown in Figs. 3-14 and 3-15.

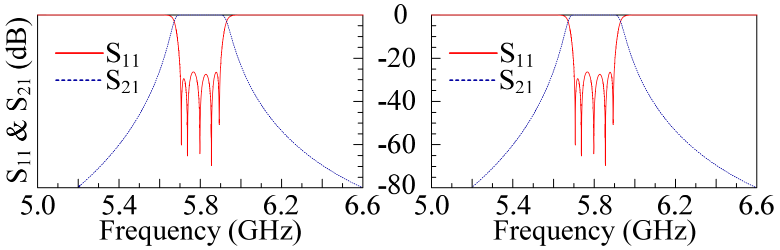

(a) (b)

Fig. 3-13. 50 ohm (a) conventional (b) proposed.

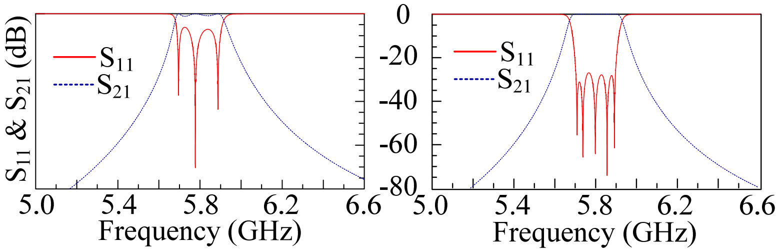

(a) (b)

Fig. 3-14. 30 ohm (a) conventional (b) proposed.

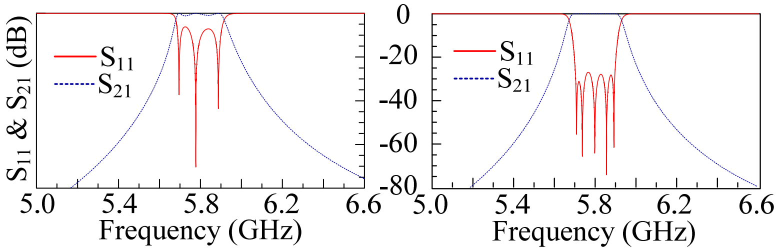

(a) (b)

Fig. 3-15. 100 ohm (a) conventional (b) proposed.

A new design technique using arbitrary image impedance has been introduced for a capacitive gap-coupled BPF. Using the proposed method, a capacitive gap-coupled BPF, which produces the pass-band of 5.7~5.9 GHz and 5-resonant poles within the pass-band, is designed and simulated for different image impedance conditions. In cases where the image impedance is not the same as the input/output impedance, the simulated results based on the proposed design methodology show improved frequency response characteristics compared to the conventional design.

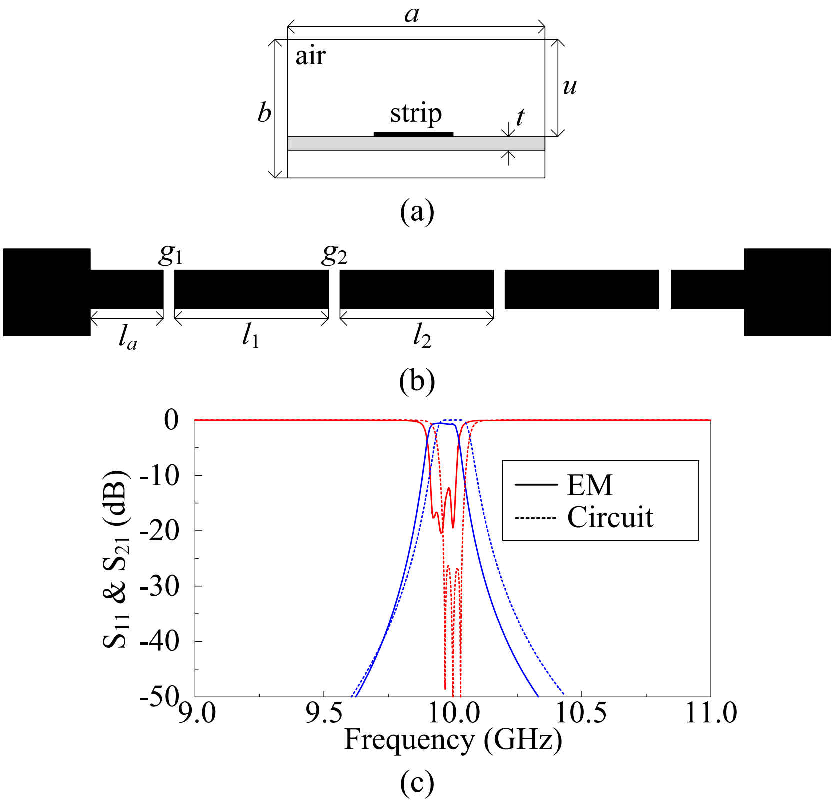

Fig. 3-16. Equivalent circuit model of Fig. 3-10 (N=3).

Based on the proposed capacitive gap-coupled BPF design, the BPF with N=3, f_c=10 GHz, ripple=0.01 dB, and FBW=3.5 % is designed using suspended strip line. The arbitrary image impedance is set to 70 Ω. Fig. 3-16 (a) illustrates the cross section view of the suspended strip line, where a=5, b=1.954, u=1.4, and t=0.254 mm. Fig. 3-16 (b) shows the top view of the suspended strip line, where l_a=6.1, l_1=12.16, l_2=12.2, g_1=0.194, and g_2=1.436 mm. For the given dimensions of the suspended strip structure, 50 Ω line widths of input and output are found to be 1.93 mm. 70 Ω line width is also found to be 1.18 mm. Fig. 3-16 (c) presents the circuit and EM simulated results, and they show good agreement.

3.4 Capacitive Gap Coupled BPF Using Nonuniform Arbitrary Image Impedances

This section introduces a new design technique for a capacitive gap-coupled bandpass filter (BPF) using non-uniform arbitrary image impedances. Based on the proposed BPF equivalent circuit model, the filter's design equations are derived, and they are validated from comparisons of the calculated and simulated results. For this theoretical verification, the BPF using non-uniform arbitrary image impedances is designed using the specifications of: center frequency (f_c)=5.8 GHz, fractional bandwidth (*FBW*)=3.5 %, and filter stage (*N*)=3. The calculated and simulated results of the designed filter show good agreement. The BPF using the proposed design method could provide an advantage that one can arbitrarily determine two different image impedances, which ultimately affects the BPF's coupling gaps and line widths. This could result in suitable filter dimensions, i.e. gaps and line width, for a conventional low resolution photolithography fabrication although a low or high dielectric constant substrate is used for the design.

Planar type filters using microstrip have been popular, and their various design techniques have been presented for last few decades [7]-[18]. In planar type bandpass filters (BPFs), parallel and capacitive gap-coupled line BPFs are frequently used for many system designs because they are relatively easy to design and provide a reasonable performance. Their analysis and design formulas are well described in [4] and [5]. In the designs of these microstrip coupled type BPFs, a dielectric constant should properly be selected in order to obtain suitable filter dimensions which are appropriate for a conventional low resolution photolithography fabrication process. For an example, in a conventional capacitive gap-coupled line BPF design, the lower the dielectric constant is used, the narrower the coupled-gap dimensions is required in order to obtain a desired capacitance value. Therefore, in a low dielectric constant substrate, the coupled line's gap dimension can be too narrow to be fabricated using the conventional low resolution etching process. In order to avoid the inappropriate gap dimensions, an alternative design technique to control the gap dimensions is necessary.

In [6], a parallel coupled line BPF design using a uniform arbitrary image impedance has been introduced. In this paper, a novel design technique for a capacitive gap-coupled BPF using non-uniform arbitrary image impedances is introduced. Proposed design formulas are validated from comparisons of computed and simulated data. Using the proposed design technique, capacitive coupled line's gap dimensions can be controlled by changing the coupled line's image impedances.

A conventional capacitive gap-coupled BPF is presented in Fig. 3-17 (a). As shown in the Fig. 3-17 (a), each resonator's characteristic impedance and input/output port characteristic impedance are set at Z_o. However, the proposed capacitive gap-coupled BPFs in Figs. 3-17 (b) and (c) employ two different image impedances (Z_1 and Z_2) which are not identical to the input/output port characteristic impedances. Here, the two image impedances could arbitrarily be determined. Fig. 3-18 presents the equivalent circuit models of the proposed capacitive gap-coupled BPFs in Figs. 3-17 (b) and (c). It should be noted that another transmission line section at input/output in Figs. 3-17 (b) and (c) is added for maintaining symmetric coupling structures.

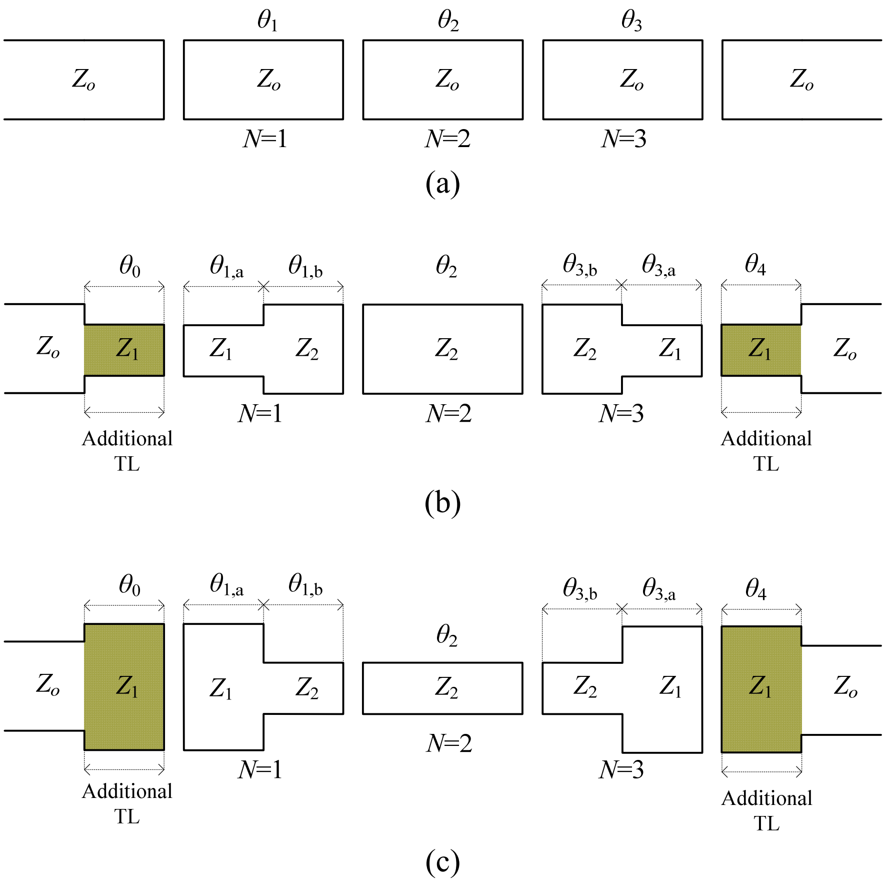

Fig. 3-17. Capacitive gap-coupled BPFs (N=3); (a) conventional BPF, (b) proposed BPF for $Z_1>Z_2$, and (c) proposed BPF for $Z_1<Z_2$.

In order to utilize admittance inverters, the equivalent circuit in Fig. 3-18 (a) could be transformed as Fig. 3-18 (b). Then, the transmission line electrical lengths in Fig. 3-18 (a) and (b) can be expressed as:

$$\theta_0 = \phi + \phi_{01} \tag{3.34}$$

$$\theta_i = \phi_{i-1,i} + 2\phi + \phi_{i,i+1} \tag{3.35}$$

where i=1, 2, 3 and $\phi=\pi/2$ at ω_0.

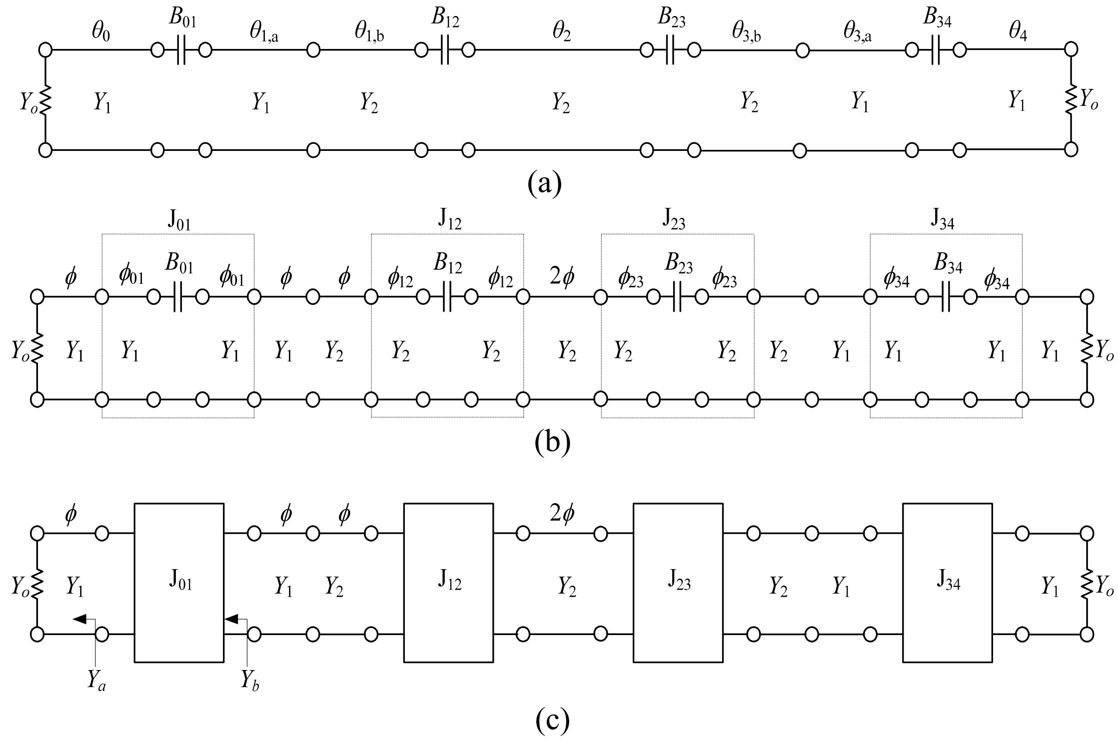

Fig. 3-18. Equivalent circuit models of Fig. 3-17 (b) and (c); (a) transmission line model, (b) J-inverter equivalent circuit model, and (c) J-inverter model.

Electrical lengths, $\theta_{1,a}$ (=$\theta_{3,a}$) and $\theta_{1,b}$ (=$\theta_{3,b}$) are also expressed as $\phi_{01}+\phi$ and $\phi_{12}+\phi$, respectively. Using the admittance inverter equivalent circuit, Fig. 3-18 (b) can be presented as Fig. 3-18 (c). Input admittance, Y_a in Fig. 3-18 (c) can be rewritten as:

$$Y_a = Y_1 \left\{ \frac{Y_1 - jY_0 \dfrac{1}{\tan\left(\dfrac{\pi}{2}\dfrac{\omega}{\omega_o}\right)}}{Y_0 - jY_1 \dfrac{1}{\tan\left(\dfrac{\pi}{2}\dfrac{\omega}{\omega_o}\right)}} \right\} = Y_1 \left\{ \frac{Y_1 + jY_o \tan\left(\dfrac{\pi}{2}\dfrac{\omega}{\omega_o} - \dfrac{\pi}{2}\right)}{Y_o + jY_1 \tan\left(\dfrac{\pi}{2}\dfrac{\omega}{\omega_o} - \dfrac{\pi}{2}\right)} \right\} \qquad (3.36)$$

In (3.36), ω_0 is a center frequency of a designing BPF. When $\omega \approx \omega_0$, the equation in (3.36) is then manipulated as:

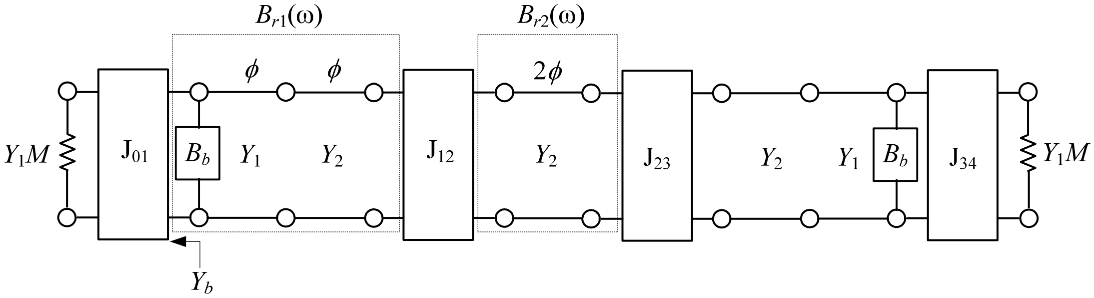

Fig. 3-19. Equivalent circuit model of Fig. 3-2 (c).

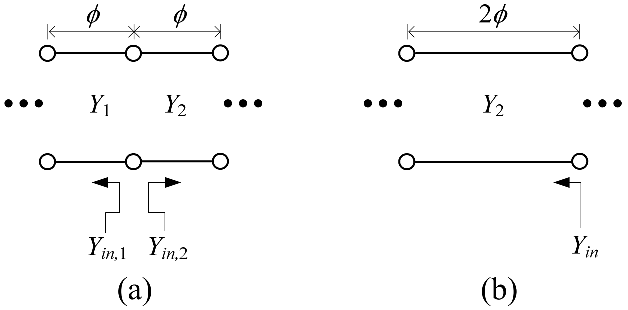

Fig. 3-20. Modeling of the transmission line sections; (a) the first section and (b) the second section.

$$Y_a = Y_1 \left. \left\{ \frac{\frac{Y_1}{Y_o} + j\frac{\pi}{2}\left(\frac{\omega-\omega_o}{\omega_o}\right)}{1 + j\frac{\pi}{2}\frac{Y_1}{Y_o}\left(\frac{\omega-\omega_o}{\omega_o}\right)} \right\} \right|_{\omega\approx\omega_o} \tag{3.37}$$

For simplicity, the expression in (3.37) could be rewritten as:

$$Y_a = \frac{Y_1^2}{Y_o} + jY_1N\left(1-M^2\right) \tag{3.38}$$

where *M* and *N* are:

$$M = \frac{Y_1}{Y_o} \tag{3.39}$$

$$N = \frac{\pi}{2}\left(\frac{\omega-\omega_o}{\omega_o}\right) \tag{3.40}$$

Based on (3.38), input admittance, Y_b in Fig. 3-18 (c) can be expressed as:

$$Y_b = \frac{J_{01}^2}{Y_a} = \frac{J_{01}^2}{Y_1 M + jY_1 N\left(1 - M^2\right)}$$

$$= \frac{J_{01}^2}{Y_1}\left\{\frac{1}{M} + jN\left(1 - \frac{1}{M^2}\right)\right\} \tag{3.41}$$

Since the expression in (3.41) shows a similar form to (3.38), the equivalent circuit model in Fig. 3-18 (c) could be transformed as in Fig. 3-19. As a result, B_b in Fig. 3-19 is written as:

$$B_b = \frac{J_{01}^2 N}{Y_1}\left(1 - \frac{1}{M^2}\right) \tag{3.42}$$

In order to obtain the equivalent susceptances of the transmission line sections in Fig. 3-19, the first and second transmission line sections are modeled in Figs. 3-20 (a) and (b). When $\omega \approx \omega_0$, the input impedances ($Z_{in,1}$ and $Z_{in,2}$) in Fig. 3-20 (a) are expressed as:

$$Z_{in,1} = Z_1 \left. \frac{Z_1 + jZ_L \frac{\pi}{2}\left(\frac{\omega - \omega_o}{\omega_o}\right)}{Z_L + jZ_1 \frac{\pi}{2}\left(\frac{\omega - \omega_o}{\omega_o}\right)} \right|_{\omega \approx \omega_o} \tag{3.43}$$

$$Z_{in,2} = Z_2 \left. \frac{Z_2 + jZ_L \frac{\pi}{2}\left(\frac{\omega - \omega_o}{\omega_o}\right)}{Z_L + jZ_2 \frac{\pi}{2}\left(\frac{\omega - \omega_o}{\omega_o}\right)} \right|_{\omega \approx \omega_o} \tag{3.44}$$

The input impedance of the second transmission line section in Fig. 3-20 (b) is then shown as:

$$Z_{in} = Z_2 \left. \frac{Z_L + jZ_2\pi\left(\dfrac{\omega-\omega_o}{\omega_o}\right)}{Z_2 + jZ_L\pi\left(\dfrac{\omega-\omega_o}{\omega_o}\right)} \right|_{\omega\approx\omega_o} \tag{3.45}$$

Since both ends of the lines in Figs. 3-20 (a) and (b) are physically open circuit, the condition, $Z_L >> Z_1$ and $Z_L >> Z_2$ could be applied to (3.43)-(3.45). As a result, using their admittance expressions, (3.43)-(3.45) can be simplified as:

$$Y_{in,1} = jY_1 \frac{\pi}{2}\left(\frac{\omega-\omega_o}{\omega_o}\right) = jB_1(\omega)\Big|_{\omega\approx\omega_o} \tag{3.46}$$

$$Y_{in,2} = jY_2 \frac{\pi}{2}\left(\frac{\omega-\omega_o}{\omega_o}\right) = jB_2(\omega)\Big|_{\omega\approx\omega_o} \tag{3.47}$$

$$Y_{in} = jY_2 \pi\left(\frac{\omega-\omega_o}{\omega_o}\right) = jB_{r2}(\omega)\Big|_{\omega\approx\omega_o} \tag{3.48}$$

B_1 and B_2 which are the input susceptances of the first line section in Fig. 3-20 (a) can be determined from (3.46) and (3.47). Total susceptance, B_{r1} of the first line section in Fig. 3-19 can be obtained by adding B_b, B_1, and B_2. The equation in (3.48) presents the susceptance of the second line section in Fig. 3-20 (b).

Once the total susceptances (B_{r1} and B_{r2}) of the first and second line sections are found in Fig. 3-19, their slope parameters can simply be determined by solving the first order differential equations in terms of ω:

$$b_{r1} = \frac{\omega_o}{2}\frac{dB_{r1}}{d\omega}\bigg|_{\omega=\omega_0} = \frac{\pi Y_1}{4}\left[\frac{J_{01}^2}{Y_1^2}\left(1-\frac{1}{M^2}\right)+\frac{Y_2}{Y_1}+1\right] \tag{3.49}$$

$$b_{r2} = \frac{\omega_o}{2}\frac{dB_{r2}}{d\omega}\bigg|_{\omega=\omega_0} = \frac{\pi}{2}Y_2 \tag{3.50}$$

Using (3.49) and (3.50), J-inverter expressions for the proposed BPFs in Figs. 3-17 (b) and (c) can be presented as:

$$J_{01} = J_{34} = \sqrt{\frac{WY_1M\pi\left(Y_1+Y_2\right)}{4g_0g_1 - W\pi\left(M-1/M\right)}} \tag{3.51}$$

$$J_{12} = J_{23} = \sqrt{\frac{W^2}{g_1g_2}\left[\frac{\pi^2Y_1Y_2}{8}\left\{\frac{J_{01}^2}{Y_1^2}\left(1-\frac{1}{M^2}\right)+\frac{Y_2}{Y_1}+1\right\}\right]} \tag{3.52}$$

In (3.49)-(3.52), $\omega_o = \frac{2\omega_2\omega_1}{\omega_2+\omega_1}$, $W = 2\left(\frac{\omega_2-\omega_1}{\omega_2+\omega_1}\right)$, and $M = \frac{Y_1}{Y_0}$.

Based on the new J-inverter equations in (3.51) and (3.52), the series capacitive susceptances and negative electrical lengths in Fig. 3-18 (b) can be shown as:

$$B_{j,j+1} = \frac{J_{j,j+1}}{1-\left(\frac{J_{j,j+1}}{Y_1}\right)^2}\Bigg|_{j=0,\ 1,\ \cdots 3} \tag{3.53}$$

$$\phi_{j,j+1} = -\tan^{-1}\left(\frac{2B_{j,j+1}}{Y_1}\right)\Bigg|_{j=0,\ 1,\ \cdots 3} \tag{3.54}$$

Since B_{01}=B_{34} and B_{12}=B_{23} in Fig. 3-18 (a) and (b), electrical lengths of the proposed BPFs in Figs. 3-17 (b) and (c) are: θ_0= $\theta_{1,a}$= $\theta_{3,a}$= θ_4 and $\theta_{1,b}$= $\theta_{3,b}$. Using the equations in (3.34), (3.35), (53), and (54), the electrical lengths of the proposed BPFs in Figs. 3-17 (b) and (c) can be calculated from:

$$\theta_0 = \frac{\pi - \tan^{-1}\left(\dfrac{2B_{0,1}}{Y_1}\right)}{2} \tag{3.55}$$

$$\theta_{1,b} = \frac{\pi - \tan^{-1}\left(\dfrac{2B_{1,2}}{Y_2}\right)}{2} \tag{3.56}$$

$$\theta_2 = \pi - \frac{1}{2}\left[\tan^{-1}\left(\frac{2B_{12}}{Y_1}\right) + \tan^{-1}\left(\frac{2B_{23}}{Y_1}\right)\right] \tag{3.57}$$

Using (3.53), actual series coupling capacitance values in Fig. 3-18 (a) can be determined by:

$$C_{j,j+1} = \left.\frac{B_{j,j+1}}{\omega_o}\right|_{j=0,\ 1,\ \cdots 3} \tag{3.58}$$

In order to validate the proposed design method, a capacitive gap-coupled BPF using non-uniform arbitrary image impedances is designed based on the derived equations. The simulated results are then compared with the calculated results. For the theoretical verifications, the BPF is designed on microstrip, where a substrate thickness and a dielectric constant are 0.508 mm and 2.2, respectively. The BPF's center frequency is 5.8 GHz and the FBW is set to 3.5 %. The number of the filter stages is *N*=3, and Chevyshev prototype element values for passband ripple of 0.01 dB have been used for the proposed J-inverter calculations. Based on the proposed equations, the BPF's electrical lengths and capacitance values are calculated from (3.51)-(3.58). Table 3-1 shows the resulting element values for Fig. 3-18 (a), where *B* is in pF.

Figs. 3-21 (a)-(d) illustrate the frequency responses of the proposed BPF, where the arbitrary image impedance, Z_1 is set to 70 Ω, and Z_2 varies from 80 to 60 Ω. In Figs. 3-21 (a) and (b), a magnitude of passband return loss decreases as mismatch degree ($|Z_1-Z_2|$) becomes higher. In this case ($Z_1<Z_2$), the filter's bandwidth also increases as Z_2 becomes greater than Z_1. In (3.51) and (3.52), increasing Z_2 results in larger J-inverter values. Because J-inverter values are always less than a unity for a BPF design, a susceptance in (3.53) becomes larger. Therefore, a capacitance in (3.58) becomes greater. As a result, increasing Z_2 produces a wide bandwidth due to a larger capacitance. In Figs. 3-21 (c) and (d), the magnitude of return loss in the passband increases as Z_2 becomes smaller than Z_1. However, in this case, a bandwidth of the BPF decreases. When Z_2 is further decreased in Fig. 3-21 (d), it is also observed that the designed BPF produces a single S_{11} pole in the passband. As mentioned earlier, the image impedances (Z_1 and Z_2) can arbitrarily be set by a designer, but input/output feed line characteristic impedances (Z_0) are fixed at 50 Ω.

TABLE 3-1
CALCULATED BPF ELEMENT VALUES FOR FIG. 3-18

	θ_0 , $\theta_{1,a}$	$\theta_{1,b}$	θ_2	$B_{01}= B_{34}$	$B_{12}= B_{23}$
Z_1=70, Z_2=80	76.6859	85.9543	171.9086	0.0983	0.02439
Z_1=70, Z_2=75	76.4879	86.0221	172.0441	0.1001	0.02557
Z_1=70, Z_2=65	76.0141	86.1613	172.3225	0.1041	0.02846
Z_1=70, Z_2=60	75.7272	86.2328	172.4656	0.1066	0.03025
Z_1=70, Z_2=70	76.2656	86.0910	172.1821	0.1019	0.02692
Z_1=50, Z_2=50	73.6469	86.0339	172.0679	0.1762	0.03824

Figs. 3-22 (a) and (b) show the frequency responses when Z_1=Z_2. In Fig. 3-22 (a), the arbitrary image impedances, Z_1 and Z_2 are set to 70 Ω. This could be the uniform arbitrary image impedance design for a capacitive gap-coupled BPF. As shown in Fig. 3-22 (a), the design provides a return loss greater than 20 dB, and satisfies the desired design specifications, i.e., *FBW*, center frequency, and etc. In Fig. 3-22 (b), the arbitrary image impedances, Z_1 and Z_2 are set to 50 Ω, which is identical to a conventional capacitive gap-coupled BPF. Both calculated and simulated results in Figs. 3-22 (a) and (b) show good agreement.

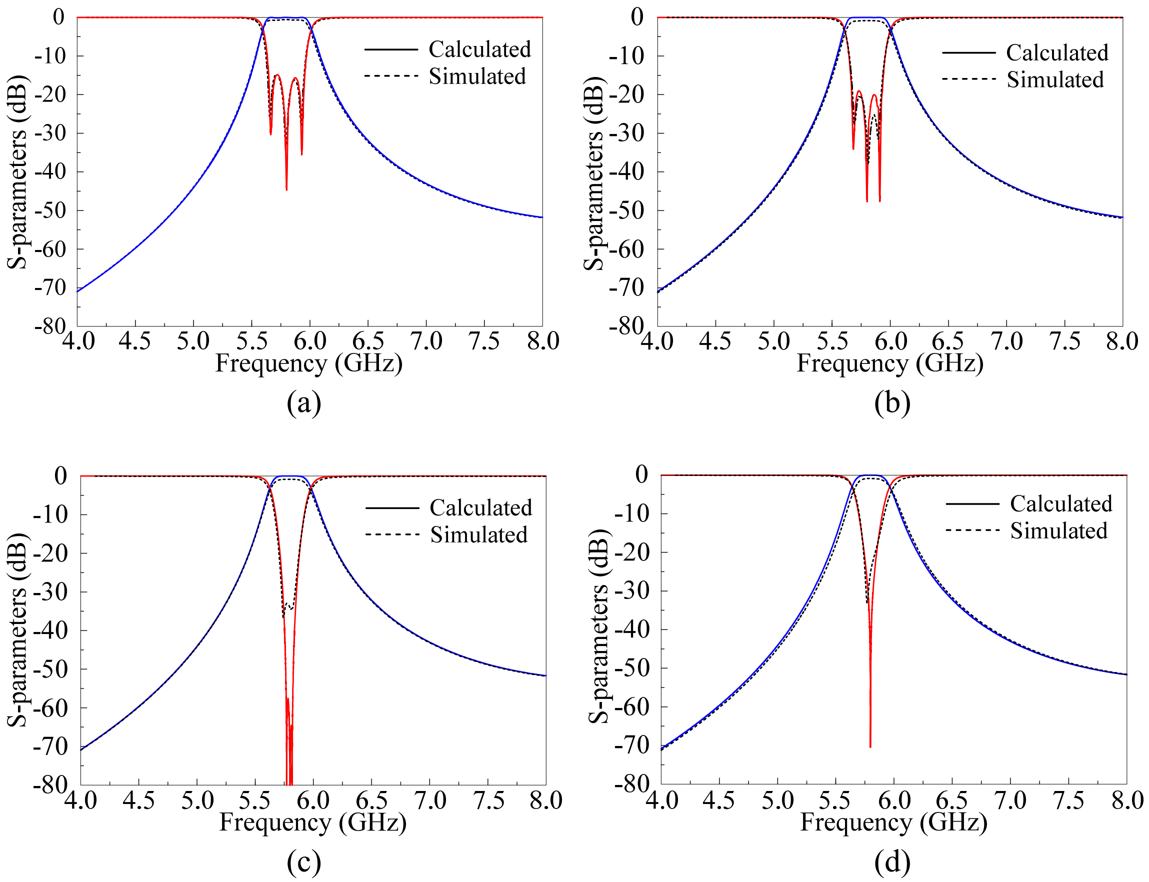

(a) (b)

(c) (d)

Fig. 3-21. Calculated and simulated results of proposed capacitive gap-coupled BPF, where Z_1=70 Ω and Z_2= (a) 80, (b) 75, (c) 65, (d) 60 Ω.

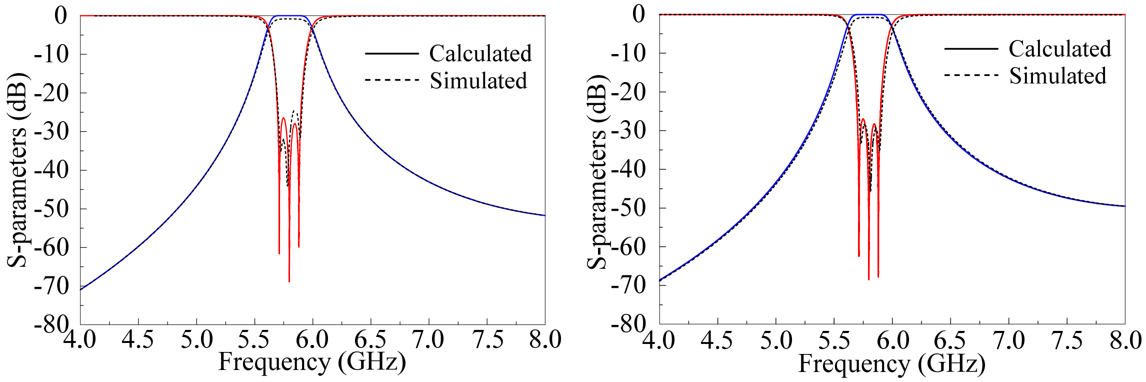

(a) (b)

Fig. 3-22. Calculated and simulated results of proposed capacitive gap-coupled BPF; (a) Z_1=70 and Z_2=70 Ω and (b) Z_1=50 and Z_2=50 Ω.

A capacitive gap-coupled BPF using non-uniform arbitrary image impedances has been introduced and studied based on circuit and classical filter theories. The proposed design topologies and equations are validated from comparing the equation based calculation results and simulated results. In the proposed design, two different impedances can arbitrarily be set to the image impedances of a capacitive gap-coupled line BPF. Therefore, a designer can favorably control the BPF's resonator characteristic impedances. This would allow of reasonable line widths and gap dimensions on a low or high dielectric constant substrate. Using the derived design equations, a capacitive gap-coupled BPF has been designed and simulated. Both calculated and simulated results have shown good agreement. The proposed design technique is simple and easy, and the design could be realized using a microstrip line or a suspended strip line.

3.5 Hairpin BPF Design Using Nonuniform Arbitrary Image Impedances

In this chapter, a new design technique for a hairpin bandpass filter (BPF) using nonuniform arbitrary image impedances is introduced. The hairpin BPF using the proposed design method could provide an advantage that resonator's coupling gaps and line widths can be adjustable by changing the resonator's arbitrary image impedances. Based on the equivalent circuit of the proposed hairpin BPF, admittance inverters are derived, and they are validated from simulations and measurements. In the proposed design, resonator's electrical lengths are also adjusted to maintain the filter's return loss greater than 20 dB. Hairpin bandpass filters (BPFs) have drawn much attention in modern RF/microwave filter designs because of their simple planar type structures, reliable performance, compactness [19-20], and tuning ability [21]. The design of hairpin BPF can be achieved using resonator's cross coupling coefficients and external quality factors (Q_{ext}) at input/output ports [22]. However, in the coupling coefficient based design, rigorous electromagnetic (EM) simulations are necessary to determine a coupling coefficient for given gap dimensions.

In this chapter, a proposed hairpin BPF is analyzed based on a transmission line (TL) equivalent circuit model. From the TL model, resonator's slope parameters and coupled line's admittance inverters are derived. As a result, EM simulation for coupling coefficients and Q_{ext} is not required in the design. The proposed design method employs two different arbitrary image impedances, which ultimately becomes the characteristic impedances of the hairpin resonators. Changing resonator's characteristic impedance results in a variation of coupling gap; high (low) characteristic impedance produces a wide (narrow) coupling gap. Thus, although a low dielectric substrate is utilized, the proposed design could provide a reasonable gap dimension for an easy fabrication.

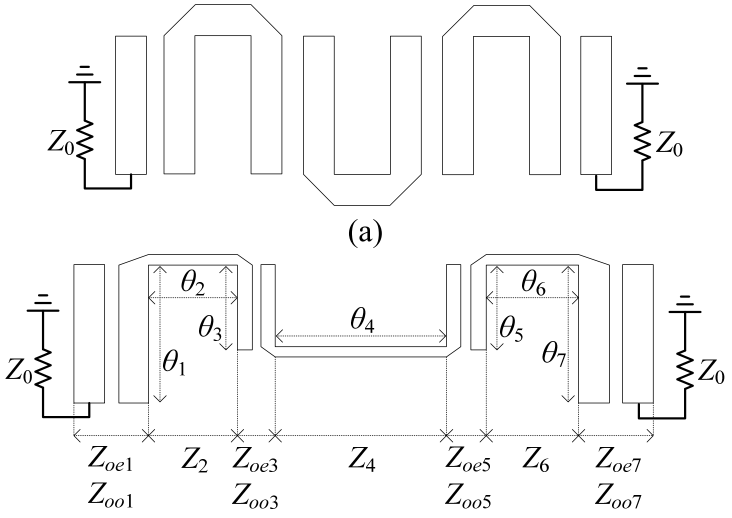

(a)

(b)

Fig. 3-23. Hairpin BPFs; (a) conventional and (b) proposed type (θ_2+ θ_3=90º and θ_3+ θ_4/2=90º).

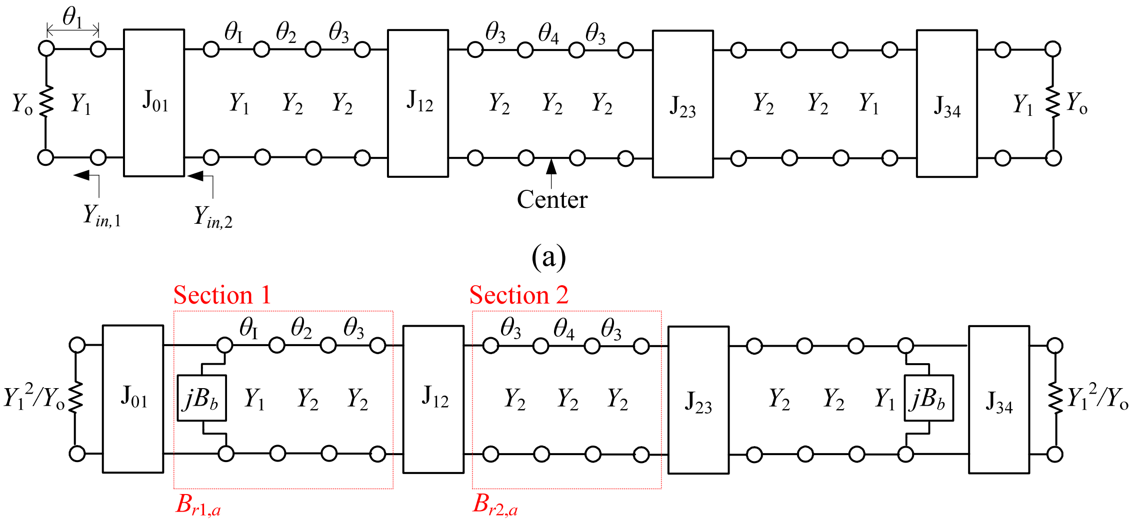

(a)

(b)

Fig. 3-24. Equivalent circuit models of proposed hairpin BPF; (a) initial and (b) simplified models, where Y_1 and Y_2 are adjustable admittance.

Fig. 3-23 (a) shows a conventional hairpin BPF fed by a parallel coupled line, where resonators utilize uniform characteristic impedance optimized from EM simulation. Fig. 3-23 (b) illustrates the proposed hairpin BPF, where resonator's characteristic impedance could arbitrarily be set and lengths (θ_2, θ_3, θ_4) are also adjustable. The first coupled line length (θ_1) is fixed to $\lambda_{g0}/4$, but $\theta_2+\theta_3=\lambda_{g0}/4$ and $\theta_3+\theta_4/2=\lambda_{g0}/4$. Fig. 3-23 (a) presents an equivalent circuit of the proposed hairpin BPF in Fig. 3-23 (b), where arbitrary image admittances ($Y_1=1/Z_1$, $Y_2=1/Z_2$) are employed as characteristic admittances of the resonators. If $\theta_1=\pi/2$ and $\omega\approx\omega_0$ in Fig. 3-24 (a), the input admittance, Y_{in1} could be expressed as:

$$Y_{in,1}=Y_1\left.\frac{\dfrac{Y_1}{Y_o}+j\dfrac{\pi}{2}\left(\dfrac{\omega-\omega_o}{\omega_o}\right)}{1+j\dfrac{\pi}{2}\dfrac{Y_1}{Y_o}\left(\dfrac{\omega-\omega_o}{\omega_o}\right)}\right|_{\omega\approx\omega_o} \tag{3.59}$$

Then, the expression in (3.59) could be simplified as:

$$Y_{in,1}=\frac{Y_1^2}{Y_o}+jY_1N(1-M^2) \tag{3.60}$$

where M and N are:

$$M=\frac{Y_1}{Y_o} \tag{3.61}$$

$$N=\frac{\pi}{2}\left(\frac{\omega-\omega_o}{\omega_o}\right) \tag{3.62}$$

Input admittance, $Y_{in,2}$ in Fig. 3-2 (a) is then written:

$$Y_{in,2} = \frac{J_{01}^2}{Y_{in,1}} = \frac{J_{01}^2}{Y_1 M}[1 + jN(M - {}^{1}\!/_{M})] \tag{3.63}$$

Since (3.60) and (3.63) are in similar form, equivalent circuit in Fig. 3-24 (a) can be transformed to Fig. 3-24 (b). Near a resonant frequency ($\omega \approx \omega_0$), the susceptance, B_b in Fig. 3-24 (b), which is the imaginary part of (3.63), becomes zero (B_b=0). Because the filter is designed at the center frequency (ω_0), B_b can be assumed as zero.

The first resonator, Section 1 in Fig. 3-24 (b) could be modeled as shown in Fig. 3-25. The modeling is necessary for deriving resonator's slope parameter expression. When considering the susceptance, $\mathrm{B}_{\mathrm{r1,a}}$ in Fig. 3-24 (b), it can be expressed as:

$$B_{r1,a} = B_{1,a} + B_{2,a} \tag{3.64}$$

where $B_{1,a}$=$jY_1\tan(\theta_1)$ and $B_{2,a}$=$jY_2\tan(\theta_A)$.

Then, (3.64) leads to:

$$B_{r1,a} = Y_1 \tan\left\{\theta_1 + \tan^{-1}\left(\frac{Y_2}{Y_1}\tan(\theta_A)\right)\right\} \tag{3.65}$$

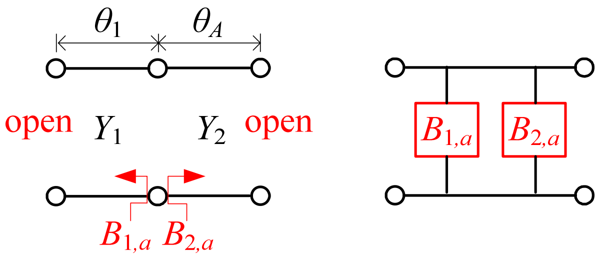

(a) (b)

Fig. 3-25. Section 1 modeling; (a) TL model (θ_A=θ_2+θ_3) and (b) its equivalent model.

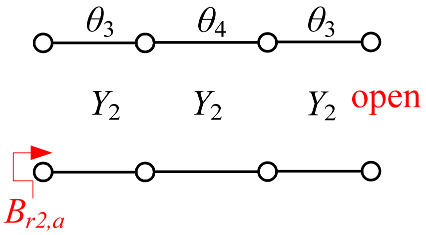

Fig. 3-26. Section 2 modeling.

At resonance ($\omega \approx \omega_0$), (3.65) should be zero. The angle of tangent in (3.64) could be rewritten using propagation constant, β and physical line length, l, and the angle needs to be equal to $n\pi$:

$$\left|\theta_1 + \tan^{-1}\left(\frac{Y_2}{Y_1}\tan(\theta_A)\right)\right| = \beta l = n\pi \tag{3.66}$$

For a simple case (n=1), (3.66) determines $l=\lambda_0/2$, then the angle of tangent:

$$\beta l = \frac{2\pi}{\lambda}\frac{\lambda_0}{2} = \frac{2\pi f}{c}\frac{c}{2f_0} = \pi\frac{\omega}{\omega_0} \tag{3.67}$$

From (3.67), (3.65) can be shown as:

$$B_{r1,a} = Y_1 \tan\left(\pi\frac{\omega}{\omega_0}\right) = Y_1 \tan\left\{\pi\left(\frac{\omega-\omega_0}{\omega_0}\right)\right\} \tag{3.68}$$

When $\omega \approx \omega_0$, (3.68) is simplified:

$$B_{r1,a} = Y_1 \pi\left(\frac{\omega-\omega_0}{\omega_0}\right) \tag{3.69}$$

The slope parameter of (3.69) is then:

$$b_{r1,a} = \frac{\omega_0}{2}\frac{d}{d\omega}\left(B_{r1,a}\right)\Big|_{\omega=\omega_0} = \frac{\pi}{2}Y_1 \tag{3.70}$$

In similar way, the second resonator ($B_{r2,a}$) can be modeled in Fig. 3-26. The susceptance, $B_{r2,a}$ is expressed as:

$$B_{r2,a} = Y_2 \tan\left(2\theta_3 + \theta_4\right) \tag{3.71}$$

The slope parameter of (3.71) is then derived as:

$$b_{r2,a} = \frac{\omega_0}{2}\frac{d}{d\omega}\left(B_{r2,a}\right)\Big|_{\omega=\omega_0} = \frac{\pi}{2}Y_2 \tag{3.72}$$

Finally, admittance inverters for the proposed hairpin BPF can be obtained:

$$J_{01} = J_{34} = \sqrt{\frac{\pi Y_1^3 FBW}{2\omega_1' g_0 g_1 Y_0}} \tag{3.73}$$

$$J_{12} = J_{23} = \frac{\pi FBW}{2\omega_1'}\sqrt{\frac{Y_2^2}{g_1 g_2}} \tag{3.74}$$

where $FBW = \left(\frac{\omega_2 - \omega_1}{\omega_0}\right)$ and $\omega_0 = \frac{\omega_2 + \omega_1}{2}$.

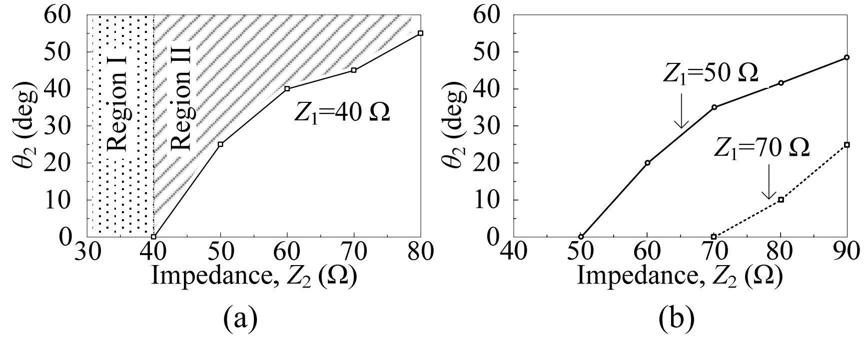

(a) (b)

Fig. 3-27. θ_2 vs. Z_1 & Z_2 for return loss of greater than 20 dB; (a) for Z_1=40 Ω and (b) for Z_1=50, 60, and 70 Ω.

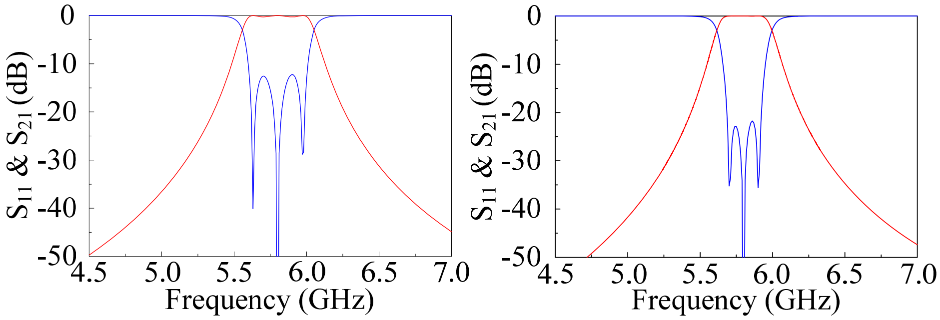

(a) (b)

Fig. 3-28. Designed BPF's frequency responses for (a) θ_2=10° and (b) θ_2=40°, where Z_0=50, Z_1=40, and Z_2=60 Ω.

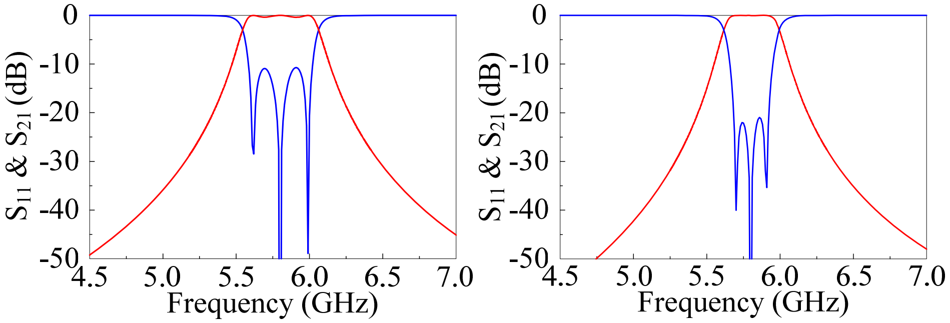

(a) (b)

Fig. 3-29. Designed BPF's frequency responses for (a) θ_2=10° and (b) θ_2=42°, where Z_0=50, Z_1=50, and Z_2=80 Ω.

In order to validate the proposed design method, a hairpin BPF is tested using design specifications:f_2=5.92, f_1=5.68, f_c=5.8 GHz, FBW=0.0414 %, Chevyshev ripple=0.01 dB. Resonator's variable impedances are set to two different cases: Case I (Z_1=40 Ω, Z_2= 60 Ω) and Case II (Z_1=50 Ω, Z_2= 80 Ω). Electrical length, θ_2 is initially set to 10° for the both cases. In Fig. 3-27 (a), Region I indicates $Z_1 > Z_2$. When Z_2 is relatively smaller than Z_1, the designed BPF has shown a single S_{11} pole, and bandwidth shrank due to decreased J-values (J_{12} & J_{23}). If J decreases, even and odd mode characteristic impedances of a coupled line also decrease. This results in coupling reduction. However, Z_2 becomes greater than Z_1, coupling of the parallel coupled line increases with bandwidth. Here, optimum θ_2 which produces return loss greater than 20 dB is experimentally found for different Z_1 and Z_2. Figs. 3-27 (a) and (b) show the optimum θ_2 for return loss greater than 20 dB. In this letter, Region II is only considered for three S_{11} poles. From Fig. 3-27 (a) and (b), θ_2 for the Cases I and II are 40 ° and 42 °, respectively.

TABLE 3-2
DESIGN PARAMETERS FOR CASE I AND II

Case I		Case II	
J_{01}=0.009	J_{12}=0.0014	J_{01}=0.0064	J_{12}=0.001
Z_{oe}=59.54Ω Z_{oo}=30.79Ω	Z_{oe}=65.41Ω Z_{oo}=55.42Ω	Z_{oe}=71.24Ω Z_{oo}=39.09Ω	Z_{oe}=87.21Ω Z_{oo}=73.90Ω
θ_2= 40°		θ_2= 42°	

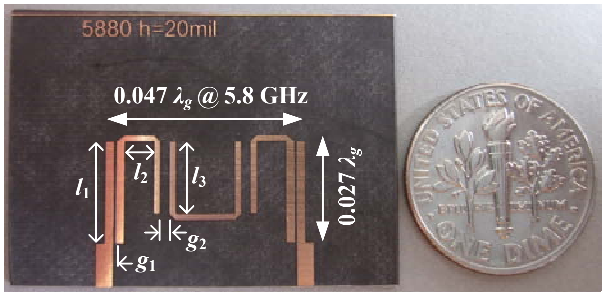

Fig. 3-30. Photo of the fabricated BPF; Z_1=70, Z_2=90, θ_2=25°, ε_r=2.2 (l_1=9.24, l_2=2.7, l_3=6.6, g_1=0.2, and g_2=0.86 mm).

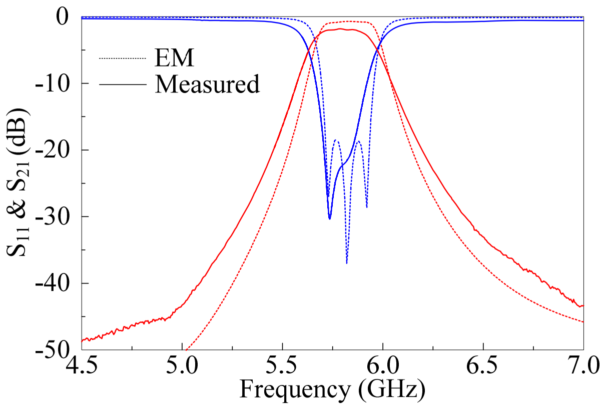

Fig. 3-31. EM simulated and measured hairpin BPF in Fig. 3-30.

Table 3-2 presents the calculated BPF parameters. Figs. 3-28 and 29 show simulated results of the Cases I and II. By utilizing the proposed hairpin BPF design technique, one can have flexibility on selection of substrate's dielectric constant. For high (low) dielectric substrate, low (high) impedance is preferable. Fig. 3-30 presents a photo of the fabricated hairpin BPF, where the variable impedances are set to Z_1=70 and Z_2=90 Ω, and θ_2 is found as 25° from Fig. 3-27 (b). Fig. 3-31 illustrates EM simulated and measured results of the fabricated BPF. Employing high impedance on low dielectric substrate increases even and odd mode impedances of a parallel coupled line, which ultimately increases a gap distance. Thus, a filter fabrication using conventional low resolution photolithography can be easier.

3.6 Conclusions

In this Chapter III, BPF designs using uniform or non-uniform arbitrary image impedances have been introduced. For demonstrations, a parallel coupled line BPF, capacitive gap-coupled line BPF, and hairpin BPF are utilized. The proposed BPF designs are validated from simulations and measurements. The design procedure is simple, and the design parameters can directly be calculated from given BPF design specifications. In the proposed BPF designs, the coupled line's gap distance can be adjusted by varying the arbitrary image impedance.

CHAPTER IV

DUAL-BAND AND TRIPLE BAND BANDPASS FILTER SYNTHESES

4.1 Introduction

As today's frequency spectrum becomes increasingly crowded, dual-band and multi-band systems are emerged for an efficient system operation and frequency use. For these dual- or multi-band systems, dualband bandpass filter (DBBPF) and tripleband bandpass filters (TBBPF) have been developed. A DBBPF has been reported in [23]-[29] for multiband applications. In [23], a DBBPF was achieved by connecting two different BPFs in parallel. In [24], a wideband BPF was cascaded with a narrow-band bandstop filter in order to produce the dual passband. In [25], an anti-resonator, i.e., series *LC* resonator in shunt, has been employed for a DBBPF design. By connecting three anti-resonators, three different transmission zeros have been achieved, which ultimately produces dual passband. [26] and [27] have utilized stepped impedance resonators (SIRs) to realize a DBBPF, where the coupled structure SIRs are mirrored for a transmission zero between the two passbands. [28] and [29] proposed DBBPF designs based on a classical admittance inverter theory. One of the remarkable advantages of the DBBPF designs in [28] and [29] is that the center frequencies and passband widths of the dual bands can independently be controlled.

TBBPFs have also been developed in [30]-[32]. However, the designs shown in [30]-[32] utilizes complicated microstrip structures and is difficult to control the frequency responses including center frequencies and bandwidths. For these reasons, a new design method for the TBBPF is developed and introduced in this chapter.

4.2 Dual-Band BPF Synthesis

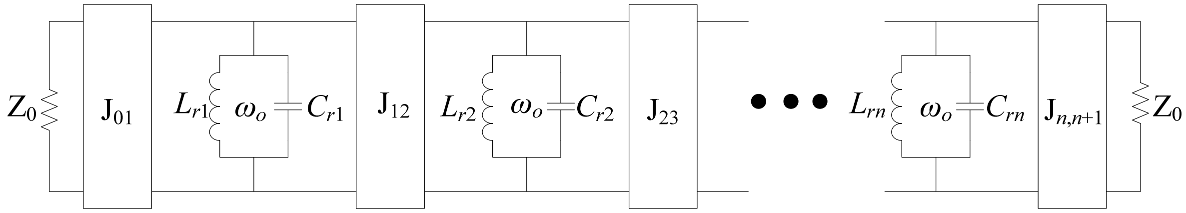

Fig. 4-1. Conventional BPF with J-inverters and shunt parallel LC resonators.

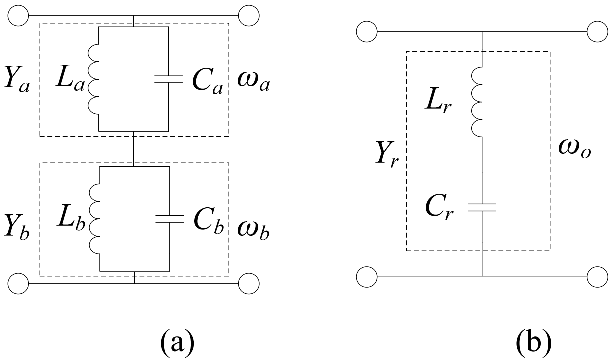

Fig. 4-2. Lumped (a) composite series resonator and (b) its equivalent LC series resonator [29].

In this section, a DBBPF design shown in [29] is briefly introduced for background review. Fig. 4-1 shows the conventional BPF using parallel *LC* resonators and admittance inverters (J-inverter). The J-inverters can be determined using the well kwon formulas in (4.1)-(4.4), where Ω_c=1 (rad/sec), ω_0= mid-band angular frequency of the BPF, FBW=fractional bandwidth, and g_i(i=0 to n+1)=prototype LPF element values [1].

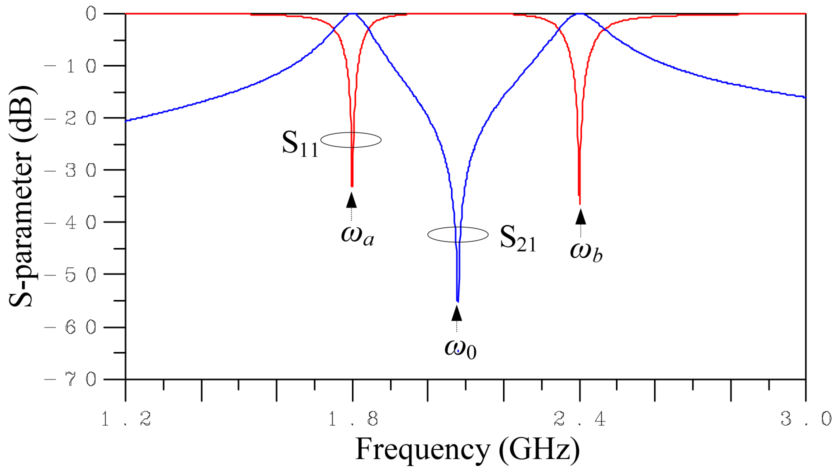

Fig. 4-3. Frequency response of the composite resonator in Fig. 4-2 (a), where L_a=0.111 nH, L_b=0.083 nH, C_a=70.249 pF, and C_b=52.687 pF.

$$L_{ri} = \left.\frac{1}{\omega_0^2 C_{ri}}\right|_{i=1\ \text{to}\ n} \tag{4.1}$$

$$J_{0,1} = \sqrt{\frac{FBWG_0\omega_0 C_{ri}}{\Omega_c g_0 g_1}} \tag{4.2}$$

$$J_{i,i+1} = \left.\frac{FBW\omega_0}{\Omega_c}\sqrt{\frac{C_{ri}C_{ri+1}}{g_i g_{i+1}}}\right|_{i=1\ \text{to}\ n-1} \tag{4.3}$$

$$J_{n,n+1} = \sqrt{\frac{FBWG_{n+1}\omega_0 C_{rn}}{\Omega_c g_n g_{n+1}}} \tag{4.4}$$

Fig. 4-2 (a) shows a composite series resonator consisting of two cascaded parallel *LC* resonators. The two composite resonators have the susceptances of Y_a and Y_b, and resonate at ω_a and ω_b, respectively.

$$Y_{a\ \text{or}\ b} = j\omega C_{a\ \text{or}\ b} + \frac{1}{j\omega L_{a\ \text{or}\ b}} \tag{4.5}$$

$$\omega_{a\ \text{or}\ b} = \frac{1}{\sqrt{L_{a\ \text{or}\ b}C_{a\ \text{or}\ b}}} \tag{4.6}$$

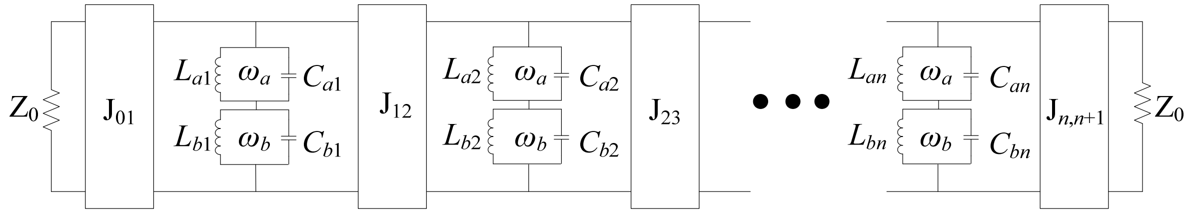

Fig. 4-4. DBBPF equivalent circuit model using composite resonators and J-inverters [29].

$$Y_{a\,\mathrm{or}\,b} = j\omega C_{a\,\mathrm{or}\,b}\left\{1-\left(\frac{\omega_{a\,\mathrm{or}\,b}}{\omega}\right)^2\right\} \tag{4.7}$$

$$\omega_0 \cong \frac{1}{\sqrt{(L_a+L_b)\cdot\left(\dfrac{C_aC_b}{C_a+C_b}\right)}} = \sqrt{\omega_a\omega_b} \tag{4.8}$$

The susceptances of Y_a and Y_b can be written as (4.5). Using the resonant condition in (4.6), (4.5) can be presented as (4.7). In (4.7), the assumption, $\omega_a < \omega_b$ leads $Y_a > 0$ (capacitive) and $Y_b < 0$ (inductive) for the frequency region of $\omega_a < \omega < \omega_b$. As a result, the composite resonator in Fig. 4-2 (a) can be represented as a series *LC* resonator in Fig. 4-2 (b). The resonator in Fig. 4-2 (b) produces a bandstop frequency response at ω_0, where ω_0 can approximately be calculated using (4.8).

In order to demonstrate the composite resonator in Fig. 4-2 (a), a circuit simulation is utilized, where the element values are: L_a=0.111 nH, L_b=0.083 nH, C_a=70.249 pF, and C_b=52.687 pF. These lumped element values have been determined using (4.6) and (4.9), where f_a, FWB_a, f_b, FWB_b, and J_{01} for Butterworth (N=2) are set to 1.8 GHz, 4 %, 2.4 GHz, 4 %, and 0.0212, respectively. The equations in (4.9)-(4.11) are derived from (4.2)-(4.4). As shown in Fig. 4-3, the composite series resonator produces two resonant frequencies (ω_a and ω_b), which ultimately becomes the center frequency of the DBBPF. Fig. 4-4 presents the equivalent circuit model of the DBBPF. It is important to notice that the J-inverter values in the DBBPF design are assumed to be constant over the frequency. Fig. 4-5 illustrates a design flow of the DBBPF.

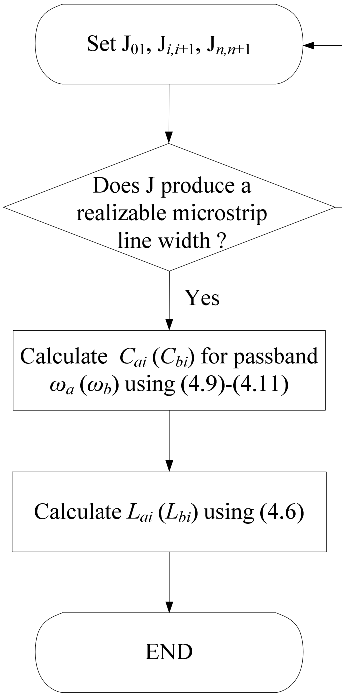

Fig. 4-5. Design flowchart for DBBPF.

$$C_{r,1} = \frac{\Omega_c g_0 g_1 J_{0,1}^2}{FBW_r G_0 \omega_r} \tag{4.9}$$

$$C_{r,n} = \frac{\Omega_c g_n g_{n+1} J_{n,n+1}^2}{FBW_r G_{n+1} \omega_r} \tag{4.10}$$

$$C_{r,i+1} = \frac{\Omega_c^2 g_i g_{i+1} J_{i,i+1}^2}{FBW_r^2 \omega_r^2 C_{ri}} \tag{4.11}$$

where r=a or b.

Even though this design flow in [29] provide a reasonable design procedure, guessing an initial J-value in Fig. 4-5 is difficult. It should be noticed that if inductance and capacitance values in Fig. 4-2 (a) are not properly chosen, the composite resonator does not provide the dualband frequency response. This means that DBBPF design using the composite resonators in Fig. 4-2 (a) could not be successful although the J-value satisfies the realizable microstrip line width. For these reasons, instead of guessing the J-value, composite resonator's element value calculations could utilize:

$$C_{r,i} = \frac{g_i}{FBW_r \, \omega_r Z_0} \tag{4.12}$$

where r=a or b and i=1 to n. Once the capacitance value is determined from (4.12), J-value and inductance value can be calculated from (4.2-4) and (4.6), respectively. The equation in (4.12) is derived from bandpass frequency transformation and impedance scaling of prototype LPF element value.

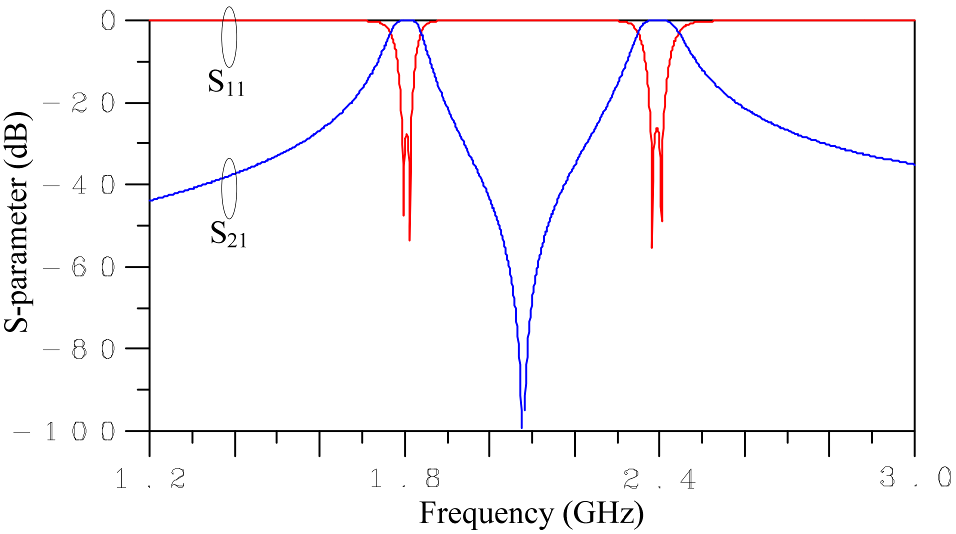

Fig. 4-6. 1.8 GHz and 2.4 GHz DBBPF simulation result in Fig. 4-4, where J-inverter is realized using a quarter wavelength transmission line at ω_0=2.078 GHz.

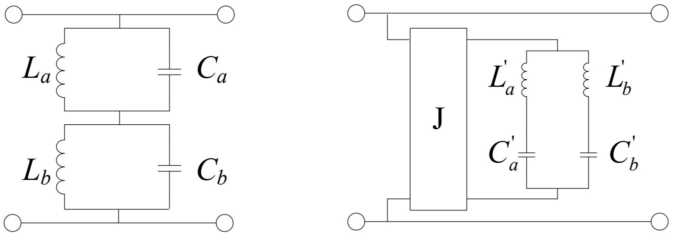

(a) (b)

Fig. 4-7. Transformation from (a) the composite series resonator to composite shunt resonator [29].

Fig. 4-6 presents the circuit simulated S-parameters of the DBBPF in Fig. 4-4. Instead of utilizing (4.12), the DBBPF is designed using the method shown in [29]. The designed DBBPF produces the pass-band at 1.8 GHz and 2.4 GHz with FBW of 4 %. The number of filter stages is N=2, and J_{01} (=J_{23}) and J_{12} are set at 0.0212 and 0.0228, respectively. Since J-inverter values are defined, the lumped element values in Fig. 4-4 can be calculated using (4.9) and (4.10). The inductance in Fig. 4-4 can also be determined by (4.6). J-inverters in Fig. 4-4 are realized by microstrip quarter wavelength transmission line at ω_0. The line width, i.e., characteristic impedance, can be determined because J-inverter values have already been known. The resulting lumped element values in Fig. 4-4 are: C_{a1} (C_{a2})=70.249 pF, L_{a1} (L_{a2})=0.111 nH, C_{b1} (C_{b2})=52.687 pF, and L_{b1} (L_{b2})=0.083 nH. However, it is not easy to realize the lumped composite resonators using microstrip. Thus, a transformation using additional J-inverter is necessary. The lumped composite resonator in Fig. 4-7 (a) can be transformed as shown in Fig 38 (b), where the resulting element values (L_a', C_a', L_b', and C_b') can be determined from (4.13)-(4.16).

$$C_a' = L_a J^2 \tag{4.13}$$

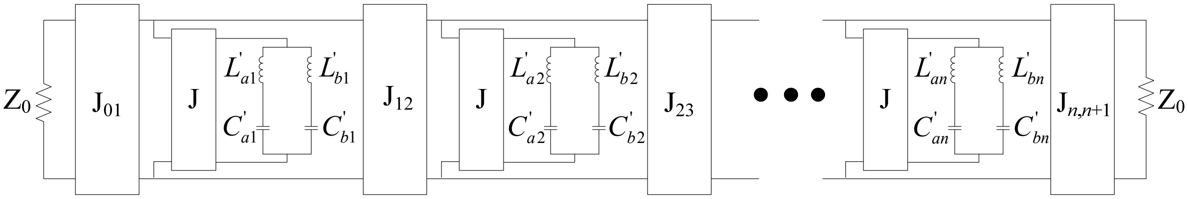

Fig. 4-8. Transformed DBBPF using parallel composite resonator [29].

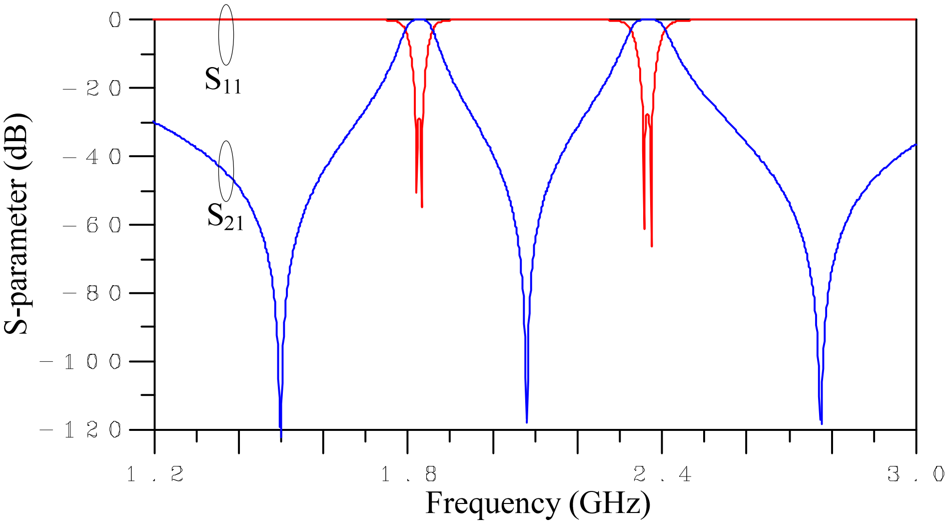

Fig. 4-9. Circuit simulated S-parameters of DBBPF in Fig. 4-8.

$$L_a^{'} = \frac{C_a}{J^2} \tag{4.14}$$

$$C_b^{'} = L_b J^2 \tag{4.15}$$

$$L_b^{'} = \frac{C_b}{J^2} \tag{4.16}$$

In (4.13)-(4.16), the J-inverters are arbitrarily determined values, but their values are limited for realizable microstrip line fabrication. Fig. 4-8 shows the transformed DBBPF using parallel composite resonator. In the transformation process of Fig. 4-7, additional J-inverter value has been set to 0.1, which is the same as the characteristic impedance of 10 ohm. The line length for the J-inverter is a quarter wavelength at ω_0 determined from (4.8). The transformed lumped element values in Fig. 4-8 are C_{a1} (C_{a2})=1.113 pF, L_{a1} (L_{a2})=7.02 nH, C_{b1} (C_{b2})=0.834 pF, and L_{b1} (L_{b2})=5.26 nH. Fig. 4-9 presents the circuit simulated S-parameters of the transformed DBBPF. As shown in the Fig. 4-9, the transformed DBBPF produces transmission zeros at 1.5, 2.08, and 2.78 GHz. Due to these transmission zeros, the transformed DBBPF achieves shaper frequency cutoff characteristic than initial DBBPF in Fig. 4-4.

In order to fabricate the DBBPF using the microstrip, lumped series resonators in Fig. 4-8 should be converted to a microstrip stub. Fig. 4-10 illustrates the lumped series resonator transformation to its equivalent microstrip open stub. The reactance of the lumped series resonator in Fig. 4-10 (a) can be written as (4.17), and the slope parameter of (4.17) is presented in (4.18).

$$X_{in} = \omega L_a - \frac{1}{\omega C_a} \tag{4.17}$$

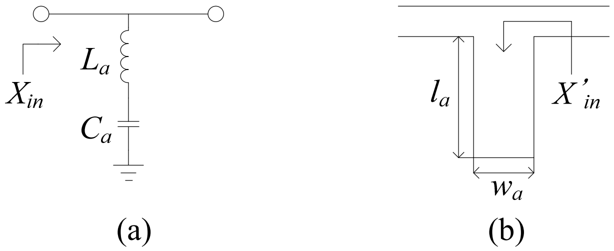

(a) (b)

Fig. 4-10. (a) Lumped series LC resonator and (b) its equivalent quarter wavelength microstrip open stub.

$$\frac{d}{d\omega} X_{in}\Big|_{\omega=\omega_a} = 2L_a \tag{4.18}$$

Microstrip open stub in Fig. 4-10 (b) is a quarter wavelength at ω_a, so the microstrip line length can be shown as (4.19). The reactance of the open stub in Fig. 4-10 (b) can be written as (4.20), and its slope parameter is in (4.21).

$$l_a = \frac{\lambda_{g,a}}{4} = \frac{c}{4f\sqrt{\varepsilon_{eff}}} = \frac{\pi c}{2\omega_a\sqrt{\varepsilon_{eff}}} \tag{4.19}$$

$$X_{in}^{'} = -Z_a \cot(\beta \cdot l_a) = -Z_a \cot\left(\frac{\pi}{2} \cdot \frac{\omega}{\omega_a}\right) \tag{4.20}$$

$$\frac{d}{d\omega} X_{in}^{'}\Big|_{\omega=\omega_a} = \frac{Z_a \pi}{2\omega_a} \tag{4.21}$$

By equating (4.18) and (4.21), (4.22) can be derived. Using (4.19) and (4.22), the microstrip open stub length and width can be determined.

$$Z_a = \frac{4\omega_a L_a}{\pi} \tag{4.22}$$

4.3 Triple-Band BPF Synthesis

This section introduces a TBBPF design using admittance inverters and parallel *LC* resonators. Three shunted parallel *LC* resonators are connected in series to produce a triple-bandpass response. In the proposed TBBPF design, each center frequency and fractional bandwidth (*FBW*) of low, mid, and high bands can separately be controlled. In order to demonstrate the design methodology, simulated results are compared with measured results. For a filter fabrication using microstrip, the TBBPF is designed at a center frequency of 1.8, 2.4, and 3 GHz. *FBW* is set to 4 % in all passbands, and the number of filter stages is N=2. The designed TBBPF shows good agreement in simulated and measured results.

Fig. 4-11 (a) presents a triple-band resonator (TBR) consisting of three parallel *LC* resonators. The parallel *LC* resonators are serially connected in shunt to produce triple passband. If the resonator's element values are properly chosen, the TBR could produce triple passband with two transmission zeros between low and high bands.

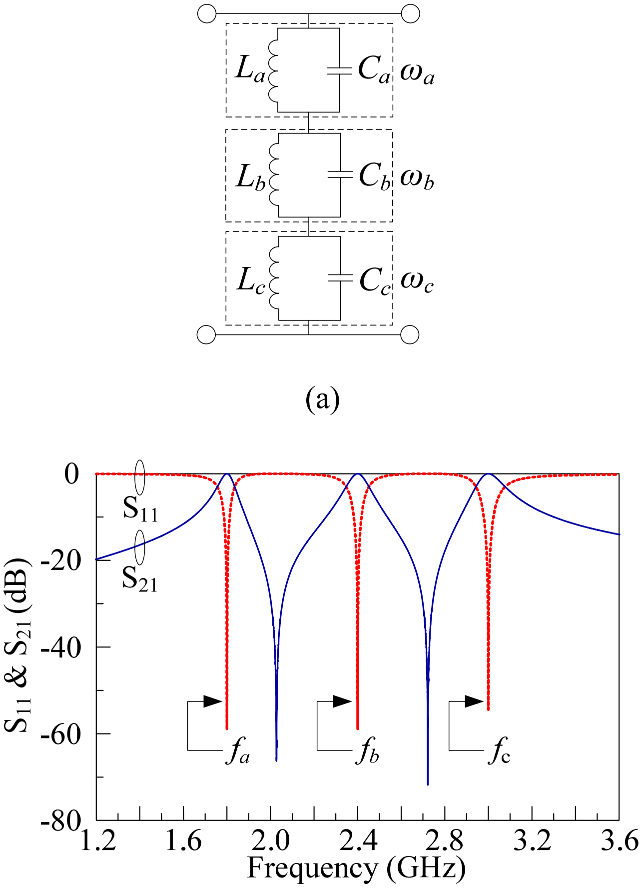

(a)

(b)

Fig. 4-11. Circuit configuration of (a) triple-band lumped resonator (L_a=0.09772 nH, C_a=80 pF, L_b=0.07329 nH, C_b=60 pF, L_c=0.05863 nH, and C_c=48 pF) and (b) simulated frequency response.

For a given center frequency of 1.8, 2.4, and 3 GHz, a frequency response of the TBR is illustrated in Fig. 4-11 (b), where capacitance values are arbitrarily selected, and inductance values are then obtained from:

$$L_r = \frac{1}{\omega_r^2 C_r} \text{ , where } r = a,\ b, \text{ or } c. \tag{4.23}$$

Fig. 4-12 shows a TBBPF equivalent circuit consisting of J-inverters and TBRs. The capacitance values of the TBR in Fig. 4-12 could be determined from:

$$C_{ri} = \frac{\Omega_c g_i G_0}{FBW_r \omega_r} \ . \tag{4.24}$$

where $FBW_r = (\omega_u - \omega_l)/\omega_r$, $\omega_r = (\omega_u \omega_l)^{1/2}$, and ω_u and ω_l are upper and lower 3 dB cutoff frequencies of each band. Ω_c and g_i are prototype lowpass filter's cutoff frequency and element value, respectively.

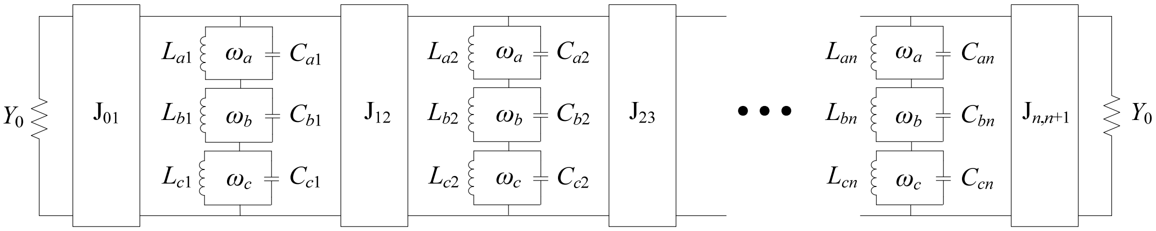

Fig. 4-12. Equivalent circuit model of TBBPF using J-inverters and parallel *LC* resonators.

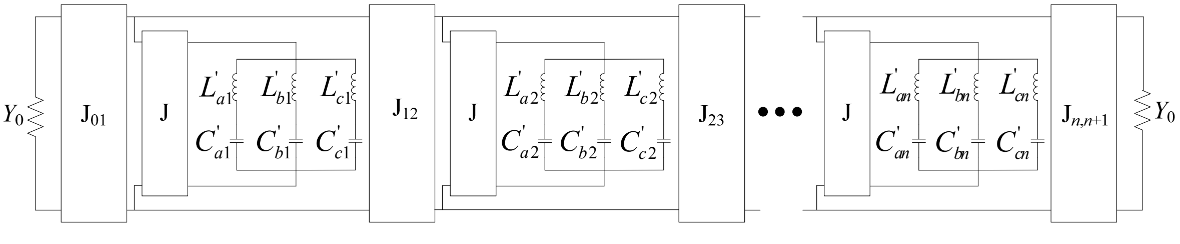

Fig. 4-13. Equivalent circuit model of transformed TBBPF by additional J-inverters.

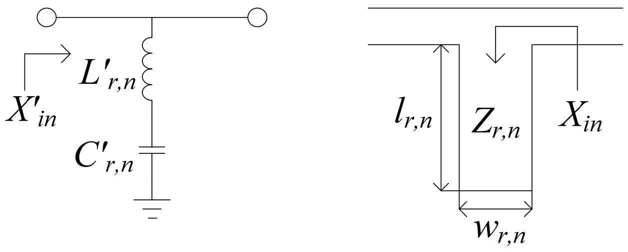

(a) (b)

Fig. 4-14. Equivalent model of (a) lumped series *LC* resonator and (b) distributed element.

The expression in (4.24) is derived from impedance scaling and frequency transformation of the prototype lowpass filter elements (g_i). Once the capacitance values are found, inductance values in Fig. 4-12 are then calculated from (4.23). J-inverters in Fig. 4-12 are realized by a quarter wavelength transmission line. Even though a quarter wavelength line is relatively narrow-band in nature, it can satisfactorily be used as an impedance or admittance inverter [1]. Here, J-inverter values in Fig. 4-12 should be in a reasonable range for fabrication because J-value results in a microstrip line width, i.e., $Z_o=1/Y_o$ and Y_o=J. If capacitance values are known, J-inverter values are then determined from:

$$J_{0,1}=\sqrt{\frac{FBW_r G_0 \omega_r C_{r1}}{\Omega_c g_0 g_1}} \tag{4.25}$$

$$J_{i,i+1}=\frac{FBW_r \omega_r}{\Omega_c}\sqrt{\frac{C_{ri}C_{ri+1}}{g_i g_{i+1}}}\Bigg|_{i=1 \text{ to } n-1} \tag{4.26}$$

$$J_{n,n+1}=\sqrt{\frac{FBW_r G_{n+1} \omega_r C_{rn}}{\Omega_c g_n g_{n+1}}} \text{ ,where } r=a,\ b, \text{ or } c. \tag{4.27}$$

In (4.25)-(4.27), C_{ai}, C_{bi}, or C_{ci} can be used for the J-inverter calculations because it is assumed that an inverter value is constant over the triple-band. By substituting (4.24) into (4.25)-(4.27), one may instantly notice that J-values in (4.25)-(4.27) are always determined as G_0, which corresponds to 50 Ω line. Here, the transmission line length must be a quarter guided wavelength at the frequency of:

$$\omega_m = \frac{\omega_a + \omega_c}{2} \tag{4.28}$$

where ω_a and ω_c are the center frequencies of 1st and 3rd passbands, respectively.

Since it is difficult to realize parallel TBRs with distributed elements on microstrip, the circuit in Fig. 4-12 is converted to Fig. 4-13 by using:

$$L'_{r,n} = \frac{C_{r,n}}{J^2} \tag{4.29}$$

$$C'_{r,n} = J^2 L_{r,n} \tag{4.30}$$

where, $r=a$, b, or c, and $n=1$ to n.

In (4.29) and (4.30), J is arbitrarily determined. After transformation using additional inverters, lumped series resonators in Fig. 4-13 can be converted to distributed elements. The input reactance in Fig. 4-14 (a) is written as:

$$X'_{in} = \omega L'_{r,n} - \frac{1}{\omega C'_{r,n}} \tag{4.31}$$

and its slope parameter is then derived:

$$\frac{\omega_r}{2} \frac{d}{d\omega} X'_{in}\Big|_{\omega=\omega_r} = \omega_r L'_{r,n} \tag{4.32}$$

The input reactance in Fig. 4-14 (b) can be presented as:

$$X_{in} = -Z_{r,n} \cot\left(\beta \cdot l_{r,n}\right) = -Z_{r,n} \cot\left(\frac{\pi}{2} \cdot \frac{\omega}{\omega_r}\right) \tag{4.33}$$

and its slope parameter is also derived as:

$$\frac{\omega_r}{2} \frac{d}{d\omega} X_{in}\Big|_{\omega=\omega_r} = \frac{Z_{r,n}\pi}{4} \tag{4.34}$$

Equating (4.32) and (4.34) leads to:

$$Z_{r,n} = \frac{4\omega_r L'_{r,n}}{\pi} \tag{4.35}$$

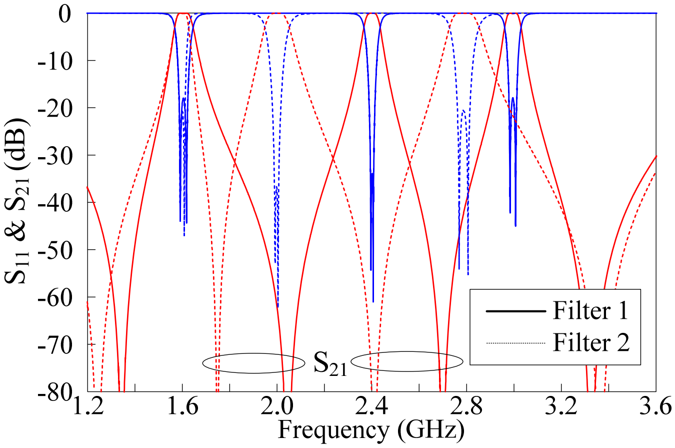

Fig. 4-15. Simulated results of Fig. 4-3, where filter1:f_a=1.6 GHz (FBW_a=0.075), f_b=2.4 GHz (FBW_b=0.05), f_c=3 GHz (FBW_c=0.04) and filter2:f_a=1.6 GHz (FBW_a=0.06), f_b=2 GHz (FBW_b=0.06), f_c=2.8 GHz (FBW_c=0.06); N=2 (Butterworth).

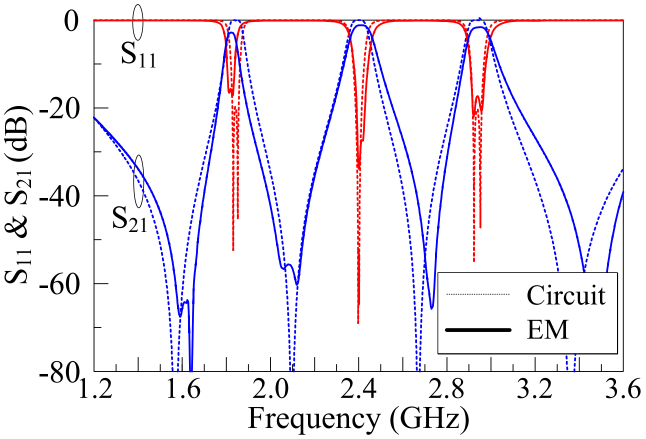

Fig. 4-16. Circuit and EM simulated results of designed TBBPF.

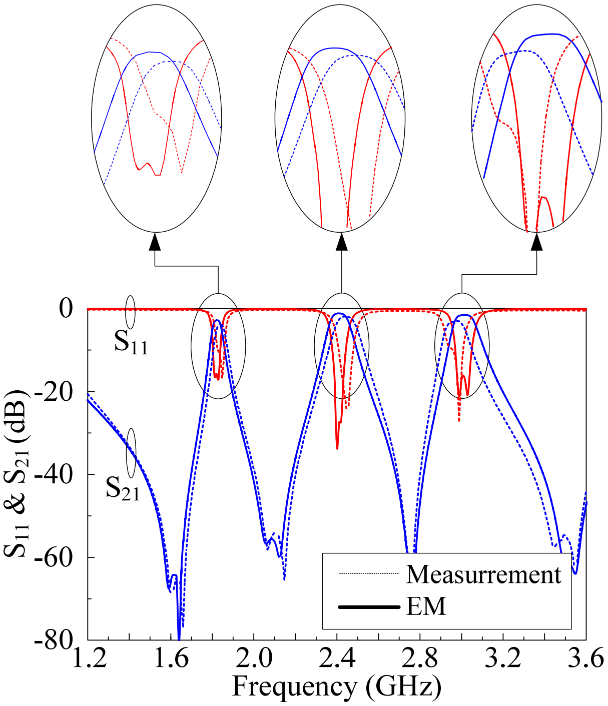

Fig. 4-17. EM simulated and measured results of designed TBBPF.

From (4.35), a stub width (W_r) in Fig. 4-14 (b) can be determined. A stub length (l_r) is a quarter guided wavelength at resonant frequency due to $L'_{r,n}$ and C'_{rn} in (7) and (8). Because $Z_{r,n}$ in (4.35) is a function of $L'_{r,n}$, an arbitrary J value in (4.29) should carefully be selected for a realizable line width. When *FBW* becomes larger (smaller), J value in (4.29) should also increase (decrease) for a reasonable line width.

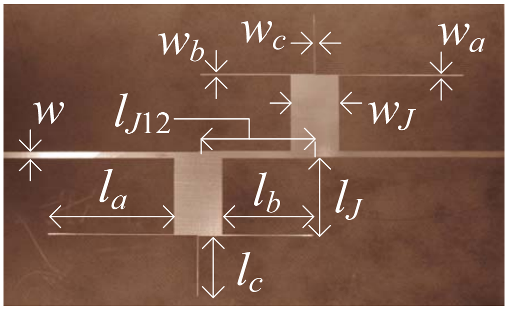

Fig. 4-18. Fabricated microstrip TBBPF (l_{J12}=22.8, l_J=22.4, l_a=30, l_b=21.35, l_c=18.45, w=1.5, w_J=11.5, w_a=0.3, w_b=0.5, w_c= 0.3 mm).

Fig. 4-15 illustrates simulated results of designed two TBBPFs and their design specifications. As shown in the Fig. 4-15, center frequency and *FBW* of each band can separately be adjusted. In filter 1, the bandwidth is fixed as 120 MHz.

TBBPF is designed and fabricated using design parameters of f_a=1.8, f_b=2.4, f_c=3.0 GHz, *N*=2 (Butterworth), *FBW*=0.04 for all bands. Figs. 47 and 48 compare simulated and measured results. Fig. 4-18 illustrates the photo of the fabricated TBBPF. Measured insertion losses at each band were less than 3 dB, and return losses were greater than 15 dB within passband. Both simulated and measured results have shown good agreement.

4.4 Conclusions

In this Chapter IV, a triple-band bandpass filter (TBBPF) design has been introduced based on lumped triple-band parallel *LC* resonators and admittance inverters. Since the proposed TBBPF produces transmission zeros between passbands, high selectivity can be achieved with smaller number of filter stages. For given center frequencies of TBBPF, if *FBW* increases, resonator's capacitance values decrease in (4.24). These decreased capacitance values lower the characteristic impedance in (4.35). From the experiment, it has been found that the proposed TBBPF can favorably be designed for *FBW* up to 20 % by appropriately selecting J-inverter values in (4.29) and (4.30). The design methodology is validated through simulations and measurements. The circuit and EM simulated results show good agreement with the measured data.

CHAPTER V

COMPACT BANDPASS FILTER DESIGN USING SPLIT RING RESONATORS

5.1 Introduction

In this chapter, a coupled type complementary split ring resonator (CSRR) is introduced for a compact direct-coupled bandpass filter (BPF). The proposed unit cell of the resonator consists of two CSRRs, where gaps of outside rings face each other to achieve a strong cross coupling. For an analysis of the coupled CSRR, an equivalent circuit model is discussed and validated through circuit and EM simulations. Based on the coupled CSRR structure, two-/four- pole direct-coupled BPFs are designed, simulated, and measured. Their equivalent circuit models are also presented and validated from comparing simulated and measured results. The designed BPFs utilizing the coupled CSRRs provide a sharp frequency cutoff, low insertion loss, and compact size. The BPFs are designed at the center frequency of 2.45 GHz. The designed two-pole BPF shows fractional bandwidth (*FBW*) of 15 %, an insertion loss of less than 1 dB, and a size of $0.11\lambda_g \times 0.22\lambda_g$. The four-pole BPF demonstrates *FBW* of 20 %, an insertion loss of less than 2.8 dB, and a size of $0.33\lambda_g \times 0.45\lambda_g$. The simulated and measured results of both designed BPFs show good agreement.

The microstrip band-pass filter (BPF) is one of the most widely used components in RF/microwave systems since it controls signal flows within a certain frequency band. Recently, many filters have been developed to meet today's filter requirements including low-insertion loss, compact size, and low cost. For these needs, filter designs using complimentary split ring resonator (CSRR) have been studied by many researchers, and reported [33]-[36]. In [36], a BPF was designed by combining a lowpass filter (LPF) and highpass filter (HPF). The design method presented in [36] has an advantage for bandwidth tuning, which relies on cutoff frequencies of LPF and HPF. However, this cascaded structure could increase an insertion loss of the filter. As shown in [36], it is also difficult to achieve a flat passband when the bandwidth becomes narrow. In addition, cascading two different filters would have a disadvantage of reducing a circuit size. For these reasons, a simple filter structure is preferable for a low insertion loss and size reduction.

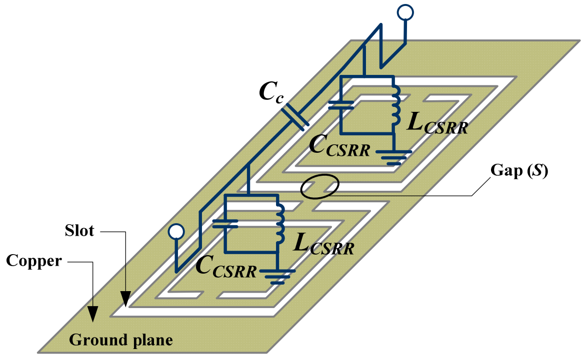

Fig. 5-1. Proposed unit cell of coupled CSRR and its lumped equivalent circuit model.

Even though a filter design using resonators mostly relies on coupling coefficient and input/output external Q-factor, an analysis and modeling are also important to give an insight for a filter design. This paper introduces compact direct- coupled BPF designs and their equivalent circuit models.

A general design methodology and lumped equivalent circuit models of a direct coupled BPF have already been described in [5]. A direct-coupled BPF could be a capacitive- or an inductive- coupled structure. Frequency responses of the direct-coupled BPFs normally show asymmetric attenuation characteristics. A direct capacitive-coupled BPF produces a slow attenuation slope in upper frequency cutoff region due to series capacitances. On the other hand, a direct inductive-coupled BPF shows a slow attenuation slope in lower frequency cutoff region because of series inductances.

Fig. 5-1 illustrates the proposed unit cell of capacitive-coupled CSRRs. As shown in Fig. 5-1, two pairs of square rings are etched off from a ground plane, where gaps (S) of the outside rings face each other to enhance the coupling (C_c) between the two CSRRs. As the gaps (S) become narrower, a stronger coupling is obtained due to the focused electric field within the gaps. An equivalent circuit model for a conventional CSRR has been investigated in [37], where slotted complimentary square rings in a ground plane are represented as a parallel LC resonator. The lumped equivalent circuit model for the proposed coupled CSRRs is shown in Fig. 5-1, where parallel LC (C_{CSRR} and L_{CSRR}) shunt resonators are connected with a series capacitor (C_c).

Proposed BPFs are simulated and fabricated on Rogers 5880 with a substrate thickness of 0.508 mm. A low dielectric constant substrate has been used to minimize the dielectric loading effects on miniaturization.

5.2 Two Pole Coupled BPF Design Using CSRR

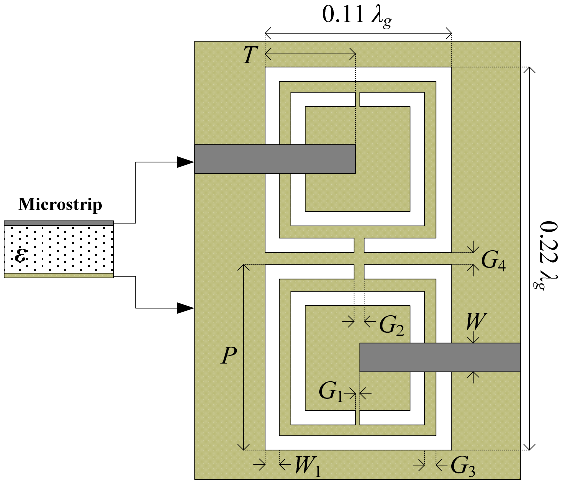

Fig. 5-2. Proposed two pole direct-coupled BPF using one coupled CSRR.

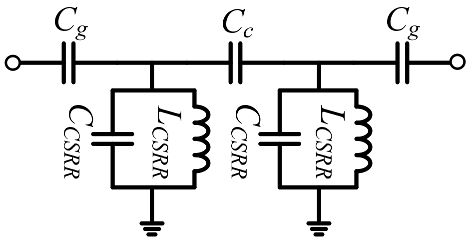

Fig. 5-3. Equivalent circuit model of proposed two pole direct coupled BPF.

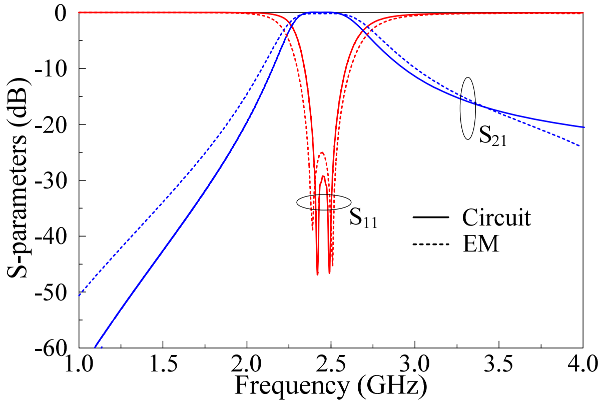

Fig. 5-4. Circuit and EM simulated results of two pole direct-coupled BPF.

Fig. 5-2 illustrates two pole direct-coupled BPF using a unit cell capacitive-coupled CSRR structure. It should be noticed that gaps in CSRR's outside rings must face each other to generate enough coupling so that it could produce passband. If the gaps are not faced each other, the passband is not created due to a low coupling. Equivalent circuit model of the proposed two pole direct-coupled BPF is shown in Fig. 5-3. The filter's center frequency is a function of CSRR dimensions (P, W_1, G_1, G_2, and G_3), which result in C_{CSRR} and L_{CSRR}. The lumped element values (C_{CSRR} and L_{CSRR}) for the given CSRR dimensions can be evaluated as in [37]. Since it is difficult to obtain analytical solutions for equivalent element values of the circuit structure in Fig. 5-2, other element values (C_g and C_c) are experimentally determined by fitting circuit simulated results to EM simulated one [35] and [36]. Bandwidth of the filter is affected by C_c. Thus, if C_{CSRR} and L_{CSRR} are known, C_c which achieves the same bandwidth to EM simulation can be found with C_g. In Fig. 5-2, the longer feed line length (T) above CSRR produces the bigger coupling capacitance, C_g, and smaller gap dimensions of G_2 and G_4 result in a larger C_c.

The designed filter dimensions in Fig. 5-2 are P=9.8, W_1=0.8, G_1=0.2, G_2=0.4, G_3=0.5, G_4=0.4, and T=4.8 mm. Feed line width, W is set to 1.6 mm which corresponds to 50 Ω line. Lumped element values for the given dimensions are found as C_g=0.67, C_C=0.28, C_{CSRR}=1.45 pF, and L_{DSRR}=1.9 nH. Circuit and EM simulated results are shown in Fig. 5-4, where two resonant poles due to two shunted parallel LC resonators are observed.

5.3 Four Pole Coupled BPF Design Using CSRR

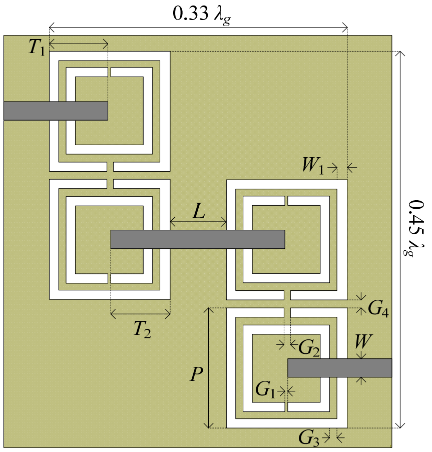

Fig. 5-5. Proposed four pole direct-coupled BPF using two coupled CSRRs.

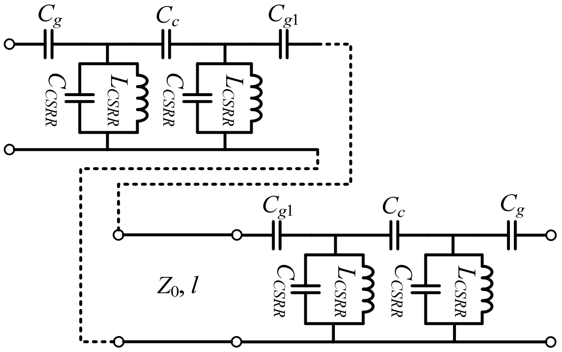

Fig. 5-6. Equivalent circuit model of four pole direct-coupled BPF.

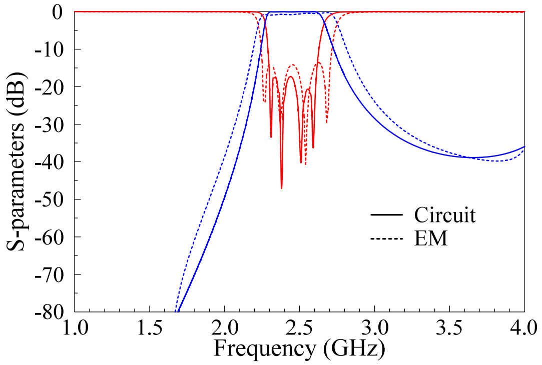

Fig. 5-7. Circuit and EM simulated results of four pole direct-coupled BPF.

Four poles direct-coupled BPF using two coupled CSRRs is designed and presented in Fig. 5-5. Equivalent circuit model of the BPF is illustrated in Fig. 5-6. Each pair of CSRRs on a ground plane is coupled to top transmission lines, where the center line's characteristic impedance is Z_0 and the length is approximately $\lambda_g/4$ at the center frequency of 2.45 GHz. Setting the line length as a quarter guided wavelength, two identical resonators can be combined and operated as a multi mode resonator. The two identical resonators connected with a quarter guided wavelength line produce a sharper frequency cutoff and wide passband, however an insertion would increase with the number of resonators. The designed four pole BPF dimensions are P=9.8, W_1=0.8, G_1=0.2, G_2=0.5, G_3=0.5, G_4=0.4, T_1=4.7, T_2=4.3, and L=21.3 mm. It should be noted that L in Fig, 54 significantly affect an upper band cutoff slop, so it is optimized to achieve a sharp upper cutoff slope. This results in that L is slightly less than $\lambda_g/4$ at 2.45 GHz. The extracted element values are C_g=0.63 cF, C_C=0.23 pF, C_{g1}=0.5 pF, C_{CSRR}=1.45 pF, and L_{DSRR}=1.9 nH. Circuit and EM simulated results of the four pole direct-coupled BPF are illustrated in Fig. 5-7. Measured results of the fabricated two-/four-pole direct coupled BPFs are presented in Figs. 5-8 and 5-9, respectively. Photo of the fabricated four pole direct-coupled BPF is illustrated in Fig. 5-10. EM simulated and measured results show good agreement.

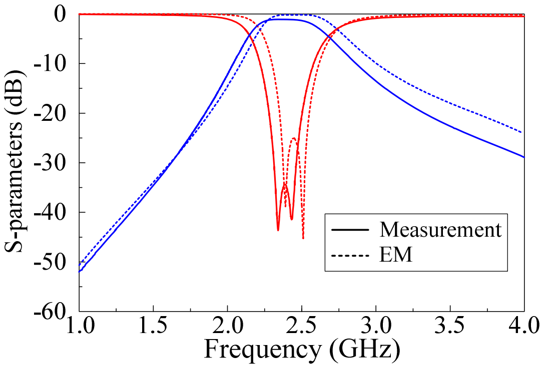

Fig. 5-8. EM simulated and measured results of two pole direct-coupled BPF.

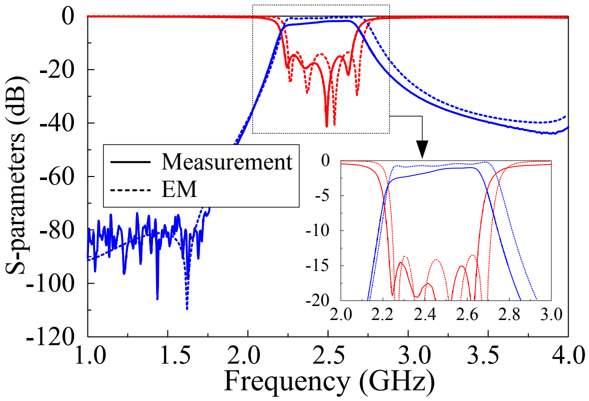

Fig. 5-9. EM simulated and measured results of four pole direct-coupled BPF.

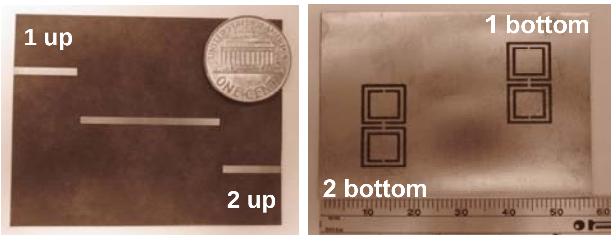

Fig. 5-10. Photo of fabricated four pole direct-coupled BPF.

5.4 Conclusions

A compact direct-coupled BPF using coupled CSRRs has been introduced. Their equivalent circuit models have also been presented and validated through circuit and EM simulations. At the center frequency, the dimensions of the designed two-/four- pole BPFs are $0.11\lambda_g \times 0.22\lambda_g$ and $0.33\lambda_g \times 0.45\lambda_g$, respectively. Measured insertion losses of the both filters are found as less than 1 and 2.8 dB within passband, and return losses were greater than 20 and 15 dB. Both simulated and measured results of the designed filters show good agreement.

CHAPTER VI

MODELING OF VERSATILE DUMBBELL SHAPED-SLOT RESONATOR (DSSR)*

6.1 Introduction

This chapter presents a dumbbell-shaped slot resonator (DSSR) for miniaturized lowpass filter (LPF) and bandpass filter (BPF) designs. Based on circuit theory and an electromagnetic (EM) simulation, the DSSR's lumped and distributed equivalent circuit models are presented and validated. The proposed DSSR does not employ a ground slot, so the fabrication process is simple. This allows one to minimize cost and fabrication errors. Using the DSSRs, a miniaturized LPF and BPF are designed, simulated, and measured. The dimensions of the fabricated LPF are $0.27\lambda_g\times0.17\lambda_g$ at a cutoff frequency of 3.4 GHz, and a measured insertion loss of less than 1 dB and a return loss of greater than18 dB have been achieved. The dimensions of the fabricated BPF are $0.37\lambda_g \times 0.27\lambda_g$ at a center frequency of 7.35 GHz, and an insertion loss of less than 3 dB and a return loss of greater than 15 dB have been achieved. The designed BPF provides a fractional bandwidth (FBW) of 2%. Both simulated and measured results of the designed filters show good agreement. The proposed filters do not utilize stubs or other circuit elements, so the filters are compact in size.

---

*Parts of this chapter are reprinted with permission from D.-J. Jung and K. Chang, "Miniaturized bandpass filter using dumbbell-shaped slot resonator," *IET Electron. Lett.*, vol. 48, pp. 100-102, Jan. 2012. Copyright 2012 IET.; D.-J. Jung and K. Chang, "Accurate modeling of microstrip dumbbell shaped slot resonator (DSSR) for miniaturized tunable resonator and bandpass filter," *Progress In Electromagnetics Research C*, vol. 23, pp. 137-150, 2011. Copyright 2011 EMW.

The microstrip resonator is one of the most widely used components in RF/microwave and millimeter wave circuits. Many types of microstrip resonators have been reported [38]-[42] and employed in both passive and active applications. Microstrip resonators are especially essential for planar type filter designs [43]-[46] because they are used to produce a frequency passband. For this reason, compact and simple resonators are preferred to meet today's filter design requirements.

In this chapter, a dumbbell-shaped slot resonator (DSSR) is introduced for miniaturized lowpass filter (LPF) and bandpass filter (BPF) designs. The proposed DSSR can be compared with a dumbbell-shaped defected ground structure (DGS) described in [8] and [9] since the geometry and analysis are similar. However, there are distinctive differences between the dumbbell-shaped DGS and the DSSR. The dumbbell-shaped DGS utilizes slotted ground structures. Thus, a top microstrip line and a ground slot should be precisely aligned in the fabrication process. Fabrication errors can increase because of the alignment difficulty, which ultimately affects insertion and return losses of a circuit. On the other hand, the DSSR does not employ ground slots, therefore the fabrication process is simpler. As presented in [8] and [9], LPF design using the DGS utilizes shunt capacitive stubs. In a BPF design as shown in [47] and [48], the DGS should be used with another BPF or resonant circuit to produce a frequency passband. This could make it difficult to reduce the circuit size. However, in LPF and BPF designs using the DSSRs, shunt capacitive stubs or other circuit elements are not necessary.

All circuits in the chapter are fabricated on Rogers 5880 substrate with a thickness of 0.508 mm, and they are measured using an HP 8510 vector network analyzer. A low dielectric constant substrate has been used to minimize the dielectric loading effect on miniaturization.

6.2 Modeling of DSSR

Fig. 6-1 presents the proposed prototype DSSR. Each square slot ($D \times D$) is connected with another rectangular slot ($G \times W$). The input and output microstrip line widths (W) of the DSSR are set to a 50Ω line impedance. Fig. 6-2 illustrates the DSSR's equivalent circuit using a distributed model. The distributed equivalent circuit model of the DSSR can be instantly obtained from the DSSR's geometrical structure. However, this distributed equivalent circuit model may not account for the parasitic element effects. In this section, the DSSR's distributed equivalent circuit model is studied with the lumped equivalent circuit model. Both distributed and lumped equivalent circuits are validated through a circuit and EM simulations.

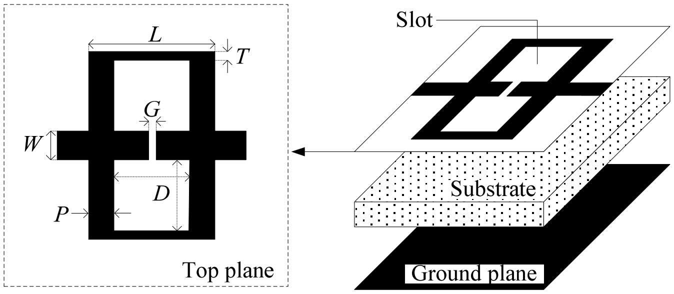

Fig. 6-1. Proposed prototype dumbbell-shaped slot resonator (DSSR) on microstrip.

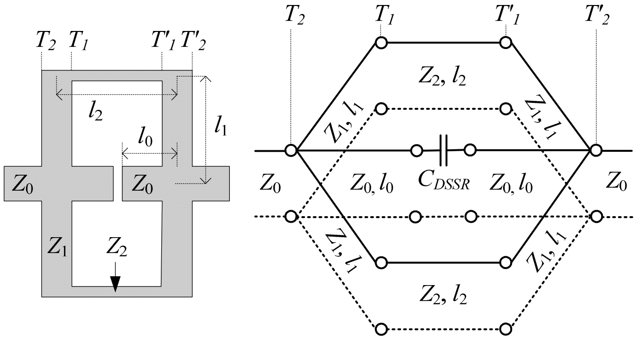

(a) (b)

Fig. 6-2. Prototype (a) DSSR and (b) distributed equivalent circuit model.

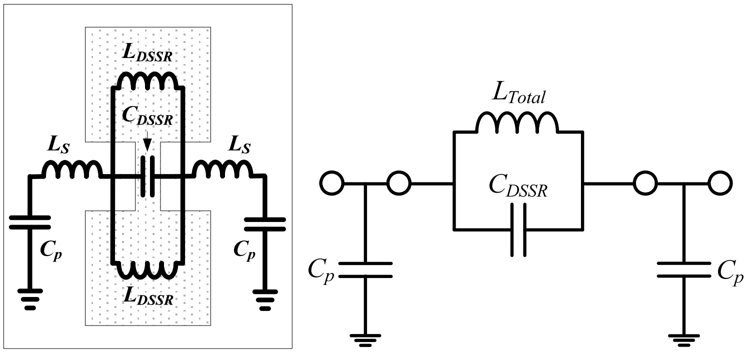

(a) (b)

Fig. 6-3. DSSR's lumped equivalent circuit models; (a) complete model and (b) simplified model.

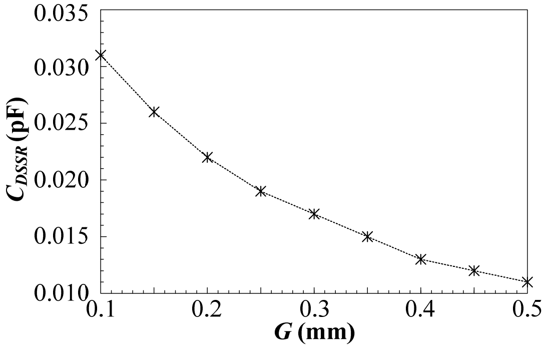

Fig. 6-4. C_{DSSR} versus gap dimension (G).

Fig. 6-3 depicts the lumped equivalent circuit model of the DSSR. In Fig. 6-3 (a), two square slot areas ($D \times D$) produce an inductance (L_{DSSR}), and a capacitive coupled gap separated by a gap dimension (G) generates a capacitance (C_{DSSR}).

The series inductance (L_S) and the parallel capacitance (C_p) are mainly caused by the transmission line sections (Z_1, l_1 and Z_0, l_0) in Fig. 6-2. The impedance (Z_{DSSR}) excluding the parallel capacitor (C_P) in Fig. 6-3 (a) is written as:

$$Z_{DSSR} = j\omega\left(2 \cdot L_S + \frac{L_{DSSR}}{2 - \omega^2 L_{DSSR} C_{DSSR}}\right) \tag{6.1}$$

where Z_{DSSR} is purely inductive when $\omega^2 L_{DSSR} C_{DSSR} < 2$. It should be noted that the DSSR's resonant pole, $[\omega_0 = 2/(L_{DSSR} C_{DSSR})]^{1/2}$ appears at a much higher frequency region than the DSSR's operating frequency range due to very low C_{DSSR}. As a result, $\omega^2 L_{DSSR} C_{DSSR}$ becomes very close to zero in the DSSR's operating frequency range ($\omega << \omega_0$). Thus, in the operating frequency region, the inductance (L_{Total}) of the simplified equivalent circuit model in Fig. 6-3 (b) can be written as:

$$L_{Total} \approx 2L_S + \frac{L_{DSSR}}{2}. \tag{6.2}$$

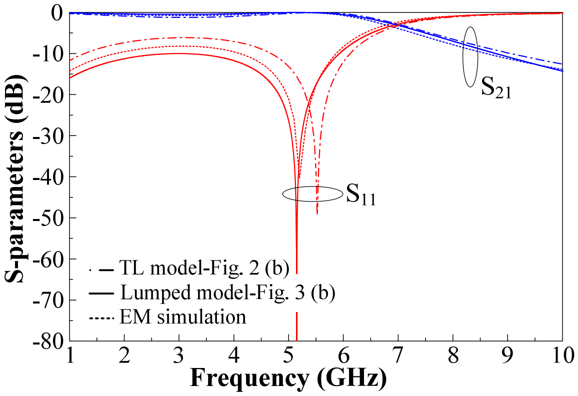

Fig. 6-5. Circuit and EM simulated results of DSSR (*D*=3, *G*=0.2, *L*=7.4, *W*=1.56, *P*=2.2, and *T*=0.2 mm).

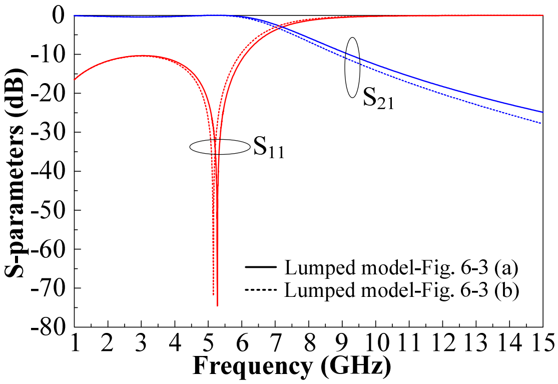

Fig. 6-6. Comparison of lumped equivalent circuit models in Fig. 6-3 (a) and (b).

Fig. 6-4 illustrates the capacitively coupled capacitance (C_{DSSR}) separated by the gap dimension (G) with a line impedance of Z_0. The parallel capacitance (C_p) in Fig. 6-3 (a) and (b) can be determined using:

$$C_p(F) = \frac{\varepsilon_0 \varepsilon_r A}{h} \tag{6.3}$$

where ε_0=8.854×10^{-12} F/m, A=microstrip size (in m^2), and h=substrate thickness (in m).In order to validate the proposed equivalent circuit models in Fig. 6-2 (b) and Fig. 6-3 (b), the circuit simulated results are compared with EM simulated results. The DSSR dimensions in Fig. 6-1 have arbitrarily been selected as D=3, G=0.2, L=7.4, W=1.56, P=2.2, and T=0.2 mm. The exact value of C_{DSSR} is determined as 0.022 pF from coupled line gap modeling. From (6.3), using A=19.7×10^{-6} m^2 and h=0.508×10^{-3} m, C_P is determined to be 0.76 pF. Then, L_{Total} in Fig. 6-3 (b) can be determined by:

$$L_{Total}(H) = \frac{1}{f_{ar}^2 4\pi^2 C_{DSSR}} \tag{6.4}$$

where f_{ar}=arbitrary anti-resonant frequency (S_{21} pole) due to L_{Total} and C_{DSSR}. f_{ar} is determined as a frequency which results in the same cutoff slope to the EM simulated result. Using C_{DSSR}=0.022 pF and C_P=0.76 pF, a circuit simulation of Fig. 6-3 (b) reveals f_a=28.18 GHz with L_{Tota} of 1.45 nH. These f_a and C_{DSSR} values satisfy (6.4).

Fig. 6-5 compares the circuit and EM simulated results. The circuit simulated results using Fig. 6-3 (b) show good agreement to the EM simulated results, but the resonant pole of the Fig. 6-2 (b) is slightly shifted from the EM simulation results. However, as shown in Fig. 6-5, the distributed equivalent circuit model in Fig. 6-2 (b) still provides a reasonable agreement to the DSSR's frequency response characteristics.

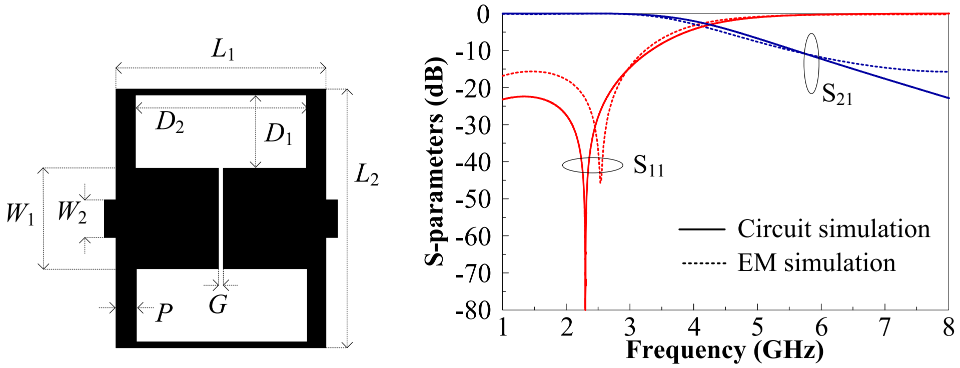

(a) (b)

Fig. 6-7. Modified DSSR for L_{DSSR} and C_{DSSR} enhancement; (a) top view of modified DSSR (L_1=8.6, L_2=10.56, D_1=3, D_2=7, G=0.2, P=0.8, W_1=4.16, and W_2=1.56 mm) and (b) circuit/EM simulated results of modified DSSR.

Since L_{Total} has been determined, L_{DSSR} can also be calculated from (6.2). Here, L_S should be known for the L_{DSSR} calculation. L_S can be determined from [9]:

$$L_S = \frac{Z_0}{\omega_c}\sin(\theta) = \frac{Z_0}{\omega_c}\sin\left(\frac{2\pi}{\lambda_{0c}} \cdot \sqrt{\varepsilon_{eff}} \cdot l_S\right) \qquad (6.5)$$

where ω_c, λ_{0c}, and l_S are the cutoff frequency of the DSSR, free space wavelength at ω_c, and physical line length, respectively. The equation in (6.5) is derived from an even and odd mode analysis of a transmission line. The cutoff frequency of 7.07 GHz has been found from the EM simulated results in Fig. 6-5. For the given DSSR dimensions, two line sections (7.96 mm×2.2 mm and 1.56 mm×1.4 mm, i.e., width × length) correspond to a characteristic impedance of 14 and 50 Ω. Using these characteristic impedances and line lengths, the inductances in (6.5) are calculated as 0.14 and 0.31 nH, respectively. As a result, by substituting L_S= 0.45 nH into (6.2), L_{DSSR}= 1.1 nH is determined. Since L_S and L_{DSSR} have been found, the lumped equivalent circuit models in Figs. 6-3 (a) and (b) can be compared. Fig. 6-6 presents the circuit simulated S-parameter results, and the results validate the approximation in (6.2) and the simplified equivalent circuit model in Fig. 6-3 (b).

6.3 LPF Design Using DSSR

Fig. 6-7 (a) shows the modified DSSR which results in increased L_{DSSR} and C_{DSSR} values. In Fig. 6-7 (a), widening the rectangular slot ($D_1 \times D_2$) increases L_{DSSR}. Narrowing the gap (G) and widening the line width (W_1) enhance C_{DSSR}. For an investigation of the modified DSSR in Fig. 6-7 (a), the dimensions have arbitrarily been selected as: L_1=8.6, L_2=10.56, D_1=3, D_2=7, G=0.2, P=0.8, W_1=4.16, and W_2=1.56 mm.

An equivalent circuit model of the modified DSSR is assumed to be the same as Fig. 6-3 (b). The capacitive coupled capacitance, C_{DSSR} is found to be 0.06 pF from a microstrip coupled gap modeling. From (6.3), using A=22.6×10^{-6} m^2 and h=0.508×10^{-3} m, C_P is determined as 0.87 pF. The calculated C_P and C_{DSSR} values are assumed to be the exact values which do not necessitate further optimization. From (6.4), L_{Total} is validated as 2.8 nH when f_{ar} is 12.28 GHz. Fig. 6-7 (b) illustrates circuit and EM simulated S-parameters of the modified DSSR. The results still show reasonable agreement, and this demonstrates that Fig. 6-3 (b) is acceptable as an equivalent circuit model of Fig. 6-7 (a).

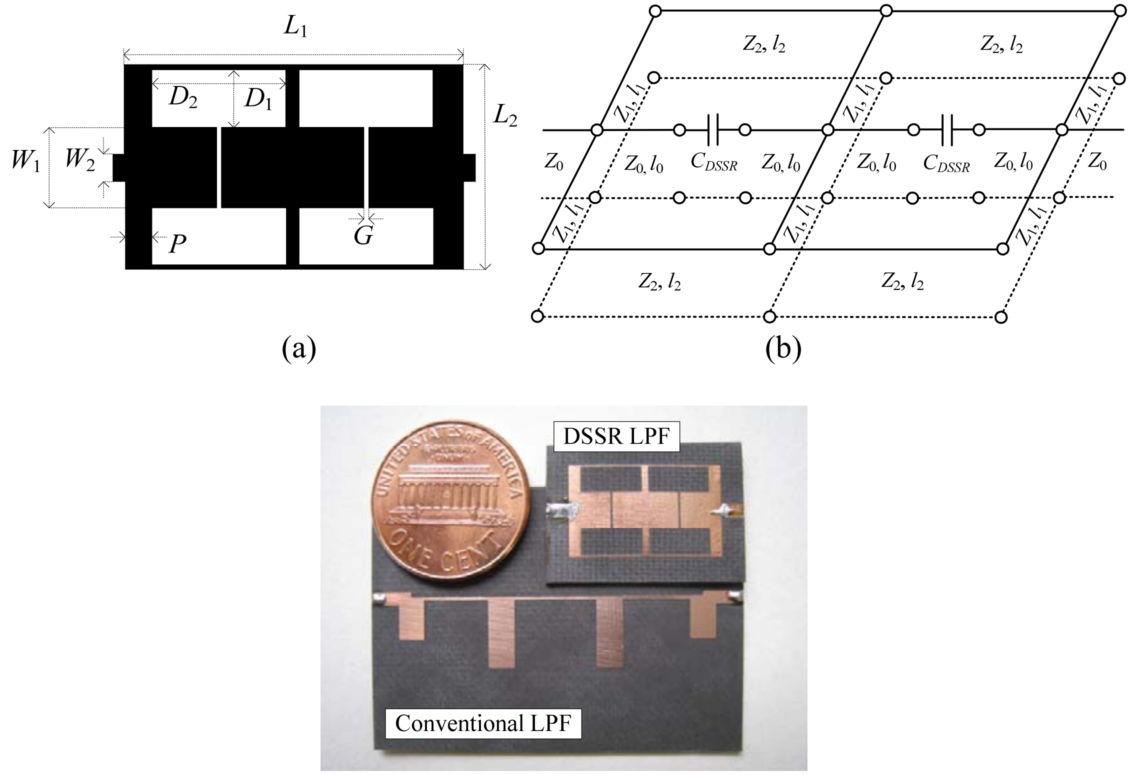

(a) (b)

(c)

Fig. 6-8. Proposed miniaturized LPF design using two modified DSSRs; (a) DSSR LPF circuit configuration, (b) equivalent circuit model, and (c) comparison of fabricated DSSR LPF and conventional LPF.

Fig. 6-8 (a) depicts the proposed microstrip miniaturized LPF employing two modified DSSRs, where L_1 and P are set to 17.6 and 1.4 mm, respectively. Other DSSR dimensions are the same as shown in Fig. 6-7 (a). Fig. 6-8 (b) presents a distributed equivalent circuit model of Fig. 6-8 (a). The equivalent circuit consists of transmission lines and gap coupling capacitances, C_{DSSR}. Fig. 6-8 (c) shows a photograph of the fabricated DSSR LPF, where the LPF is compared with a conventional ladder type LPF. The conventional LPF has been fabricated for comparison with the DSSR LPF. The number of stages for the conventional ladder type LPF is set to N=7 since it produces a similar cutoff slope as the DSSR LPF. Fig. 6-9 (a) presents the simulated and measured S-parameters of the proposed DSSR LPF. The simulated results agree well with the measured data. Insertion losses of the simulated and measured results are found to be less than 1 dB in the passband. Fig. 6-9 (b) compares the measured S-parameters of the DSSR LPF and the conventional ladder type LPF. In Fig. 6-9 (b), the DSSR LPF produces a transmission zero above the 3 dB cutoff frequency. Due to this transmission zero, the DSSR LPF achieves a steeper cutoff slope than the conventional ladder type LPF.

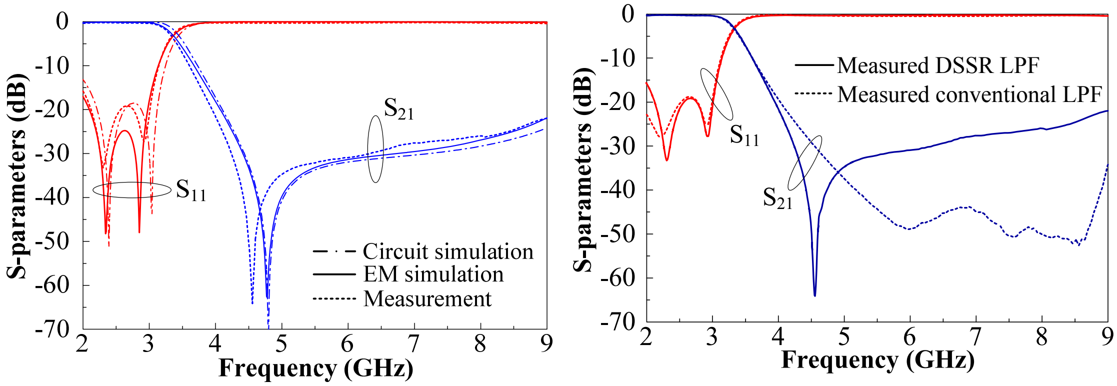

(a) (b)

Fig. 6-9. Simulated and measured S-parameters; (a) simulated and measured results of DSSR LPF and (b) comparison of DSSR LPF and conventional LPF.

6.4 Tunable DSSR Using Varactor Diode

A BPF design using the DGS in [47] employs parallel coupled line circuit elements to produce a frequency passband. Normally, complicated microstrip structures make analysis and design more difficult, and they are not helpful for circuit miniaturization. In addition, the fabrication process is complicated by a slotted ground structure. In order to minimize fabrication errors, the slotted ground region should be precisely aligned with the top microstrip line. For these reasons, a simple microstrip structure is preferable for easy analysis, design, and fabrication. A simple microstrip geometrical structure is also helpful for circuit miniaturization. In this section, BPF design using a coupled DSSR is presented. An equivalent circuit model of the coupled DSSR is provided and validated from simulated and measured results.

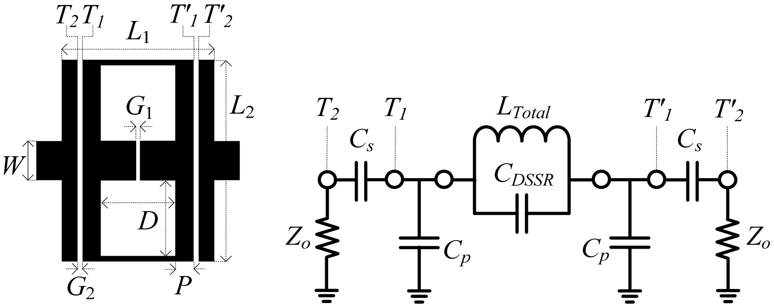

(a) (b)

Fig. 6-10. Coupled type DSSR; (a) top view of coupled DSSR (D=3, G_1=G_2=0.2, L_1=6, L_2=7.96, P=0.7, and W=1.56 mm), (b) lumped equivalent circuit model, and (c) circuit/EM simulated results.

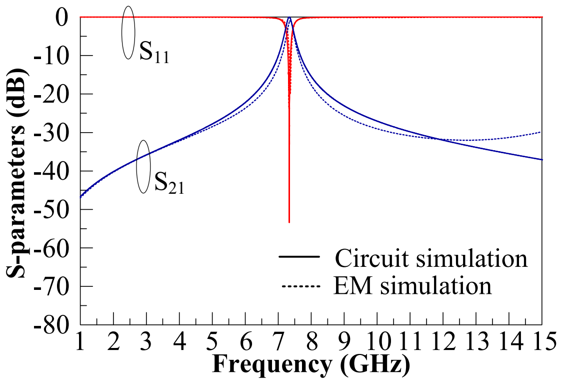

(c)

Fig. 6-10. Continued.

In the proposed BPF design using DSSRs, additional shunt stubs or other circuit elements are not necessary, so the design is simple and compact. Fig. 6-10 (a) presents the microstrip circuit configuration of a coupled DSSR. A lumped equivalent circuit model of the coupled DSSR is shown in Fig. 6-10 (b). Capacitive coupling by the gap (G_2) is modeled as a series capacitance (C_S), and the center DSSR is modeled as a parallel LC resonator with two shunt capacitances (C_P). Since the coupled DSSR utilizes a capacitive gap coupling structure, a lumped equivalent circuit model is more convenient and efficient than a distributed equivalent circuit model. The lumped equivalent circuit model could also account for parasitic element effects by adding another inductance or capacitance. For example, an inductance due to the fringing field effect should be added to the original inductance value for accurate modeling.

For the investigation of the proposed coupled DSSR, the dimensions have been set to: D=3, G_1=G_2=0.2, L_1=6, L_2=7.96, P=0.7, and W=1.56 mm. These dimensions have been determined from parametric studies for a resonant frequency of 7.35 GHz. The studies also revealed that L_{DSSR} of the coupled DSSR is affected by the dimension (P) as well as the slot dimension ($D \times D$). Since current flows around two slotted regions ($D \times D$), a narrower P and larger D increases L_{DSSR}. Thus, the resonant frequency of the coupled DSSR can be varied using different values of P even though the slot dimension ($D \times D$) is the same. As previously found in Section 6.2, C_{DSSR} is 0.022 pF for the same microstrip gap dimensions (W=1.56 and G_1=0.2 mm). The shunt capacitance, C_P is calculated as 0.3 pF from (6.3) when $A=7.8\times10^{-6}$ m^2. Then, L_{Total} and C_S become unknown values. However, there is only a single value of C_S which will result in a particular bandwidth of the coupled DSSR. For this reason, L_{Total} and C_S can be determined by fitting the circuit simulated frequency response to the EM simulated data, where L_{Toal} dominantly affects a resonant frequency and C_S mainly controls a bandwidth. L_{Total} and C_S are then found to be 2.05 nH and 0.08 pF, respectively. Fig. 6-10 (c) presents the EM simulated S-parameters of Fig. 6-10 (a) and the circuit simulated results of Fig. 6-10 (b); their results agree well. It should be noted that the passband bandwidth of the equivalent circuit model in Fig. 6-10 (b) is controlled by C_S.

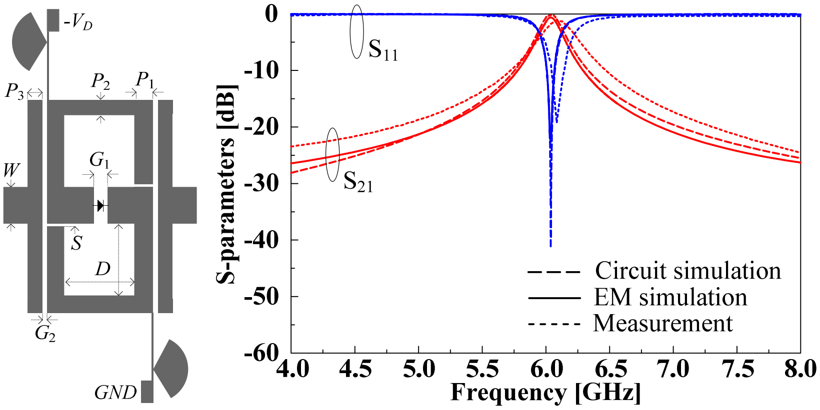

(a) (b)

Fig. 6-11. Proposed (a) tunable DSSR (D=4.5, G_1=0.6, G_2=0.2, P_1=P_2=0.7, P_3=0.6, W=1.56, and S=0.1 mm) and (b) S-parameter characteristics without varactor diode.

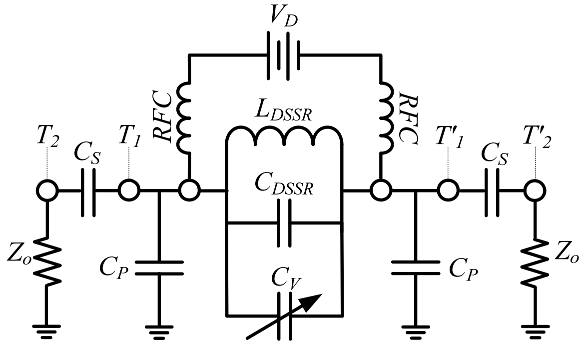

Fig. 6-12. Equivalent circuit model of the varactor tuned DSSR.

Fig. 6-11 (a) shows the microstrip circuit configuration of the proposed tunable DSSR. In Fig. 6-11 (a), DC is isolated from input and output RF ports by coupled gaps (G_2). Thus, additional lumped DC block capacitors are not necessary for this tunable resonator. Other gaps (S) are also added for an isolation of DC bias in Fig. 6-11 (a). By employing the gap (S), the series capacitance (C_S) due to the coupled gap dimension (G_2) is decreased. As a result, the resonant frequency is slightly shifted toward to the high frequency region. However, the accurate lumped element values for the tunable DSSR can still be determined since their element values are obtained from the simulated S-parameters. Without a varactor diode, the equivalent circuit model of the tunable DSSR is the same as the one in Fig. 6-10 (b). In order to demonstrate the proposed tunable DSSR and its equivalent circuit, the DSSR dimensions in Fig. 6-11 (a) are arbitrary selected as D=4.5, G_1=0.6, G_2=0.2, P_1=P_2=0.7, P_3=0.6, W=1.56, and S=0.1 mm. The corresponding lumped element values for the given tunable DSSR dimensions can be determined by using the same method described in the previous sections. The exact C_{DSSR} for G_1=0.6 and W=1.56 mm is found as 0.01 pF from a cross coupled microstrip line modeling. The parallel shunt capacitance (C_P) is calculated from (6.3), and then the series capacitance (C_S) is obtained by fitting the circuit simulated pass-band bandwidth to the EM simulated one. As already mentioned, the coupled DSSR's bandwidth is dominantly affected by C_S in Fig. 6-10 (b). Thus, C_S can simply be found. After that, L_{DSSR} is determined by matching the circuit simulated resonant pole location to the EM simulated one. The lumped element values for the given dimensions are C_{DSSR}=0.01 pF, L_{DSSR}=1.47 nH, C_P=0.8 pF, and C_S=0.13 pF. Fig. 6-11 (b) presents the circuit/EM simulated and measured S-parameters of the tunable DSSR without a varactor diode. As shown in Fig. 6-11 (b), the designed tunable DSSR resonates at 6.04 GHz, and its simulated and measured results show good agreement.

The lumped equivalent circuit of the tunable DSSR with a varactor diode is shown in Fig. 6-12. The variable capacitance (C_V) due to the different bias condition of the varactor diode changes the resonant frequency of the DSSR. Fig. 6-13 (a) and (b) present the simulated and measured S_{21} for the different bias levels of the varactor diode, where the tunable DSSR dimensions are equal to Fig. 6-11 (a). Thus, the lumped element values in Fig. 6-12 are also the same as C_{DSSR}=0.01 pF, L_{DSSR}=1.47 nH, C_P=0.8 pF, and C_S=0.13 pF. The varactor diode used for this experiment is MA46600 from M/A-COM. This diode typically provides 0.381 pF with no bias and 0.243 pF with 30 volts. From a diode modeling, the measured diode junction capacitances (C_V) have been found as 0.31, 0.295, 0.278, and 0.27 pF for 0, 5, 10, and 15 volts, respectively. The resonant frequency (f_0) of the DSSR in Fig. 6-10 (b) can be written as (6.6), where C_{Total} is the total capacitance of the coupled DSSR without the diode capacitance (C_V). Then, the resonant frequency (f_R) of the tunable DSSR's equivalent circuit in Fig. 6-12 can be estimated using (6.7), where f_0 can simply be found from EM simulation. The circuit simulated resonant locations in Fig. 6-13 (a) show good agreement with the measured results in Fig. 6-13 (b). Fig. 6-14 illustrates the photo of the fabricated tunable DSSR.

Quality (*Q*) factor of a microstrip circuit is a strong function of frequency and a substrate thickness [49]. Resonators can be characterized by their unloaded *Q* factor (Q_U), which is the ratio of the energy stored to the energy dissipated. Since Q factor is a figure of merit which represents the resonator's performance, it is an important parameter along with the resonator's slope parameter. From the measurement, loaded *Q* (Q_L) can be determined using (6.8). Once Q_L is found, Q_U can also be calculated from (6.9). Table 6-1 summarizes the performance of the fabricated tunable DSSR. One important fact in Table 6-1 is that the tunable DSSR's Q_U is a function of varactor diode bias voltage. As the bias voltage increases, Q_U also increases. This is caused by a diode junction resistance which is in parallel to the junction capacitance (C_V). The junction resistance is dramatically increased, i.e., open circuit, in the reverse bias condition, so C_V becomes dominant. This junction resistance value is decreased as the diode bias voltage increased. Thus, Q_U is increased with the diode bias voltage. The unloaded *Q* values in Table 6-1 are in the range of 100 to 200, which agrees with the theoretical calculation for a typical microstrip line [50].

$$f_0 = \frac{1}{2\pi\sqrt{L_{DSSR} \cdot C_{Total}}} \tag{6.6}$$

$$f_R = \frac{1}{2\pi\sqrt{L_{DSSR}\cdot\left(C_{Total}+C_V\right)}} = \frac{1}{\sqrt{\frac{1}{f_0^2}+4\pi^2\cdot L_{DSSR}\cdot C_V}} \tag{6.7}$$

$$Q_L = \frac{\omega_0}{\Delta\omega_{3dB}} \tag{6.8}$$

$$Q_U = \frac{Q_L}{1-10^{[IL(f_R)/20]}} \tag{6.9}$$

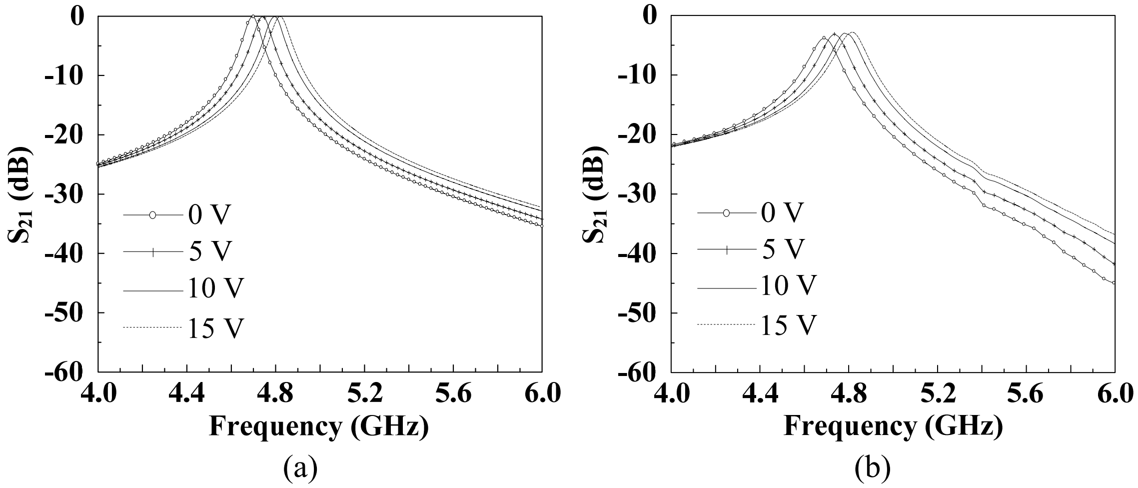

Fig. 6-13. Varactor tuned DSSR's (a) circuit simulated S_{21} ($C_{V,0V}$=0.31, $C_{V,5V}$=0.295, $C_{V,10V}$=0.278, and $C_{V,15V}$=0.27 pF) and (b) measured S_{21}.

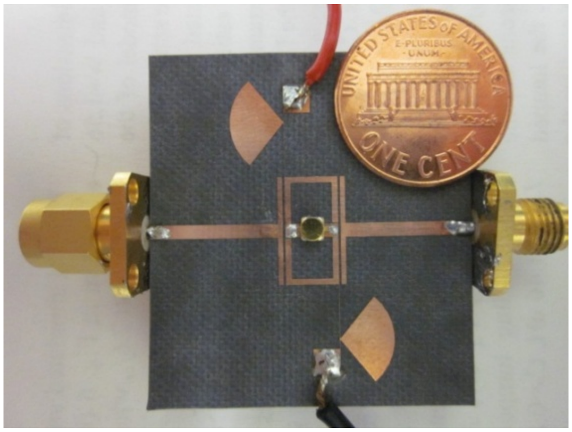

Fig. 6-14. Photo of the fabricated tunable DSSR.

TABLE 6-1
RESONANT FREQUENCIES, LOADED AND UNLOADED Q FACTORS OF THE MEASURED TUNABLE DSSR

Voltage (V)	f_R (GHz)	Q_L	Q_U
0	4.69	52.1	144.1
-5	4.74	52.6	170.7
-10	4.79	53.2	182.1
-15	4.82	53.5	188.5

6.5 BPF Design Using DSSR

Fig. 6-15 (a) shows the proposed microstrip miniaturized BPF using two coupled DSSRs. The center frequency of the filter is set to 7.35 GHz for downlink satellite communication systems. The designed filter dimensions are: D=3, L_1=4.4, L_2=7.96, G_1=G_2=0.2, and G_3=0.6 mm, and these dimensions are the same as the coupled DSSR dimensions in Fig. 6-10 (a). Fig. 6-15 (b) presents an equivalent circuit model of the proposed BPF. The capacitive coupling gap (G_3) is modeled as C_C in Fig. 6-15 (b). For the same DSSR dimensions, all other element values except C_C have already been determined in Fig. 6-10. Thus, C_C can be found by matching the circuit simulated S-parameters to the EM simulated data. This gives a C_C value of 0.012 pF.

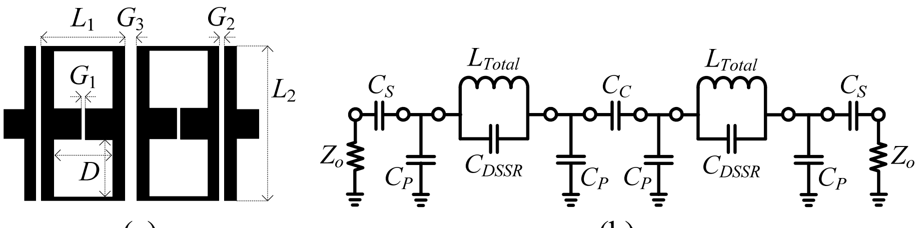

(a) (b)

Fig. 6-15. Proposed miniaturized BPF using two coupled DSSRs; (a) top view of proposed BPF (L_1=4.4, L_2=7.96, G_1=G_2=0.2, G_3=0.6, and D=3 mm), (b) lumped equivalent circuit model, and (c) comparison of fabricated DSSR BPF and conventional parallel coupled line BPF.

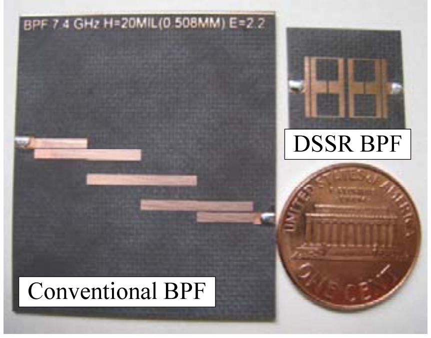

(c)

Fig. 6-15. Continued.

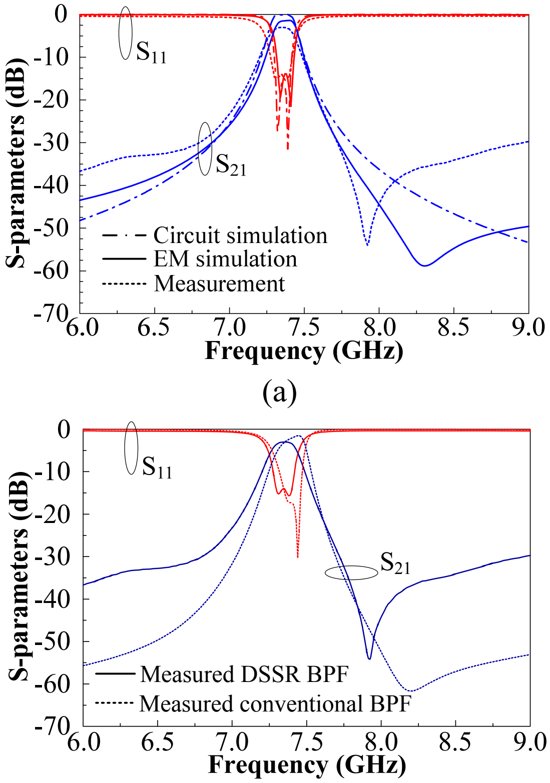

(a)

(b)

Fig. 6-16. Simulated and measured S-parameters; (a) simulated and measured results of DSSR BPF and (b) comparison of DSSR BPF and conventional BPF.

A photograph of the DSSR BPF and a conventional parallel coupled line BPF is shown in Fig. 6-15 (c). The conventional parallel coupled line BPF has been fabricated for a comparison. The number of stages for the parallel coupled line BPF is set to *N*=3 since it produces a similar cutoff slope. Fig. 6-16 (a) illustrates the simulated and measured results of the designed DSSR BPF, and Fig. 6-16 (b) compares the measured results of the DSSR BPF and the conventional parallel coupled line BPF. As presented in Fig. 6-15 (c) and Fig. 6-16 (b), a BPF miniaturization can be achieved using coupled DSSRs, and the frequency response characteristic of the DSSR BPF is comparable to a conventional parallel coupled line BPF with N=3.

6.6 Conclusions

A microstrip dumbbell-shaped slot resonator (DSSR) and its equivalent circuit models have been introduced in this chapter. Circuit and EM simulations validate lumped and distributed equivalent circuit models of the proposed DSSR. Using the DSSRs, miniaturized lowpass and bandpass filters are designed and tested. Since the DSSR is a simple microstrip structure, an analysis and design are relatively easy, and fabrication errors can also be reduced. In LPF and BPF designs using the DSSRs, both simulated and measured results agree well. The dimensions of the designed LPF are $0.27\lambda_g \times 0.17\lambda_g$ at a cutoff frequency of 3.4 GHz. A measured insertion loss of less than 1 dB and a return loss of greater than 18 dB have been achieved. The dimensions of the designed BPF are $0.37\lambda_g \times 0.27\lambda_g$ at a center frequency of 7.35 GHz. A measured insertion loss of less than 3 dB and a return loss of greater than 15 dB have been achieved. Using the proposed miniaturization technique, compact RF/microwave microstrip resonators and filters can be achieved.

CHAPTER VII

ISOSCELES TRIANGLE SHAPED PATCH RESONATOR

7.1 Introduction

The isosceles triangle shaped patch resonator (ITSPR) is investigated using electromagnetic (EM) simulation and a curve fitting method. New design equations which determine the ITSPR dimensions are then proposed. Other equations which estimate fractional bandwidth (FBW), effective dielectric constant, and center frequency of an ITSPR are also introduced. Simple design techniques for a low loss band-pass filter (BPF) and diplexer using ITSPRs are presented to demonstrate its practical uses in RF/microwave applications. The BPF designed by the proposed method produces much sharper frequency cutoff characteristics compared to a conventional BPF using a single ITSPR. The BPF using the ITSPR is easier to design and fabricate than BPFs using other coupling structures (such as a parallel/capacitive gap coupled line) since the frequency response of the ITSPR is less sensitive to the coupling gap. To validate the proposed analysis and design methodology, a 5.8 GHz BPF is designed and measured. The designed filter has a wide pass-band with a 2:1 VSWR bandwidth of 12% and an insertion loss of less than 1.5 dB in its pass-band. Measured results agree well with the simulated results. A diplexer with pass-bands of 5 and 6 GHz is also developed as an application of the ITSPR.

The microstrip band-pass filter (BPF) is one of the most widely used components in RF/microwave systems. Many filters [51]-[56] have been developed to meet today's filter requirements including low-insertion loss, compact size, and low cost. Simple geometrical structures for resonators and filters are preferable for easy analysis and design. In general, geometrically complex microstrip passive circuits tend to be more dependent on computer aided electromagnetic (EM) simulation. On the other hand, simple circuit structures provide a relatively easy analytical solution. As a result, their performance can be predicted in the design process, and the design methodology can be less dependent on EM simulation.

In this chapter, one of the simplest types of patch resonators, an isosceles triangle shaped patch resonator (ITSPR), is investigated. Utilizing an EM simulator, ITSPR design equations are obtained through curve fitting. The proposed equations provide good estimations of ITSPR performance and reduce time-consuming computer simulation in the design.

As the frequency spectrum becomes increasingly crowded, a sharp frequency cutoff is necessary for overall system performance and interference prevention. Generally speaking, filters require several resonator sections to achieve high frequency selectivity. In BPF design, inserting multiple resonator sections makes it difficult to reduce the circuit size and insertion loss. The conventional BPF design techniques discussed in [57] and [58] are not convenient since each microstrip resonator is separated by several gaps, and the filter's performance is significantly affected by fabrication errors of these gaps. This leads to inevitable errors in design realization which will alter the filter's characteristics. Thus, a simple design which minimizes the number of resonators (and therefore gaps) is preferable for low loss and compact filters, but the filter design should also produce a sharp frequency cutoff. To meet these requirements, a BPF using two ITSPRs is introduced as a proposed design.

Diplexers or multiplexers are indispensable components in wireless communication systems which operate in full duplex mode. Diplexers and multiplexers, shown in [59]-[62], are complicated and difficult to design and fabricate since there are many design parameters which should be considered for circuit dimensions. For these reasons, diplexer and multiplexer designs using a parallel coupled line filter or periodic-stub structure do not provide convenient design procedures. In this chapter, a diplexer which utilizes simple design techniques using ITSPRs is also presented.

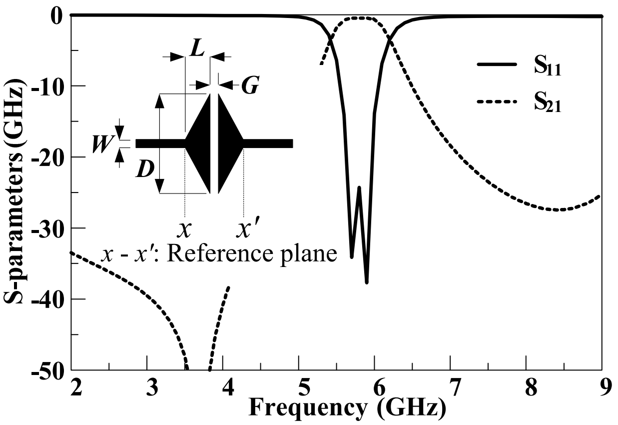

Fig. 7-1. Simulated S-parameters for an ITSPR with dimensions of W=0.56, L=3.2, D= 20.5, and G=0.6mm (H=0.635 mm and ε_r=10.2).

7.2 Background

The ITSPR was first introduced as the name of a DC-block cymbal resonator for a filter application as described in [63]. Fig. 7-1 presents an ITSPR's circuit configuration and simulated S-parameters. As shown in Fig. 7-1, an ITSPR produces a frequency pass-band like a BPF. One interesting characteristic in its frequency response is that an ITSPR operates as a dual mode resonator. By employing two resonant poles, an ITSPR is capable of a wider pass-band as compared to a single mode resonator.

The design variables for the ITSPR in Fig. 7-1 are: feed line width (*W*), patch length (*L*), gap (*G*), patch width (*D*), and substrate thickness (*H*). The feed line width (*W*) is always set to 50 Ω. The dimensions of these ITSPR design variables can be determined using the conventional design equations [63]:

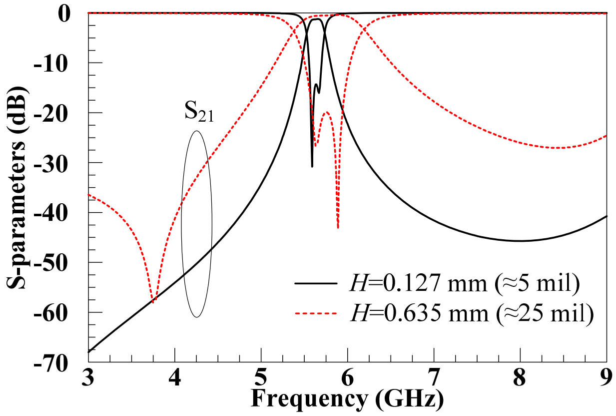

Fig. 7-2. Simulated S-parameters for an ITSPR with dimensions of D=20.5, L=3.2, and G=0.6 mm (ε_r=10.2).

$$f_o = 1.27 \cdot \frac{c}{D \cdot \sqrt{\varepsilon_r}} \tag{7.1}$$

$$L = \frac{D}{6.35} \tag{7.2}$$

$$G = \frac{L}{5} \ . \tag{7.3}$$

In (7.1), f_o is the pass-band center frequency and c is the speed of light. These conventional equations have been obtained from several simulations for different ITSPR dimensions.

In BPF design, operating bandwidth and pass-band center frequency are the most important design specifications. To obtain the desired performance, the filter should be designed based on these design specifications. Since the conventional design equations do not account for the substrate thickness effect, one cannot determine how the substrate thickness affects the bandwidth and center frequency shift. As illustrated in Fig. 7-2, use of the conventional equations (7.1)-(7.3) results in bandwidth and center frequency variations for different substrate thicknesses. Due to these frequency response variations, one cannot know what substrate thickness will result in the desired bandwidth and center frequency location. The conventional ITSPR design equations in (7.1)-(7.3) are only valid for a single substrate thickness which is used for the investigation. In Section III, new ITSPR design equations which can predict the exact center frequency and bandwidth are presented.

The conventional ITSPR design equation in (7.1), which determines the resonator's width (D), is a function of the dielectric constant (ε_r). In general, microstrip circuit design relies on the effective dielectric constant (ε_{eff}) to account for the fringing effects and radiated fields. Since this effective dielectric constant is a function of substrate thickness and microstrip line width, circuit design using the effective dielectric constant is more reasonable. For this reason, use of (7.1) might decrease the design accuracy. In order to obtain accurate ITSPR dimensions, the effective dielectric constant of the ITSPR should be determined. Calculation of the ITSPR's effective dielectric constant is discussed in Section 7.3.

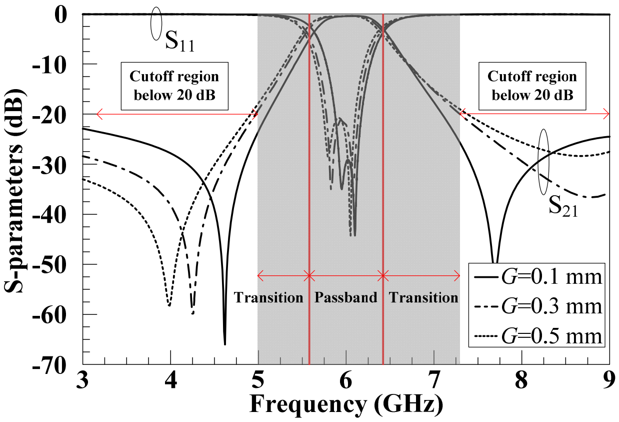

Fig. 7-3. Simulated S-parameters for an ITSPR with dimensions of D=20, L=3.1, H=0.635 mm, and ε_r=10.2.

7.3 Considerations of ITSPR Design Variables

The analytical solutions for the triangular patch resonator have been reported in [64], but these solutions are only valid for an equilateral triangle resonator and may not be compatible with an ITSPR. In this section, ITSPR dimensions (D, L, G, and H) as design variables are investigated to determine how these parameters affect operation and performance. Through this study, practical design equations for ITSPRs are introduced. The equations are validated through EM simulation and measurement.

Fig. 7-3 shows the simulated S-parameters of an ITSPR which is designed for a center frequency of 6 GHz using the conventional equations in (7.1)-(7.3). In a coupled type resonator or filter design, coupling gap distance (i.e., coupling coefficient) normally affects the frequency bandwidth. However, as illustrated in Fig. 7-3, the ITSPR's pass-band and center frequency do not show major changes even though the variations in gap dimension are significant. Due to the wide patch width (*D*), the coupling, i.e., series capacitance, between the two patches is strong. As a result, the coupling can be less dependent on the gap dimension (*G*). This illustrates that an ITSPR's pass-band and center frequency are not sensitive to the gap dimension. For this reason, the gap dimension (*G*) can be ignored in the ITSPR's design variables.

On the other hand, the frequency pass-band of a parallel/end coupled line BPF is very sensitive to its gap dimension. Thus, a BPF using an ITSPR can be easier to design and fabricate than BPFs which utilize other coupling structures.

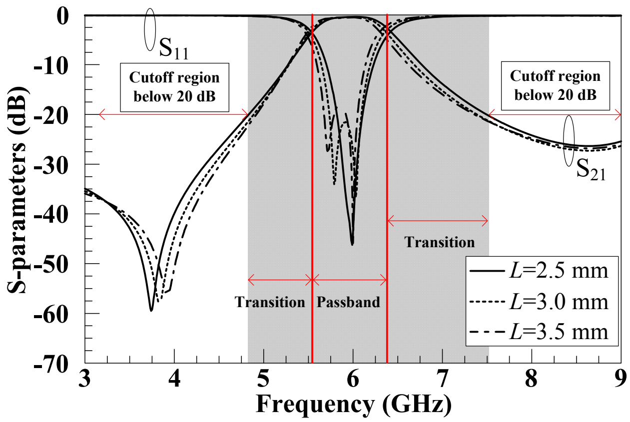

Fig. 7-4. Simulated S-parameters for an ITSPR with dimensions of *D*=20, *G*=0.6, *H*=0.635 mm, and ε_r=10.2.

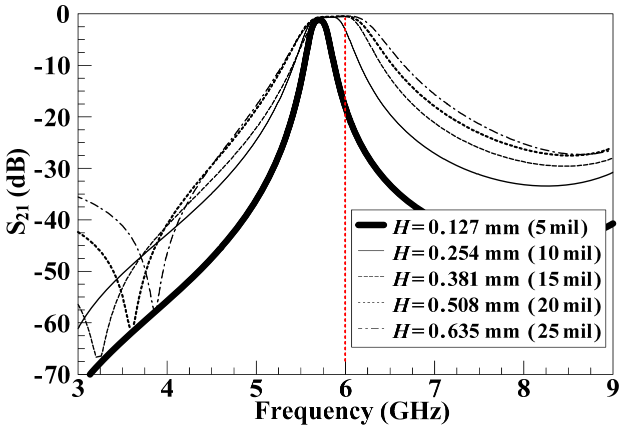

Fig. 7-5. Simulated S_{21} for an ITSPR with dimensions (D=20, L=3.1, G=0.6 mm, and ε_r=10.2) and varying substrate thickness.

In Fig. 7-3, transmission zeros are also observed. The transmission zeros below the pass-band and above the pass-band result from dominant magnetic coupling and electric coupling, respectively [65]. As the gap dimension (G) increases, the capacitance between the ITSPR and ground plane increases, and the capacitance between the two patches decreases. Accordingly, the magnetic coupling becomes dominant and the zeros appear below the pass-band. As the gap dimension narrows, the zero location moves closer to the pass-band. This improves the cutoff characteristic, but it is not significant as shown in the frequency responses of Fig. 7-3. Since the zero locations do not affect the pass-band and center frequency, which are the most important characteristics of a BPF, the formation of the zero locations is excluded from the study.

Fig. 7-4 illustrates the simulated S-parameters of an ITSPR which is designed for a center frequency of 6 GHz using the conventional design equations in (7.1)-(7.3). As shown in Fig. 7-4, the pass-band and center frequency are not appreciably altered when the resonator length (L) changes significantly. The electromagnetic field transition region, i.e., resonator length (*L*), reduces the reflections and focuses the field on the edge of the patch (*D*). Furthermore, an ITSPR's resonant frequency is mostly affected by the length of the patch edge (*D*). This explains why resonator length changes do not influence an ITSPR's overall frequency response characteristics. For this reason, the ITSPR length (*L*) can be disregarded from the ITSPR design variables.

Fig. 7-5 shows the simulated S_{21} of an ITSPR which is designed for a center frequency of 6 GHz using the conventional equations. As shown in Fig. 7-5, the bandwidth and center frequency are different for varying substrate thicknesses. When the substrate thickness increases, the bandwidth also increases. As a result, the center frequency is no longer fixed at 6 GHz. Thus, even if one designs an ITSPR using the conventional equations at a desired center frequency, the desired center frequency and bandwidth may not be obtained. This simulation experiment illustrates that the substrate thickness is a dominant factor for determining an ITSPR's operating frequency pass-band characteristics. For these reasons, the conventional equation in (7.1) is not a complete form. The ITSPR's substrate thickness (*H*) must be included as a design variable.

7.4 The Effective Dielectric Constant of an ITSPR

Through the investigation, it has been determined that the resonant point is generated when the ITSPR width (*D*) is approximately the same as the guided wavelength (λ_g). Thus, to develop accurate design equations, the ITSPR's effective dielectric constant (ε_{eff}) should be found.

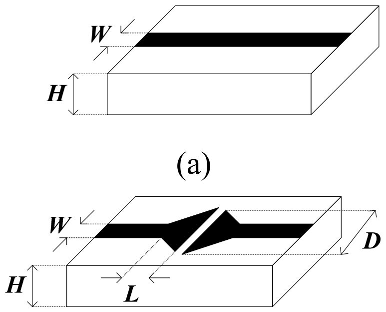

(a)

(b)

Fig. 7-6. Circuit configurations of (a) microstrip line and (b) ITSPR.

In Fig. 7-6 (a), the effective dielectric constant (ε_{eff}) of the microstrip line can be calculated using a closed-form equation obtained from curve fitting measured data [66]. Strictly speaking, ε_{eff} varies with frequency, but its variation is small. Thus, the closed-form equation can still be reliable. The microstrip line's closed-form equation for ε_{eff} is a function of line width (W) and substrate thickness (H).

To obtain a closed-form equation for ε_{eff} of an ITSPR, EM simulation and curve fitting are employed. This closed-form equation for ε_{eff} is used to develop new design equations for the ITSPR. For the simulation, the ITSPR dimensions are optimized to produce a 5.8 GHz center frequency on three different substrates. The three different substrates have dielectric constants of 6.15, 8, and 10.2, but the substrate thicknesses are the same at 0.127 mm (5 mil). The ITSPR dimensions and the dielectric constants for the simulations are:

Case 1: D=25.0, L=4.5, G=0.5, and ε_r=6.15.

Case 2: D=22.1, L=3.4, G=0.5, and ε_r=8.

Case 3: D=19.8, L=2.8, G=0.6, and ε_r=10.2.

These optimized ITSPR dimensions guarantee good resonance characteristics, i.e., an insertion loss of less than 0.8 dB and a return loss greater than 20 dB from an EM simulation. Fig. 7-7 shows ε_{eff} on a fixed substrate thickness of 0.127 mm. Since the variation of ε_{eff} in Fig. 7-7 is negligible, the frequency effect on ε_{eff} can be ignored. Fig. 7-8 represents the variation of ε_{eff} on different substrate thicknesses with the simulating frequency fixed at 5.8 GHz. As shown in Fig. 7-8, the substrate thickness (H) does not significantly change ε_{eff}. For these reasons, the frequency and substrate thickness can be disregarded in the closed-form equation for ε_{eff}.

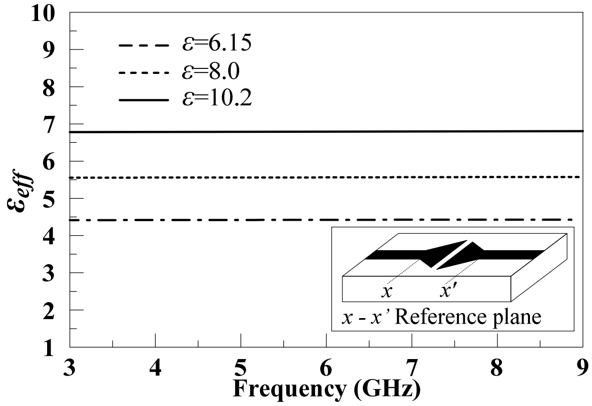

Fig. 7-7. EM simulated effective dielectric constant (ε_{eff}) for a fixed ITSPR substrate thickness (H=0.127 mm or 5 mil).

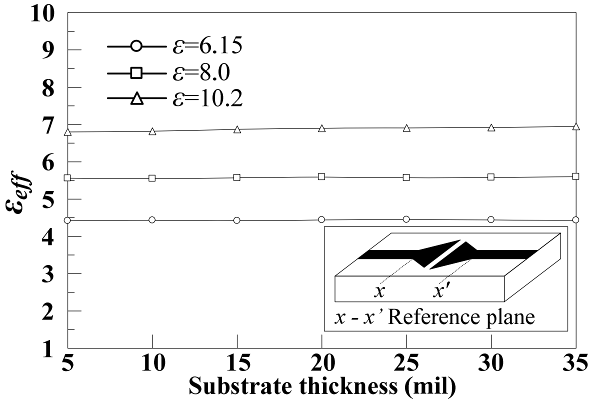

Fig. 7-8. EM simulated effective dielectric constant (ε_{eff}) at a fixed simulating frequency (f=5.8 GHz).

For $W/H > 1$, ε_{eff} of a microstrip line can be calculated using the conventional equation [66]

$$\varepsilon_{eff} = \frac{\varepsilon_r + 1}{2} + \frac{\varepsilon_r - 1}{2}\left(1 + \frac{12 \cdot H}{W}\right)^{(-1/2)} . \tag{7.4}$$

In this conventional closed-form equation, the W/H ratio is a critical factor in determining ε_{eff}, but the new proposed equation

$$\varepsilon_{eff} = \frac{\varepsilon_r + 1}{2} + \frac{\varepsilon_r - 1}{2}\left(1 + \frac{2 \cdot D}{L}\right)^{(-1/2)} \tag{7.5}$$

has different variables. From the simulated numerical data, it is found that ε_{eff} of an ITSPR is strongly affected by the D/L ratio. The proposed equation in (7.5) provides a good closed-form estimation for ε_{eff} of an ITSPR.

Table 7-1 validates the formula presented in (7.5) by comparing it to an EM simulation of ε_{eff}. The dimensions used for the comparison are optimized for a center frequency of 5.8 GHz and a substrate thickness of H=0.127mm (5 mil). As shown in Table 7-1, ε_{eff} determined using (7.5) matches well with the EM simulated results.

TABLE 7-1

EFFECTIVE DIELECTRIC CONSTANT (ε_{eff}) OF AN ITSPR

ITSPR Dimensions (mm)	ε_r	ε_{eff} (EM simulation)	ε_{eff} (Formula presented here)
D=25.0, L=4.5, G=0.5	6.15	4.4	4.3
D=22.1, L=3.4, G=0.5	8	5.6	5.4
D=19.8, L=2.8, G=0.6	10.2	6.9	6.8

7.5 Fractional Bandwidth of an ITSPR

The dimensions in Table 7-1 are used to investigate an ITSPR's bandwidth variation with differing substrate thicknesses. By fixing the dimensions and only varying the substrate thickness (*H*), an ITSPR's bandwidth variations due to *H* can be plotted using simulation results. Equations can be fit to the simulated plot and derived as

$$FBW(\%) = 2 \cdot \ln(H^2) - 2.3 \quad \text{for } \varepsilon_r{=}6.15 \tag{7.6}$$

$$FBW(\%) = 1.7 \cdot \ln(H^3) - 4 \quad \text{for } \varepsilon_r{=}8 \tag{7.7}$$

$$FBW(\%) = 2 \cdot \ln(H^3) - 5.5 \quad \text{for } \varepsilon_r{=}10.2 \tag{7.8}$$

where *H* is in mil.

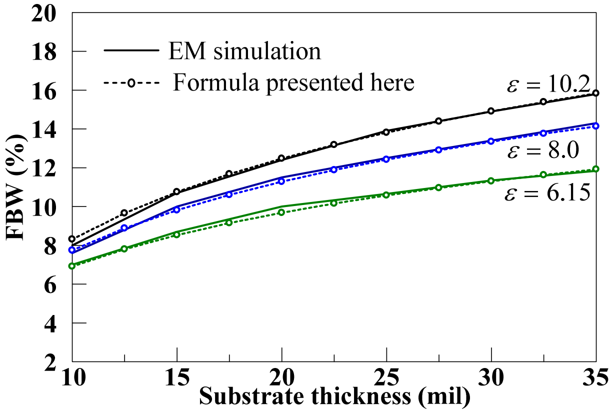

Fig. 7-9. Fractional bandwidth with varying substrate thickness (*H*).

The bandwidth estimating equations in (7.6)-(7.8) have been plotted and compared with the EM simulated results in Fig. 7-9. Fig. 7-9 illustrates increasing bandwidth of an ITSPR with increasing substrate thickness (*H*), where the ITSPR dimensions are fixed as in Table 7-1. The simulated data and equations proposed here show good agreement. From Fig. 7-9, one can estimate the fractional bandwidth and optimize the substrate thickness for ITSPR design.

7.6 ITSPR's New Design Equations

In order for an ITSPR to resonate at f_o, the patch width (D) should be set equal to the guided wavelength (λ_g) corresponding to f_o. This gives the design constraint

$$D = \lambda_g \tag{7.9}$$

which can be used to give

$$f_o = \frac{c}{\lambda_g \cdot \sqrt{\varepsilon_{eff}}} = \frac{c}{D \cdot \sqrt{\varepsilon_{eff}}} \tag{7.10}$$

where f_o is the center frequency of the pass-band and ε_{eff} is the effective dielectric constant of an ITSPR as given in (7.5). However, the investigation also reveals that the proposed equation in (7.10) is only accurate for a thin substrate (H=0.127 mm or 5 mil) because a thick substrate introduces spurious modes (i.e., surface wave modes) within the ITSPR. The spurious modes affect the center frequency location, so they are not desirable in the proposed design. As described earlier, increasing the substrate thickness enhances an ITSPR's bandwidth. Thus, for a thick substrate case, (7.10) may still be used, but the accuracy of the center frequency location is decreased due to the increased bandwidth with center frequency shift. This has already been illustrated in Fig. 7-5. Since (7.10) has been found most reliable on a substrate thickness of 0.127 mm (5 mil), (7.10) is defined as the prototype equation. To increase the accuracy of this prototype equation, the effects due to substrate thickness should be considered. Later, the prototype equation is modified in order to account for the substrate thickness effects.

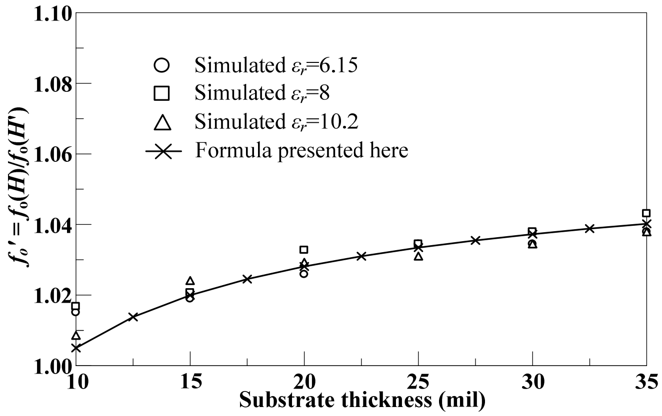

Fig. 7-10. Normalized center frequencies ($f_o' = f_o(H)/f_o(H')$) for varying substrate thickness (H=variable for substrate thickness and H'=5 mil).

Fig. 7-10 illustrates normalized center frequencies with varying substrate thickness. The ITSPR dimensions in Table I have been used for this analysis and only the substrate thickness is altered. The substrate thickness is varied from 0.254 mm (10 mil) to 0.889 mm (35 mil), and the center frequency is normalized by $f_o(H')$ which is the center frequency for a 5 mil substrate thickness. Here, $f_o(H)$ is obtained from EM simulation and $f_o(H')$ is calculated using the proposed formula in (7.10), where D and ε_{eff} are given in Table 7-1.

The substrate thickness factor (K) of the normalized center frequency due to the substrate thickness, as illustrated in Fig. 7-10, can be represented by a mathematical expression as

$$K = \left[\left\{\left(\frac{\ln\left(H/5\right)}{7 \cdot \ln\left(H\right)}\right) - 0.037\right\}\right] \cdot f_o \tag{7.11}$$

where H is in mils.

This substrate thickness factor (K) should be subtracted from (7.10) to obtain a consistent center frequency location for different substrate thickness. Then, a complete ITSPR design equation can be written as

$$D = \frac{c}{\left(f_o - K\right) \cdot \sqrt{\varepsilon_{eff}}} \ . \tag{7.12}$$

This equation accounts for the substrate thickness effect. As a result, the ITSPR can be designed on different substrate thicknesses without affecting the center frequency (f_o).

The normalized center frequency (f_o') in Fig. 7-10 is close to unity when H<0.254 mm (10 mil). Thus, when H <0.254 mm, the substrate thickness factor (K), in (7.12), becomes zero. Then, the ITSPR width (D) can be determined by

$$D = \frac{c}{f_o \cdot \sqrt{\varepsilon_{eff}}} \tag{7.13}$$

for $H < 0.254$ mm (10 mil).

For the thick substrate region (i.e., $H \geq 0.254$ mm), the ITSPR width (D) can be calculated by

$$D = \frac{c}{\left\{1.037 - \left(\frac{\ln\left(H/5\right)}{7 \cdot \ln\left(H\right)}\right)\right\} \cdot f_o \cdot \sqrt{\varepsilon_{eff}}} \tag{7.14}$$

where D is in mm.

Once the ITSPR width (D) is found from (7.13) or (7.14) at the desired center frequency, other ITSPR dimensions (L and G) can be found from

$$L = \frac{D}{a} \tag{7.15}$$

$$G = \frac{L}{b} \ . \tag{7.16}$$

The constants (*a* and *b*) are found from a simulation which gives a good insertion/return loss characteristic (i.e., $RL > 20$ dB and $IL < 1$ dB). The values for *a* and *b* change for different dielectric constants, and some values are shown in Table 7-2. These constants (*a* and *b*) can be found for other dielectric constants using the method shown here.

TABLE 7-2
OPTIMIZED VALUES FOR DIFFERENT DIELECTRIC CONSTANTS

ε_r	*A*	*b*
6.15	5.5	9.0
8	6.5	6.8
10.2	7.0	4.7

For further validation of the proposed equations in (7.6)-(7.8) and (7.13)-(7.16), ITSPRs with four different substrate thicknesses are designed for a center frequency of 6 GHz and fabricated. The dielectric constant is kept at 10.2 for all of the designs. The ITSPR dimensions of the four different substrate thicknesses are calculated using (7.13)-(7.16), simulated, and compared with measured results. The four different substrate thicknesses and calculated dimensions are:

Case 1: H=0.127 mm, D=19.17 mm, L=2.7 mm, G=0.6 mm
Case 2: H=0.254 mm, D=19.30 mm, L=2.8 mm, G=0.6 mm
Case 3: H=0.381 mm, D=19.50 mm, L=2.8 mm, G=0.6 mm
Case 4: H=0.635 mm, D=19.80 mm, L=2.8 mm, G=0.6 mm

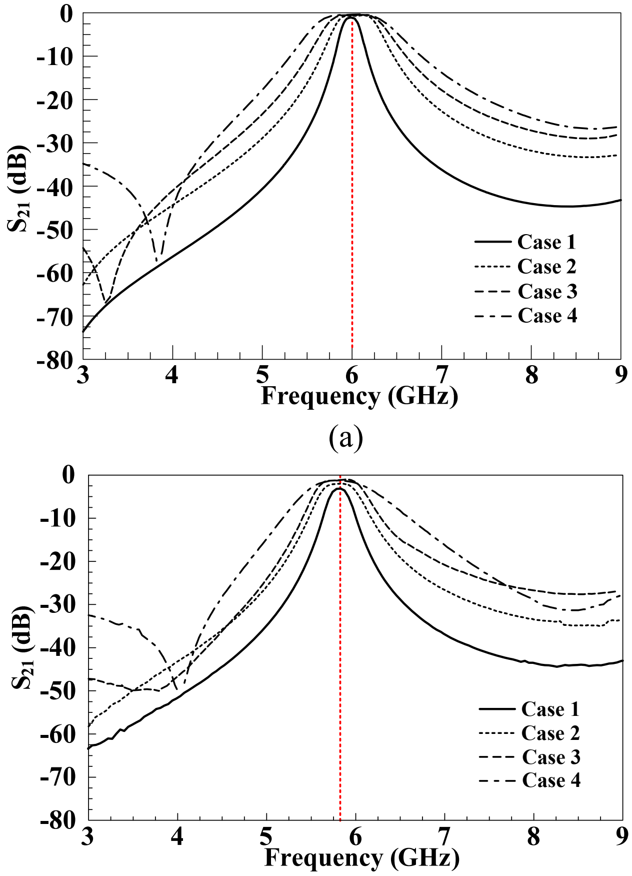

(a)

(b)

Fig. 7-11. S_{21} frequency response results of (a) EM simulation and (b) measurement for varying ITSPR substrate thickness (ε_r=10.2 for all cases).

The EM simulated and measured S_{21} results of the four different cases are shown in Fig. 7-11. These S_{21} frequency response characteristics can be compared with Fig. 7-5 since their center frequency is set to 6 GHz. The results in Fig. 7-11 are achieved using ITSPRs with dimensions calculated from the proposed equations in (7.13)-(7.16), and the results in Fig. 7-5 are obtained using dimensions calculated by the conventional equations in (7.1)-(7.3). The results using the proposed design equations show better center frequency agreement.

As shown in this section, an ITSPR's bandwidth and the center frequency can accurately be estimated by substrate thickness and dielectric constant. The proposed ITSPR design methodology would also hasten the design process by requiring less EM simulation time.

7.7 BPF Design Using Double ITSPRS

As previously mentioned, the gap dimensions of the parallel/end coupled line BPFs are very critical to their performance. Thus, a new filter design methodology reducing the number of gaps while maintaining the sharp frequency cutoff characteristic is required to improve overall filter performance.

The conventional BPF with a single ITSPR shown in [63] does not produce the sharp frequency cutoff characteristic as shown in Fig. 7-3 and 7-4. Due to its poor frequency cutoff characteristics, the BPF utilizing a single ITSPR could be considered as simply a dual mode resonator rather than a filter. Thus, this conventional BPF cannot be applied to a diplexer design when the two frequency channels of the diplexer are close each other. For these reasons, an alternative filter design technique using an ITSPR is necessary to produce a steep frequency cutoff characteristic.

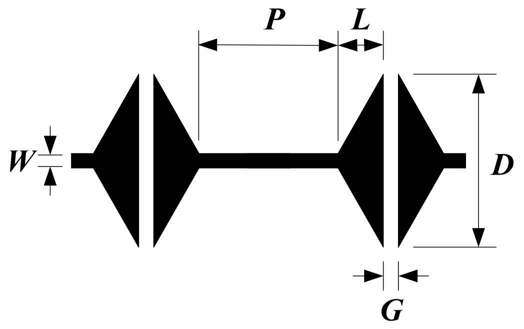

Fig. 7-12. Proposed BPF using two ITSPRs and one center transmission line.

In order to improve the frequency cutoff characteristics, a new BPF design using two ITSPRs is introduced. The improvement of the proposed design method is validated through simulation and measurement. The circuits are built on Rogers 3110 with a thickness of 0.635 mm and a dielectric constant of 10.2.

To demonstrate the double ITSPR design technique, a BPF with a center frequency of 5.8 GHz is designed. Fig. 7-12 shows the proposed double ITSPR BPF circuit configuration. As shown in Fig. 7-12, the BPF consists of two ITSPRs and one center transmission line. The line width (W) is set for a 50 Ω line, and the other ITSPR dimensions can be determined from the proposed equations in (7.13)-(7.16). The center transmission line length (P) is designed using

$$P = \frac{c}{4 \cdot \left(f_o - K \right)} \quad . \qquad (7.17)$$

The design equation in (17) can be derived from (10) and (12) when the transmission line length (P) is defined as a quarter-wavelength at the center frequency (f_o). Here, it should be noted that the ITSPR width (D) is not four times greater than the line length (P) since the width (D) includes the substrate thickness factor (K) for $H \geq 0.254$ mm.

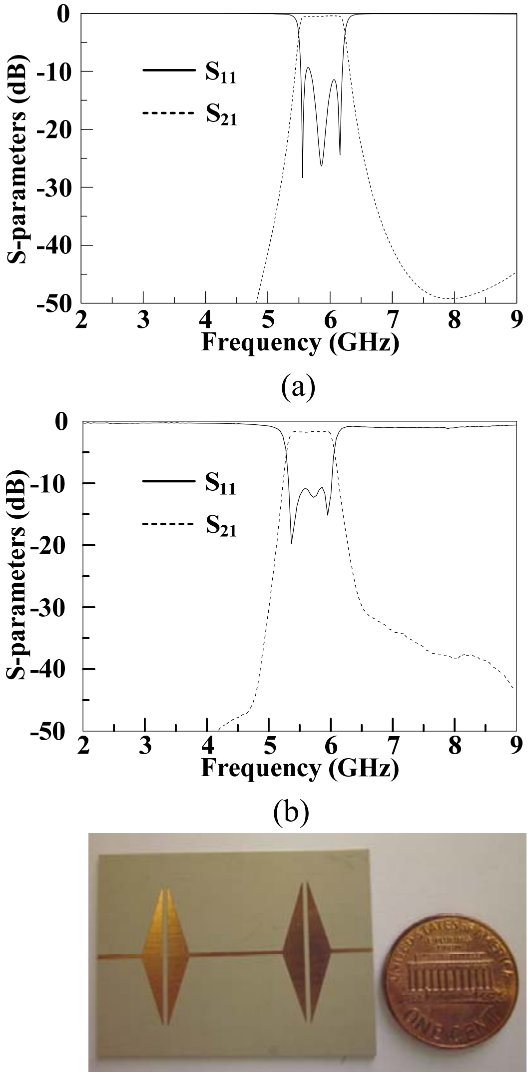

(a)

(b)

(c)

Fig. 7-13. S-parameter frequency responses of (a) simulated and (b) measured double ITSPR BPF (*D*=20.5 mm, *L*=2.9 mm, *G*=0.6 mm, and *P*=13.4 mm) and (c) photo of the fabricated ITSPR BPF.

The designed filter employing two equivalent ITSPRs with a center transmission line produces a much sharper frequency cutoff characteristic than a conventional ITSPR filter.

For parameters H=0.635 mm, f_o=5.8 GHz and ε_r=10.2, (7.14)-(7.16) can be used to find the ITSPR dimensions D, L, and G as 20.5, 2.9, and 0.6 mm, respectively. The center line length (P) is found to be 13.4 mm from (7.17). The EM simulated and measured results of a BPF with these dimensions are shown in Fig. 7-13 (a) and (b), respectively. A photograph of the fabricated BPF is also shown in Fig. 7-13 (c). As shown in Fig. 7-13 (a) and (b), the proposed BPF produces much sharper frequency cutoff characteristics as compared to the conventional one described in [63]. The measured data shows an insertion loss of less than 1.5 dB and a return loss of greater than 12 dB in the pass-band.

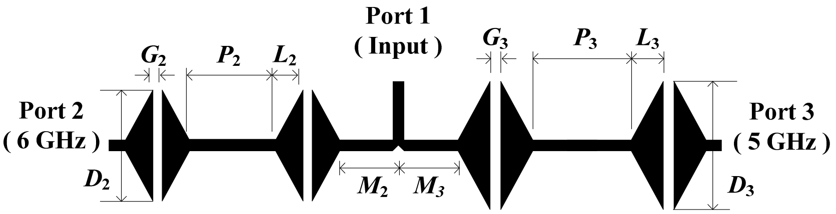

Fig. 7-14. Proposed diplexer utilizing four ITSPRs and its optimized dimensions (6 GHz: D_2=20 mm, L_2=3.1 mm, G_2=0.6 mm, P_2=12.5 mm, and M_2=4.3 mm and 5 GHz: D_3=23.85 mm, L_3=3.75 mm, G_3=0.75 mm, P_3=15 mm, and M_3=4.6 mm).

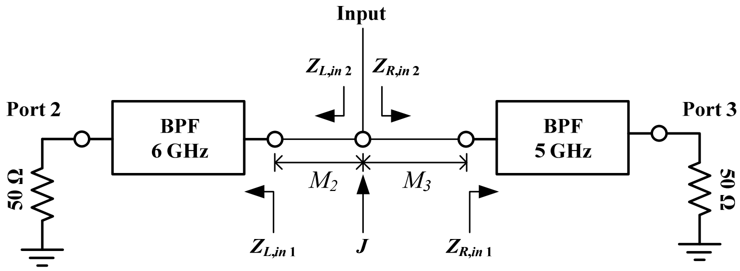

Fig. 7-15. Equivalent circuit configuration of the proposed diplexer; ports 2 and 3 are terminated with 50 Ω.

7.8 Diplexer Design

Based on the proposed BPF design utilizing two ITSPRs, a diplexer consisting of four ITSPRs is proposed. To demonstrate the proposed design, a diplexer with center frequencies of 5 and 6 GHz in each pass-band is designed, simulated, and measured. In this section, all circuits are fabricated on Rogers 3110 (thickness=0.635 mm and ε_r=10.2). Since the two channels are close to each other in the frequency band, the filters should be capable of producing a sharp frequency cutoff to reduce the interference between the two adjacent channels.

Fig. 7-14 shows the proposed diplexer with dimensions (D, L, G, P, and M). The dimensions for 5 and 6 GHz filters are found from the proposed equations in (7.13)-(7.17) and optimized using an EM simulator. The connecting line lengths (M_2 and M_3) can be defined by high and low input impedance conditions. In Fig. 7-15, $Z_{R,in1}$ and $Z_{L,in1}$ are the input impedances for the 5 and 6 GHz BPFs, respectively. Within the pass-band of these two filters, the input impedances $Z_{R,in1}$ and $Z_{L,in1}$ are about 50 Ω when both filters are terminated with 50 Ω.

To increase isolation between the two filters, a high and low input impedance condition is applied. If the input impedance, $Z_{R,in2}$ ($Z_{L,in2}$), at the junction point (J) is a high impedance (∞) and $Z_{L,in2}$ ($Z_{R,in2}$) is 50 Ω, all input signals flow into port 2 (port 3).

For the 5 GHz signal path from the input, $Z_{R,in2}$ should be 50 Ω near 5 GHz, i.e., the pass-band. If $Z_{L,in2}$ has a much higher impedance than $Z_{R,in2}$ ($Z_{L,in2} >> Z_{R,in2}$ (50 Ω)) at 5 GHz, all signals at 5 GHz will flow into the 5 GHz path. Since the input impedance of $Z_{L,in1}$ is low at 5 GHz, making M_2 a quarter- wavelength line ($\lambda_g/4$) at 5 GHz will make

$Z_{L,in2}$ a high impedance. Fig. 7-16 (a) shows a high input impedance for $Z_{L,in2}$ ($Z_{L,in2}$ = 662.7+j2670 Ω) at 5 GHz. Thus, all signals at 5 GHz flow into the 5 GHz BPF since $Z_{R,in2}$ is 50 Ω as shown in the shaded area of Fig. 7-16 (b).

For the 6 GHz signal path from the input, $Z_{L,in2}$ should be 50 Ω near 6 GHz. If $Z_{R,in2}$ has a much higher impedance than $Z_{L,in2}$ ($Z_{R,in2} >> Z_{L,in2}$(50 Ω)) at 6 GHz, all signals at 6 GHz will flow into the 6 GHz path, which is port 2. Since the input impedance of $Z_{R,in1}$ is low at 6 GHz, making M_3 a quarter-wavelength line ($\lambda_g/4$) at 6 GHz will make $Z_{R,in2}$ a high impedance. Fig. 7-16 (b) shows a high input impedance for $Z_{R,in2}$ ($Z_{R,in2}$ = 5275 + j7789 Ω) at 6 GHz. Thus, all signals at 6 GHz flow into the 6 GHz BPF since $Z_{L,in2}$ is 50 Ω as shown in the shaded area of Fig. 7-16 (a).

The design procedure to determine the dimensions of M_2 and M_3 are summarized as:

1) The input impedances $Z_{R,in1}$ (at 6 GHz) and $Z_{L,in1}$ (at 5 GHz) are found from the electromagnetic (EM) simulation. Their impedances should be low. If their impedances are high, one may use a half-wavelength line for M_2 and M_3.

2) The dimensions of M_2 and M_3 are approximated as quarter wavelengths at 5 GHz and 6 GHz, respectively.

3) The dimension of M_2 (M_3) is optimized to give a high input impedance for $Z_{L,in2}$ ($Z_{R,in2}$) at 5 GHz (6 GHz).

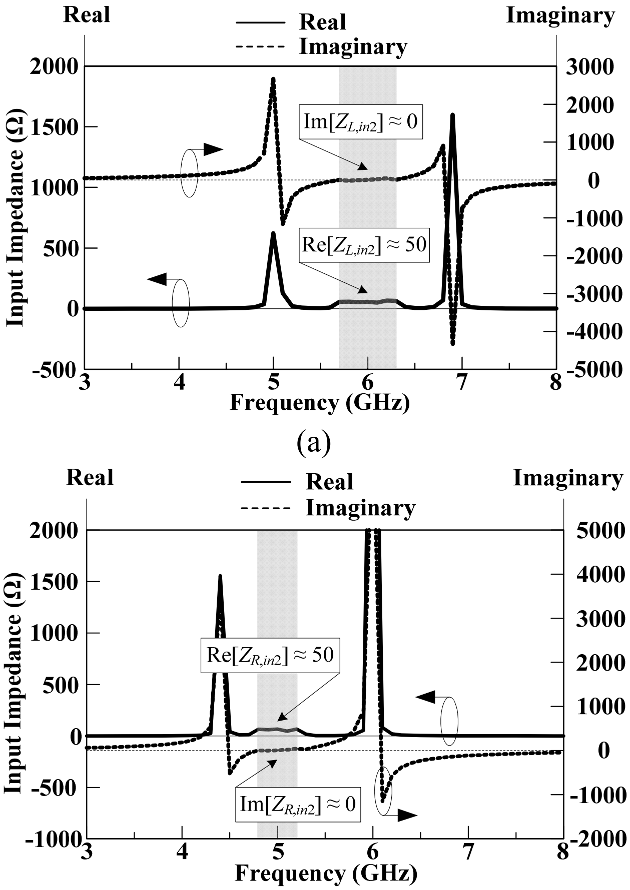

(a)

(b)

Fig. 7-16. Simulated input impedances (a) $Z_{L,in2}$ and (b) $Z_{R,in2}$ at the junction, *J*.

From the above procedure, M_2 and M_3 are found to be 4.3 mm and 4.6 mm, respectively. Fig. 7-17 (a) and (b) show the simulated and measured S-parameters of the designed diplexer. A comparison of these two results is also presented in Fig. 7-17 (c). Both simulated and measured results successfully validate the design methodology, and they agree fairly well. The isolation between the two output ports has been plotted in Fig. 7-18 and is greater than 30 dB within the two frequency pass-bands. A photograph of the fabricated diplexer is shown in Fig. 7-19. The proposed diplexer in this paper shows better performance and less circuit complexity as compared with previous work [59].

Since the designed diplexer has a simple structure, it is easy to fabricate and minimizes cost.

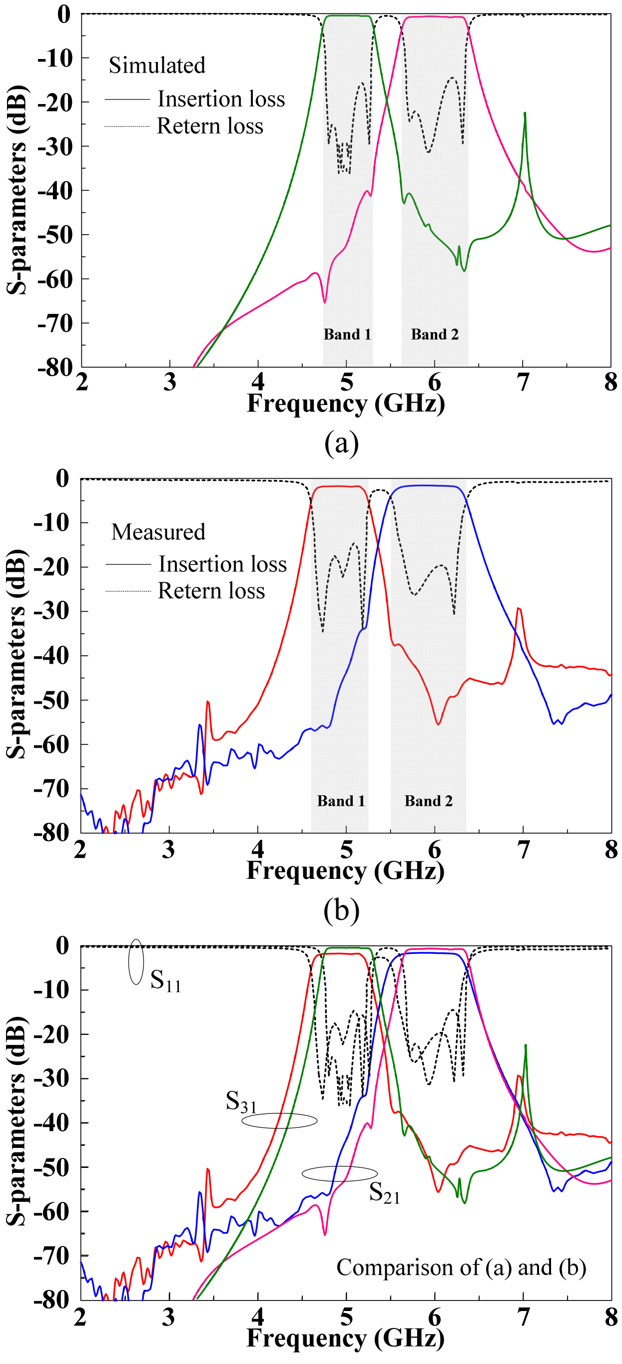

(a)

(b)

(c)

Fig. 7-17. S-parameters of (a) EM simulated and (b) measured diplexer and (c) comparison of both results.

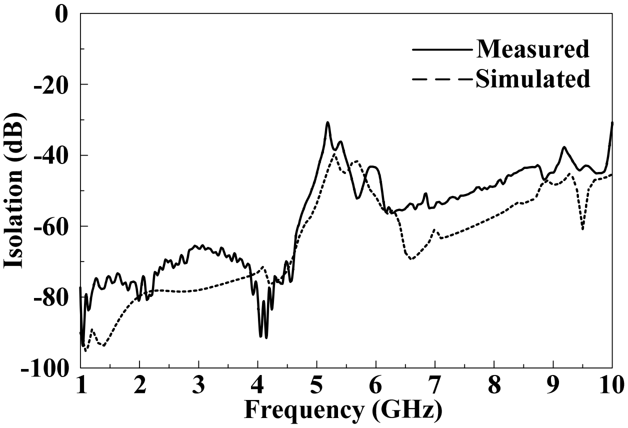

Fig. 7-18. EM simulated and measured isolation of the diplexer.

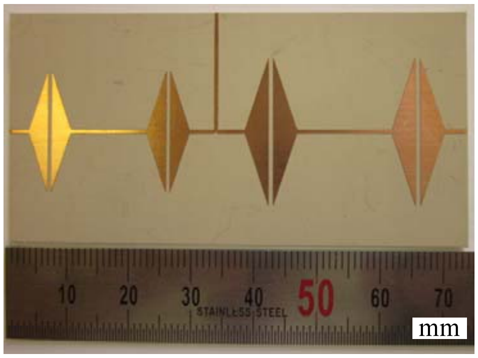

Fig. 7-19. Fabricated diplexer using ITSPRs.

7.9 Conclusions

A rigorous investigation to determine an ITSPR's effective dielectric constant, design equations, and bandwidth has been conducted. The proposed equations are validated through several simulations and measurements. Based on these studies, simple techniques for BPF and diplexer designs using ITSPRs have been presented. The BPF using the proposed method has the advantages of wide bandwidth, low loss, and simple fabrication. Compared to a conventional BPF using a single ITSPR, the proposed filter utilizing two ITSPRs and one center microstrip line produces steeper frequency cutoff characteristics. The insertion loss and return loss of the proposed BPF are measured as less than 1.5 dB and greater than 12 dB, respectively. A diplexer design using high and low impedance conditions has also been introduced as an application of the ITSPR. The simulated and measured results show fairly good agreement in both BPF and diplexer designs.

CHAPTER VIII

PHASED ARRAY FOR MULTIFUNCTION RADAR APPLICATIONS

8.1 Introduction

The study of phased arrays is very extensive and would need several texts to cover adequately. In this section, however, a brief description of relevant backgrounds and design parameter will be given for introductory purposes.

An antenna is a component that radiates and receives the electromagnetic energies and used for almost all wireless communication applications. An antenna is a reciprocal device, and the same antenna can serve as a receiving or transmitting device. Antennas considered as a component which provide transitions between guided and free-space electromagnetic waves. Guided waves are confined to the boundaries of a transmission line to transport signals from one point to another, while free-space electromagnetic waves radiate unbounded [67]. A transmission line is designed for a minimized radiation loss, but the antenna is designed to have maximum radiation. The radiation generally occurs due to discontinuities (which cause the perturbation of fields or currents), unbalanced currents, and so on.

Single antennas are popularly utilized for many communication applications because of a large HPBW and, consequently, a lower gain. However, for some applications including long range communication applications and radar systems, a high-gain and narrow pencil beam is required. Since most antennas have dimensions that are on the order of one wavelength, and since beamwidth is inversely proportional to antenna size, more than one antenna is required to sharpen the radiation beam. Generally, by increasing the number of antenna elements, one can increase a directivity of the antenna. An array of antennas working simultaneously can focus the reception or transmission of electromagnetic energy in a particular direction, which increase the useful range of a system.

Considering the one-dimensional linear array shown in Fig. 8-1, the radiated field from a set of sources can be given by:

$$\begin{aligned} E_{total} = I_1 f_1(\theta,\phi)\rho_1 \frac{e^{-j(k_0 r_1 - \Phi_1)}}{4\pi r_1} + I_2 f_2(\theta,\phi)\rho_2 \frac{e^{-j(k_0 r_2 - \Phi_2)}}{4\pi r_2} + \cdots \\ + I_i f_i(\theta,\phi)\rho_i \frac{e^{-j(k_0 r_i - \Phi_i)}}{4\pi r_i} + \cdots \end{aligned} \tag{8.1}$$

where I_i, ρ_i, and Φ_i are the ith element's magnitude, polarization, and phase, respectively; $f_i(\theta, \phi)$ is the radiation pattern of the ith element and r_i is the distance from the ith element to an arbitrary point in space; and k_0 is the propagation constant, equal to $2\pi/\lambda_0$.

Typically, the polarization of every element is aligned for copolarization, i.e., $\rho_i \approx \rho = 1$. The array has N elements with uniform spacing d. It is oriented along the z axis with a phase progression Φ. In far field condition, letting $r_1=r$ leads to the phase terms of:

$$\begin{aligned} r_1 &\cong r \\ r_2 &\cong r + d\cos\theta \\ r_3 &\cong r + 2d\cos\theta \\ &\vdots \\ r_n &= r + (N-1)d\cos\theta \end{aligned} \tag{8.2}$$

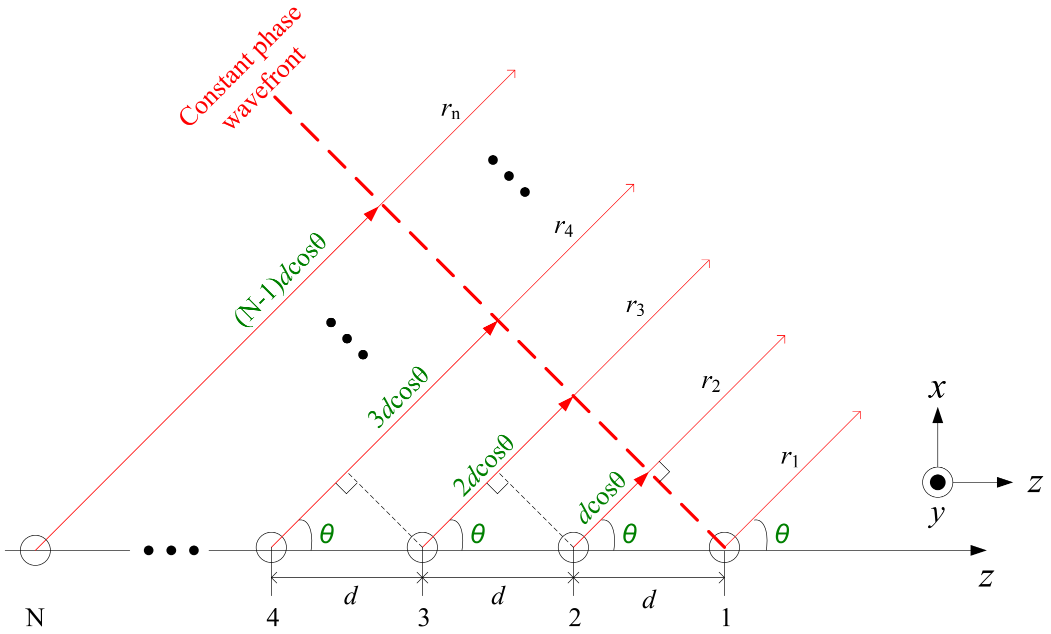

Fig. 8-1. *N*-element array along $\underline{z}$ axis.

For uniform amplitude (I_i=I), if radiation patterns of all elements are identical ($f_i(\theta,\phi)$=$f(\theta,\phi)$) and the phase progression to antenna elements are the same (Φ_i=Φ), the approximation in (8.2) allows the total field to be given by:

$$E_{total} = f\left(\theta,\phi\right) I \frac{e^{-jk_0 r}}{4\pi r} \sum_{i=1}^{N} e^{-j(i-1)(k_0 d\cos\theta-\Phi)} \tag{8.3}$$

element pattern × array factor

The total field from the array described by the equation in (8.3) is made up of an element pattern $f(\theta,\phi)I(e^{-jk_0 r}/4\pi r)$ and the array factor (AF). This is known as pattern multification. The AF in (8.3) can be rewritten as:

$$AF = \sum_{i=1}^{N-1} e^{-jn\psi} \tag{8.4}$$

where $\psi = k_0 d \cos\theta - \Phi$. The expression in (8.4) is the AF of a uniform linear array. Φ is a progressive phase difference of adjacent two elements. (8.4) implies that AF, i.e., main beam, can be controlled by adjusting element spaces (*d*) and progressive phase difference (*Φ*) between elements. From simple mathematical steps, (8.4) can be shown as:

$$AF\Big|_n = \frac{1}{N}\left[\frac{\sin\left(\frac{N}{2}\psi\right)}{\sin\left(\frac{1}{2}\psi\right)}\right] \tag{8.5}$$

where $\psi = k_0 d \cos\theta - \Phi$. (8.5) is a normalized AF of a uniform linear array.

For a scanning array with elements laying on z-axis as shown in Fig. 8-1, it is desired that the maximum radiation of the array is oriented at an angle θ_0, where θ_0 is ranging from 0° to 180°. For the maximum radiation between 0° and 180°, the normalized AF in (8.5) should also be a maximum. When ψ=0 in (8.5), the maximum AF is obtained. This leads to:

$$\psi = k_0 d \cos\theta - \Phi = 0 \tag{8.6}$$

$$\Phi = k_0 d \cos\theta\Big|_{\theta=\theta_0} \tag{8.7}$$

As a result, AF in (8.4) can be presented as:

$$AF = \sum_{i=1}^{N-1} e^{-jn(k_0 d(\cos\theta - \cos\theta_0))} \tag{8.8}$$

The expression in (8.8) is useful for computing the AF using commercial mathematic plotting tools.

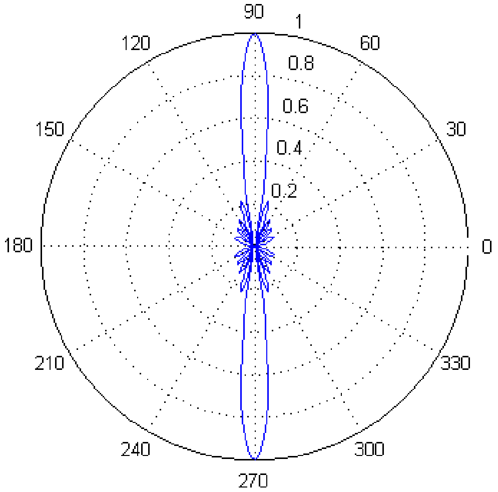

Fig. 8-2. Broadside of a uniform linear array with θ_0=90°, d=0.5λ, and N=10.

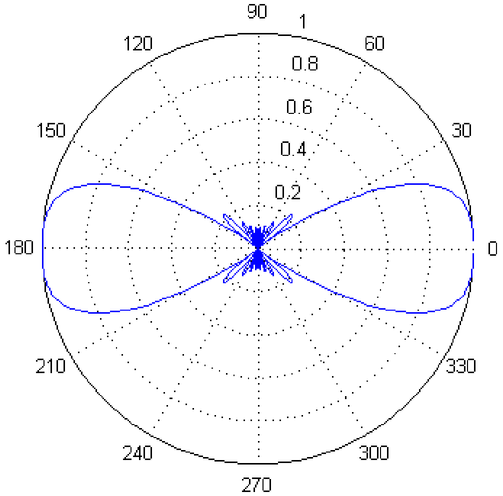

Fig. 8-3. Endfire of a uniform linear array with θ_0=0°, d=0.5λ, and N=10.

Figs. 8-2 and 8-3 show normalized AFs of a uniform linear array using (8.8). When elements lies on z-axis in Fig. 8-1, substituting θ_0=90° and d=0.5λ into (8.8) produces a broadside array factor pattern in Fig. 8-2. When θ_0=0° (or θ_0=180°) and d=0.5λ, (8.8) results in an endfire array factor pattern as shown in Fig. 8-3.

As explained in broadside and endfire array, main beam directions can be controlled by the phase excitation between the elements and the distance between the elements. The progressive phase difference between the elements is the key parameter for a scanning array operation. For the scanning array, it is desired that a main beam angle (θ_0) be $0° < \theta_0 < 180°$ for broadside scanning. Fig. 8-4 illustrates an N-element linear array with progressively larger phase delay from left to right. The AF can be formulated without consideration of the type of elements. For simplicity, it is assumed that array elements are isotropic radiator and a magnitude of element current, I_i=1. The AF of Fig. 8-4 can be written as:

$$AF = 1 + e^{-j(k_0 d\cos\theta - \Phi)} + e^{-j2(k_0 d\cos\theta - \Phi)} + \cdots + e^{-j(N-1)(k_0 d\cos\theta - \Phi)} \qquad (8.9)$$

Then, (8.9) can be simplified as (8.4), where $\psi = k_0 d\cos\theta - \Phi$.

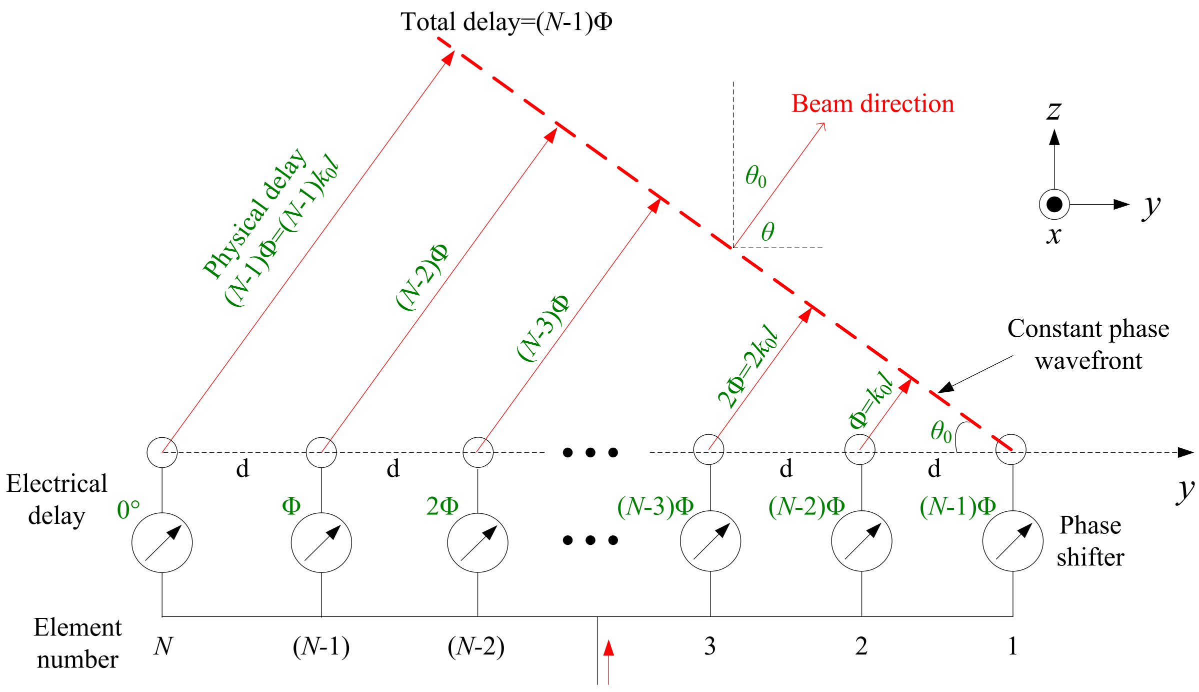

Fig. 8-4. *N*-element array with progressively larger phase delay from left to right.

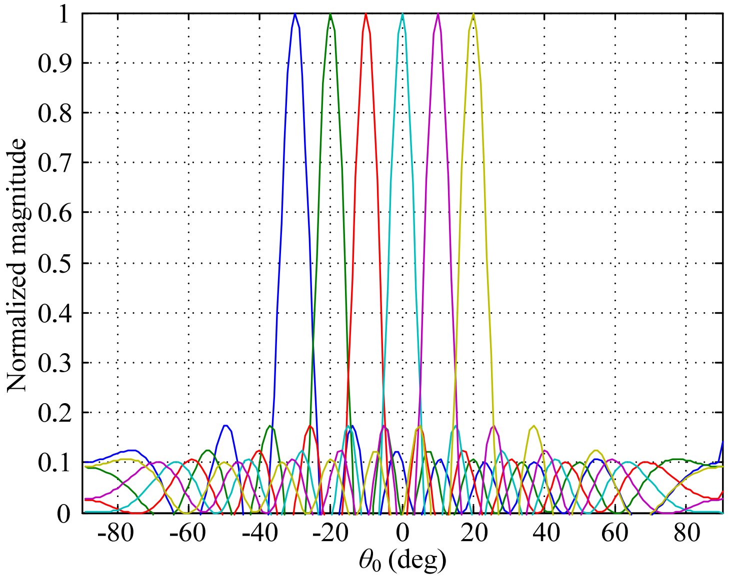

(a)

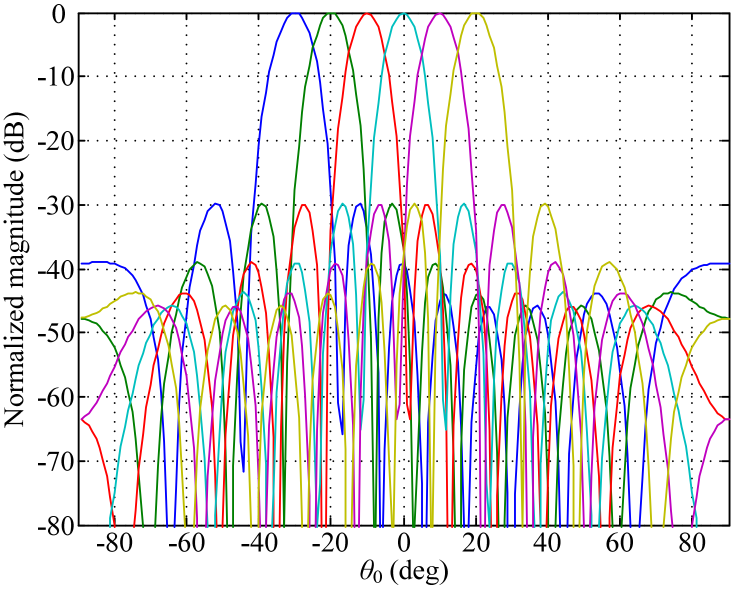

(b)

Fig. 8-5. Normalized AF of scanning array; (a) absolute value and (b) dB scale, where θ_0=-30, -20, -10, 0, 10, and 20°.

The parameter Φ is the progressive phase shift across the array, which means that there is a phase difference of Φ between the currents on adjacent elements. The progressive phase shift causes the radiation emitted from the array to have a constant phase front that is pointing at the angle θ_0 (where θ_0=90°-θ) as shown in Fig. 8-4. By varying the progressive phase shift across the array, the constant phase front is changed.

The scanning operation of Fig. 8-4 can be explained using (8.4). The equation in (8.4) is a maximum when the exponential term equals 1. Because $\psi = k_0 d \cos\theta - \Phi$, this maximum happens when $\psi = 0$ or:

$$\Phi = k_0 d \sin(\theta_0) = k_0 d \sin(90^\circ - \theta) = k_0 d \cos(\theta) \tag{8.10}$$

Then, (8.10) can be rewritten as:

$$\theta_0 = \text{scanning angle=}\sin^{-1}\left(\frac{\Phi}{k_0 d}\right) \tag{8.11}$$

where d= distance between two neighboring antennas (m), k_0=propagation constant in free space (rad/m), and Φ=progressive phase shift.

Thus, a scanning angle (θ_0 or main beam angel) can be estimated from (8.11) and progressive phase difference (Φ) of elements. This is the basic concept used in a phased array. Using (8.4) and (8.11), AF pattern of the scanning array in Fig. 8-4 can be plotted. Figs. 8-5 (a) and (b) show a normalized AF and its dB scale pattern, respectively.

Alternatively, (8.11) can also be derived from Fig. 8-4. For each element, at the constant phase wavefront, the total phase delay should be the same for all elements. The total phase delay equals the summation of the electrical phase delay due to the phase shifter and the physical phase delay. From any two neighboring elements, elements 1 and 2 for example, one can have:

$$l = d \sin\theta_0 \tag{8.12}$$

Therefore,

$$\Phi = k_0 l = k_0 d \sin\theta_0 \tag{8.13}$$

The expression in (8.13) is the same as (8.10).

From an array antenna, the main beamwidth and gain can be estimated from the number of array elements. If the elements spaced by half-wavelengths to avoid the generation of grating lobes (multiple beams), the number of radiating elements N for a pencil beam is related to the half-power (or 3 dB) beamwidth by [68]:

$$\theta_{\text{3dB BW}} \approx \frac{100}{\sqrt{N}} \tag{8.14}$$

where $\theta_{\text{3dB BW}}$ is the half-power beamwidth in degrees. A gain of the corresponding antenna array is:

$$G \approx \eta \pi N \tag{8.15}$$

where η is the aperture efficiency.

In a phased array, the phase of each antenna element is electronically controllable. One can change the phase of each element to make the array electronically steerable. The main beam will point to the direction that is normal to the constant phase front. This front can be adjusted electronically from individual phase shifter of each element.

The AF is a periodic function. Thus, it is possible to employ a constant phase front in several directions, called grating lobes. This can happen when the argument in the exponential in (8.4) is equal to a multiple of 2π. To scan to a given angle, θ_0, as in Fig. 8-4, Φ must be chosen to satisfy $\Phi = k_0 d \sin(\theta_0)$ as before. Thus, $\psi = -2\pi = k_0 d(\cos\theta -$

sinθ_0). For the given scan direction, a grating lobe will begin to appear in the end-fire direction (θ=180°) when the argument becomes:

$$-k_0 d(1+\sin\theta_0) = -2\pi. \tag{8.16}$$

From dividing out 2π from (8.16), the expression in (8.16) can be rewritten as:

$$d = \frac{\lambda_0}{1+\sin\theta_0} \tag{8.17}$$

Grating lobes reduce the array's performance to focus the radiated power in a specific area of angular space (directivity) and are undesirable in the array pattern. The spacing between adjacent elements should be less than the distance defined in (8.17) to avoid grating lobes.

In a two dimension array, (8.9) can be modified for 2D scanning operation:

$$AF = \sum_{m=0}^{M-1} e^{-jm(k_0 d_x \cos\theta\cos\phi - \Phi_x)} \sum_{n=0}^{N-1} e^{-jn(k_0 d_y \cos\theta\sin\phi - \Phi_y)} \tag{8.18}$$

where d_x and d_y are defined as the pace between the elements in the x and y directions. Φ_x and Φ_y are the progressive phase shifts in the x and y directions.

8.2 X-Band Phased Array Using Piezoelectric Transducer (PET) Phase Shifter

In this section, phased array using piezoelectric transducer (PET) phase shifter is introduced. Low cost phased array using the PET phase shifter has been introduced in [69]-[72]. Fig. 8-6 depicts a multiline differential and progressive phase shifter controlled by the PET. A dielectric perturber attached to the PET can move op and down by a DC bias voltage varied from 0 to 90 V. The dielectric perturbation changes the distributed capacitance of the microstrip line, which is controlled by the PET movement and the applied voltage. The capacitance variations correspond to variations in effective dielectric constant, which change the propagation constant, thus the phase shift [69]. Since the phase shift is proportional to the length of a perturbed line, a triangular shaped perturber shown in Fig. 8-6 can achieve the required progressive differential phase shift of Φ, 2Φ, and 3Φ between the lines. The expression in (8.11) illustrates that the progressive phase shift determines the scanning angel for a fixed frequency and element distance.

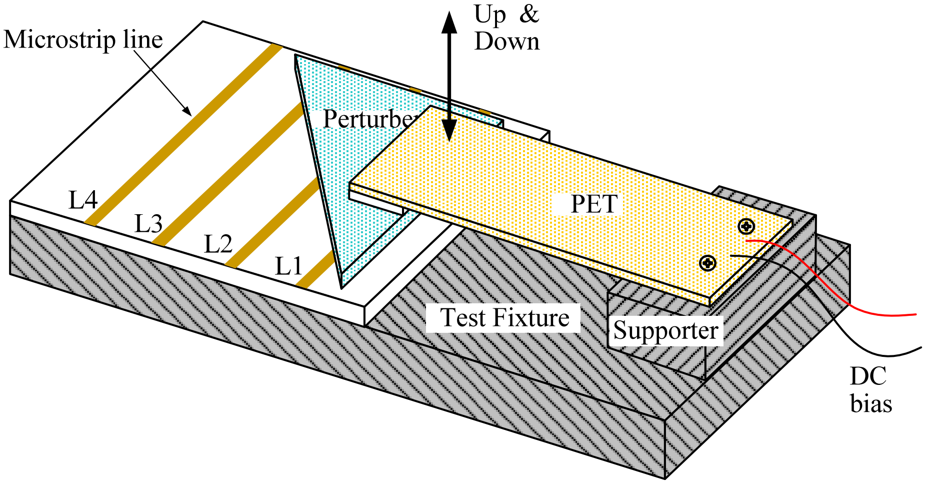

Fig. 8-6. PET controlled phase shifter [69].

The fixed free type cantilever beam PET, produced by Piezo Systems Inc., Cambridge, MA, provides mechanical movement for the attached perturber in the vertical direction as illustrated in Fig. 8-6. The PET actuator accommodates the dimensions of 57.2 x 31.8 x 2.2 mm^3, which ultimately affects PET response time. The PET used in this experiment has a response time of approximately 5 ms. The PET shows a vertical movement of ±1.2 mm when applying a DC bias of ±60 V.

The progressive phase shift between any two neighboring microstrip lines can be calculated as:

$$\Delta\phi = \Delta L \cdot \frac{2\pi}{\lambda_0}\left(\sqrt{\varepsilon_{eff}^{'}(f) - \varepsilon_{eff}(f)}\right) \tag{8.19}$$

where ΔL is the progressive length of the perturber above the microstrip lines, and $\varepsilon'_{eff}(f)$ and $\varepsilon_{eff}(f)$ are the effective relative permittivities of the perturbed and unperturbed microstrip lines, respectively [73]. From [73], it has been found that the phase shift can be maximized by having: 1) higher permittivity of microstrip line substrate and perturber; 2) thicker perturber; 3) narrower microstrip line width; 4) thinner microstrip substrate. Additionally, a higher permittivity of the perturber than that of the microstrip substrate should significantly increase the phase shift. However, in this case, it is possible to degrade the phase shifter performance by becoming very lossy at a high-frequency range due to the leaky-wave-mode generation [73]. In order to maximize the phase variation, the permittivity of the microstrip line substrate has been set to 2.2 with a thickness of 0.508 mm. The permittivity of the perturber set to 10.2 with a thickness of 1.27 mm. The arrays are fed by a 4-way power divider using a binomial multi-section matching transformer. For X-band operation, N=2 are utilized for the power divider design. Fig. 8-7 shows a 2-way power divider using binomial matching transformer (N=2), where Z_1=42.3 Ω, Z_2=30.2 Ω, and $l_1=l_2=\lambda_g/4$ at f_c. The center frequency f_c is set to 10 GHz. Fig. 8-8 presents the photograph of the fabricated PET controlled phase shifter and 4-way power divider for X-band operation. Figs. 8-9 and 8-10 illustrates the measured S-parameters of the fabricated PET controlled phase shifter at 0 and 60 V, respectively. As shown in the Figs. 8-9 and 8-10, insertion and return loss characteristics are similar in two different bias conditions. However, as mentioned before, the leaky-wave-mode degrades the phase shifter's loss characteristics above 14 GHz.

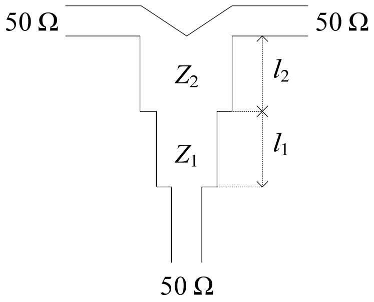

Fig. 8-7. Power divider using binomial matching transformer (N=2).

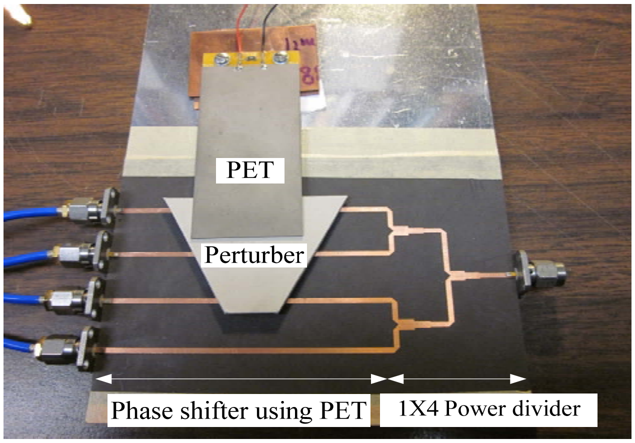

Fig. 8-8. Fabricated PET controlled phase shifter and 4-way power divider.

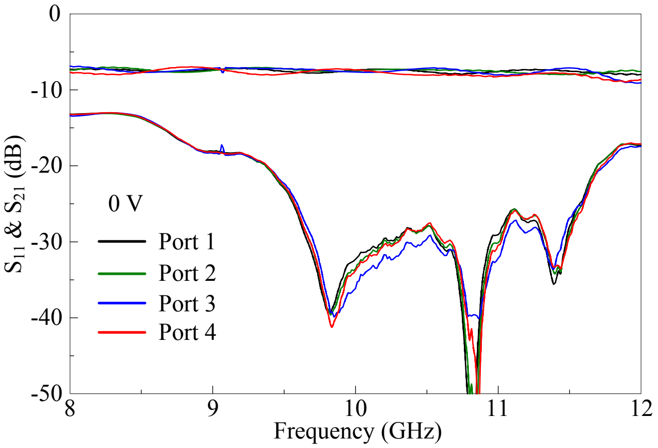

Fig. 8-9. Measured S-parameters of PET controlled phase shifter (0 V) in Fig. 8-8.

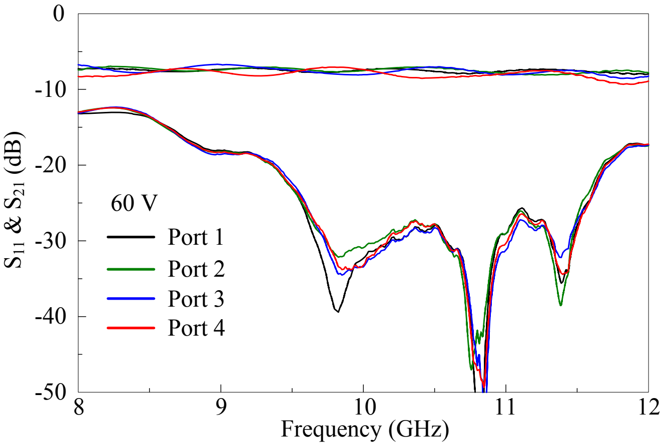

Fig. 8-10. Measured S-parameters of PET controlled phase shifter (60 V) in Fig. 8-8.

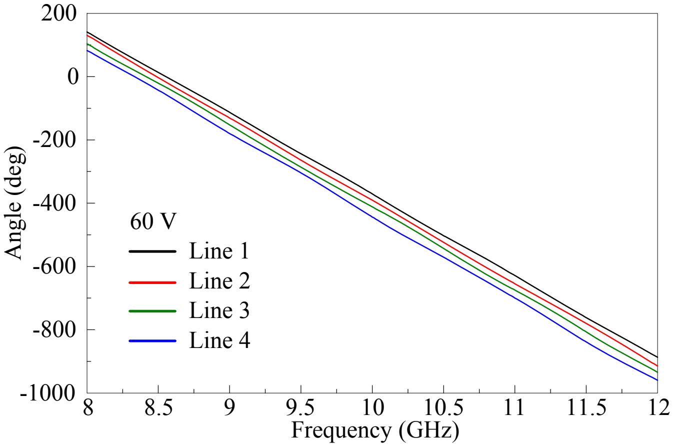

Fig. 8-11. Measured phase of PET controlled phase shifter (60 V) in Fig. 8-8.

From the expression in (8.11), the progressive phase shift of Φ=30 ° and *d*=10 mm result in the array's scanning angle of 16 °, 14.4 °, and 13.13 ° at 9, 10, and 11 GHz, respectively. Fig. 8-11 presents the measured phase of PET controlled phase shifter, where the progressive phase differences are approximately found to be 27 ° from 8 to 12 GHz. Stripline fed Vivaldi antenna shown in [70] is utilized for an H-plane 1x4 array. The detail antenna dimensions can be found in [70]. Fig. 8-12 illustrates the H-plane 1x4 Vivaldi antenna array, where the each antennas are separated by 10 mm, i.e., *d*=10 mm. Fig. 8-13 shows the measured radiation patterns of the H-plane 1x4 Vivaldi antenna array in Fig. 8-12. The measured array gain is about 8 dBi from 8 to 12 GHz. Fig. 8-14 shows the photograph of the measurement setup in anechoic antenna chamber at Texas A&M University. Figs. 8-15 (a) and (b) presents the measured radiation patterns of the H-plane 1x4 PET controlled phased array operating at X-band. The phased array produces the main beam scanning angle about 10 °~14 ° over the bandwidth.

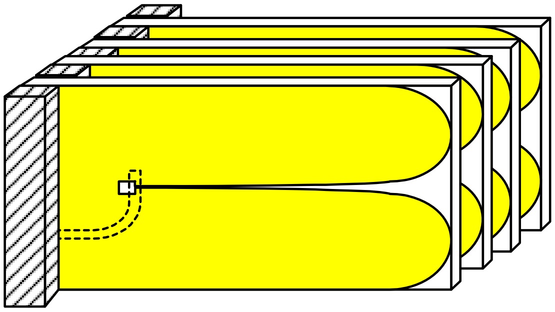

Fig. 8-12. H-plane 1x4 Vivaldi antenna array [69].

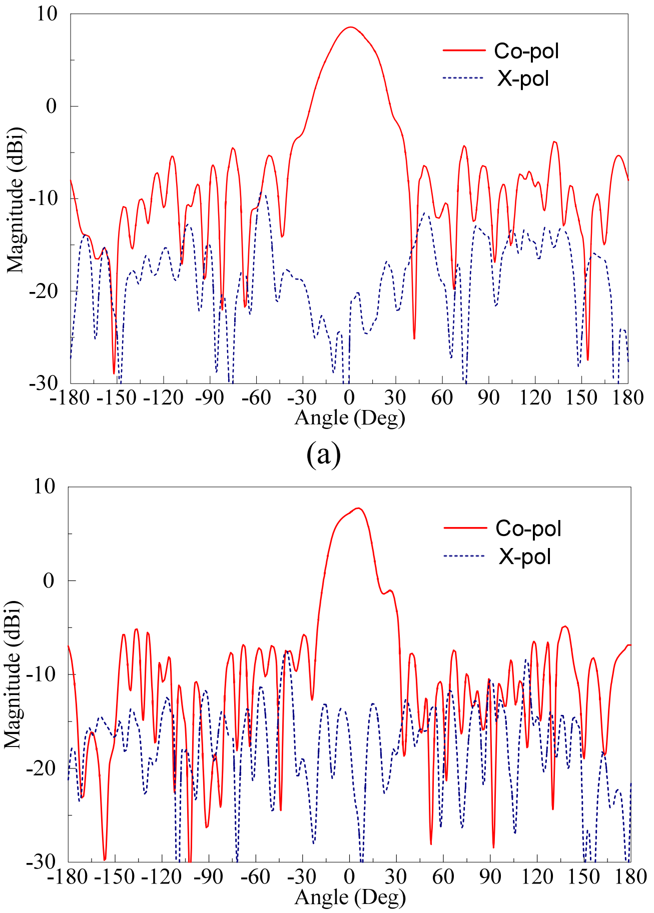

(a)

(b)

Fig. 8-13. Measured radiation patterns of 1x4 Vivaldi antenna array at (a) 9 GHz and (b) 12 GHz.

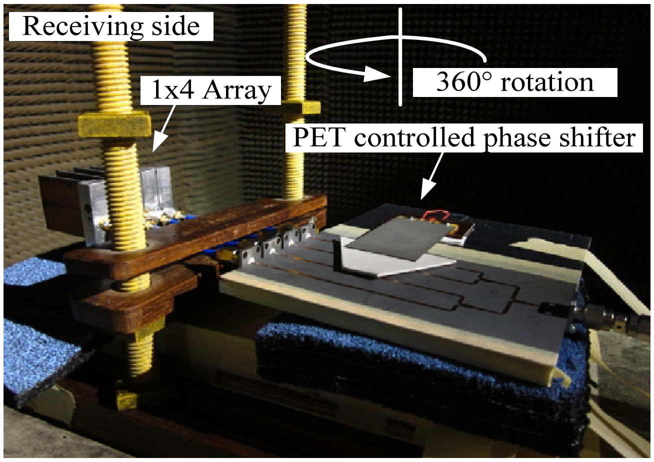

Fig. 8-14. Photograph of H-plane 1x4 PET conrolled phased array in anechoic antenna chamber.

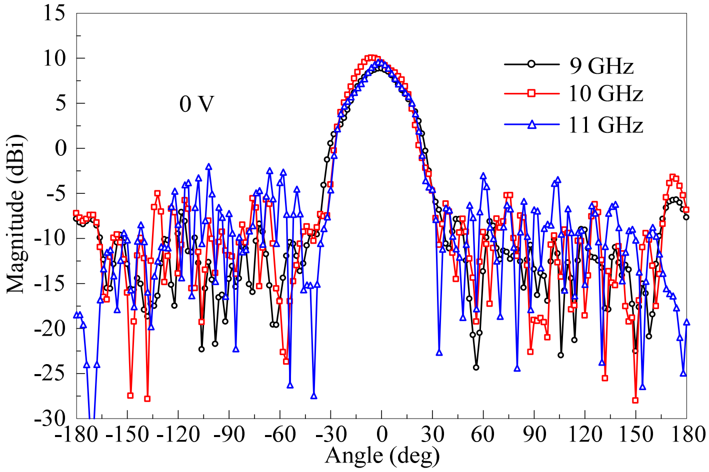

(a)

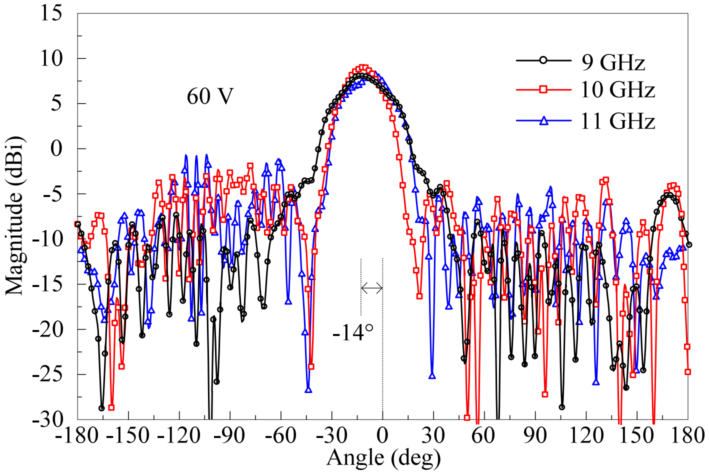

(b)

Fig. 8-15. Measured radiation patterns of H-plane 1x4 PET phased array; (a) 0 V and (b) 60 V.

8.3 X-Band Phased Array Using MMIC Phase Shifter

In this section, a phased array operating from 8 to 12 GHz is introduced for low cost multifunctional radar systems. Fig. 8-16 illustrates a typical system diagram of a transceiver front-end module. In Fig. 8-16, the system consists of single pole double throw (SPDT) T/R switches, power amplifiers (PAs), low noise amplifiers (LNAs), power divider, phase shifters and antennas. The array antenna, phase shifters, and power divider are shared in both transmitting and receiving paths. The T/R switches, PAs, and LNAs are normally integrated in a single chip using complementary metal oxide semiconductor (CMOS) technologies. In the demonstration for a low cost phased array design, the array antennas and power divider are fabricated using a microstrip. The MMIC 4-bit phase shifter (HMC543LC4B) produced by Hittite Microwave Corp. is utilized for progressive phase shift of the array antenna. The phase shifter covers from 0 to 360 ° with the steps of 22.5 °. The fabricated phased array front-end system including the array antennas, phase shifters, and power divider are measured in anechoic antenna chamber.

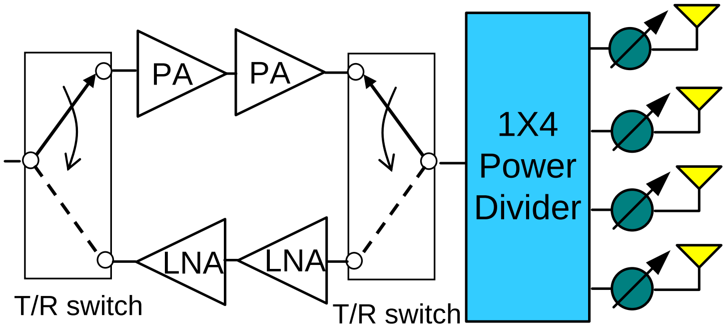

Fig. 8-16. Block diagram for phased array with full duplex operation.

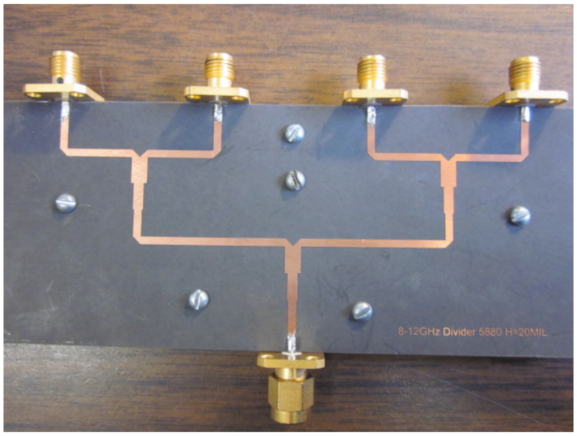

Fig. 8-17. Fabricated 1x4 power divider.

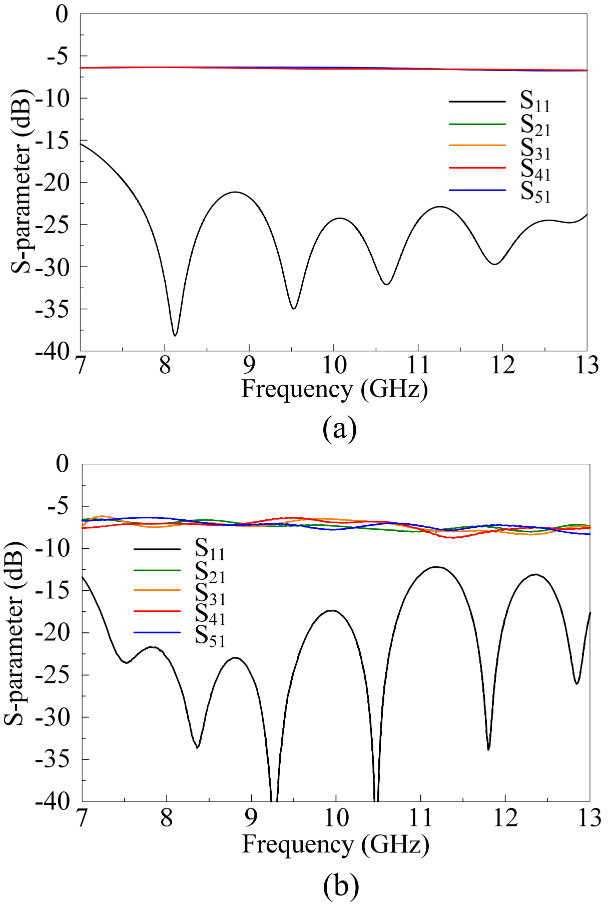

Fig. 8-18. S-parameters from (a) EM simulations and (b) measurements.

Fig. 8-17 shows a photograph of the fabricated 1x4 power divider using binomial multisection matching technique. The power divider utilizes two quarter wavelength matching transformers, and operates for X-band. Figs. 8-18 (a) and (b) illustrate EM simulated and measured S-parameters of the designed power divider. As shown in the Fig. 8-18 (a), the EM simulated insertion losses of all ports are found to be 6.5 dB. The return loss is greater than 20 dB in all frequency bandwidth. The measured results in the Fig. 8-18 (b) also present reasonable agreement to the EM simulated results.

Fig. 8-19. Phase shifter measurement using network analyzer.

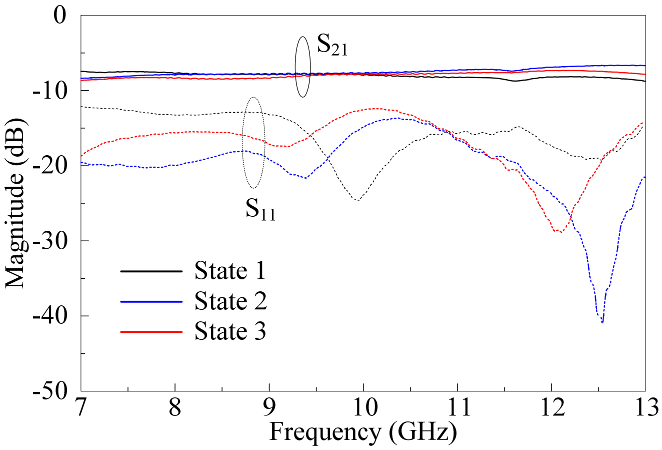

Fig. 8-20. Measured S-parameters of the phase shifter for on-state.

Fig. 8-19 shows a photograph of the phase shifter, where the output phase of the phase shifter is controlled by input voltages (0 or -3 V). The two control input voltages of 4 bit phase shifter provide 16 different inputs, and this ultimately produces 16 different output phase of the phase shifter. The maximum input power of the phase shifter is 27 dBm. Fig. 8-20 presents the measured insertion and return losses of the phase shifter. The return loss is greater than 10 dB, and the insertion loss is found to be 7 ~ 8 dB from 8 to 12 GHz.

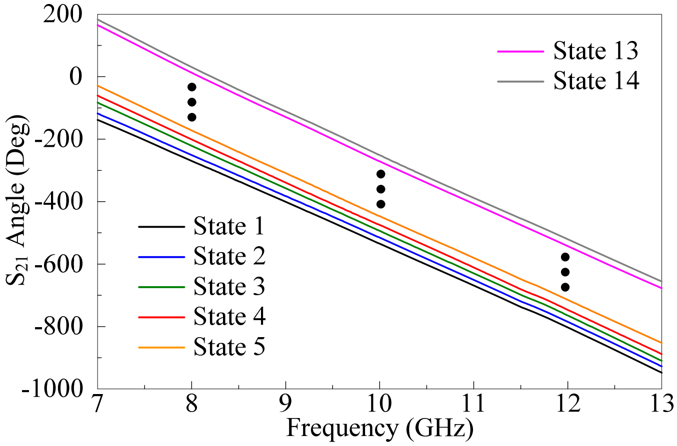

Fig. 8-21. Measured S_{21} phase of the phase shifter for on-state.

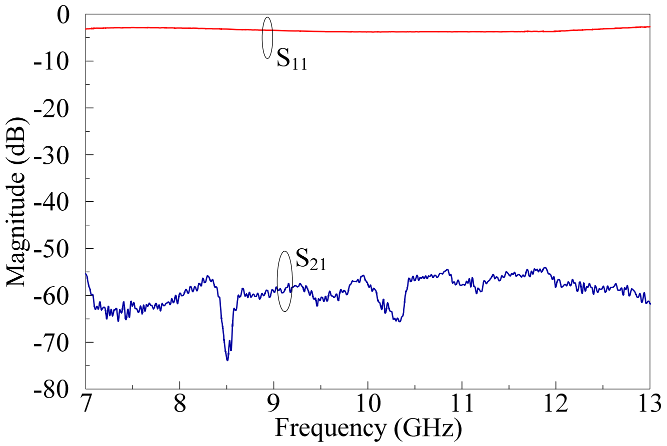

Fig. 8-22. Measured S-parameters of the phase shifter for off-state.

Fig. 8-21 presents the measured output phase of the phase shifter, and it shows almost uniform phase difference for each state from 8 to 12 GHz. Measured S-parameters of the phase shifter for off-state is illustrated in Fig. 8-22. For the off-state, the signal cannot pass the phase shifter. This characteristic of the off-state is useful for phase measurement of each phase shifter, where the phase shifters are connected to the array antenna. The same antenna elements shown in the previous section are utilized for the array construction. Fig. 8-23 illustrates the phase array measurement set up. After calibrating a measurement system using a standard gain horn antenna in anechoic chamber, the phased array including phase shifter and power divider is placed inside of the anechoic antenna chamber, and connected to a logic converter. The logic converter is also connected to DC power supply and a computer for phase shifter control. Then, phase of the each phase shifter is measured, where the phased array is fixed at boresight direction. When measuring the output phase of each phase shifter, only the phase shifter under the test is on-state. The other phase shifters should be off-state. For X-band operation from 8 to 12 GHz, the output phase of each phase shifter is measured at 10 GHz, which is the center frequency of the bandwidth. From the phase measurement of each phase shifter for different phase states, Table 8-1 can be obtained. These phases in Table 8-1 present the phase at the corresponding each antenna element. As shown in Fig. 8-21, the phase variations of the phase shifter are linear to the frequencies. Thus, the measured output phase at a single frequency could be used within the operating bandwidth. The measured output phases in Table 8-1 can favorably be utilized to determine the progressive phase difference of the array elements.

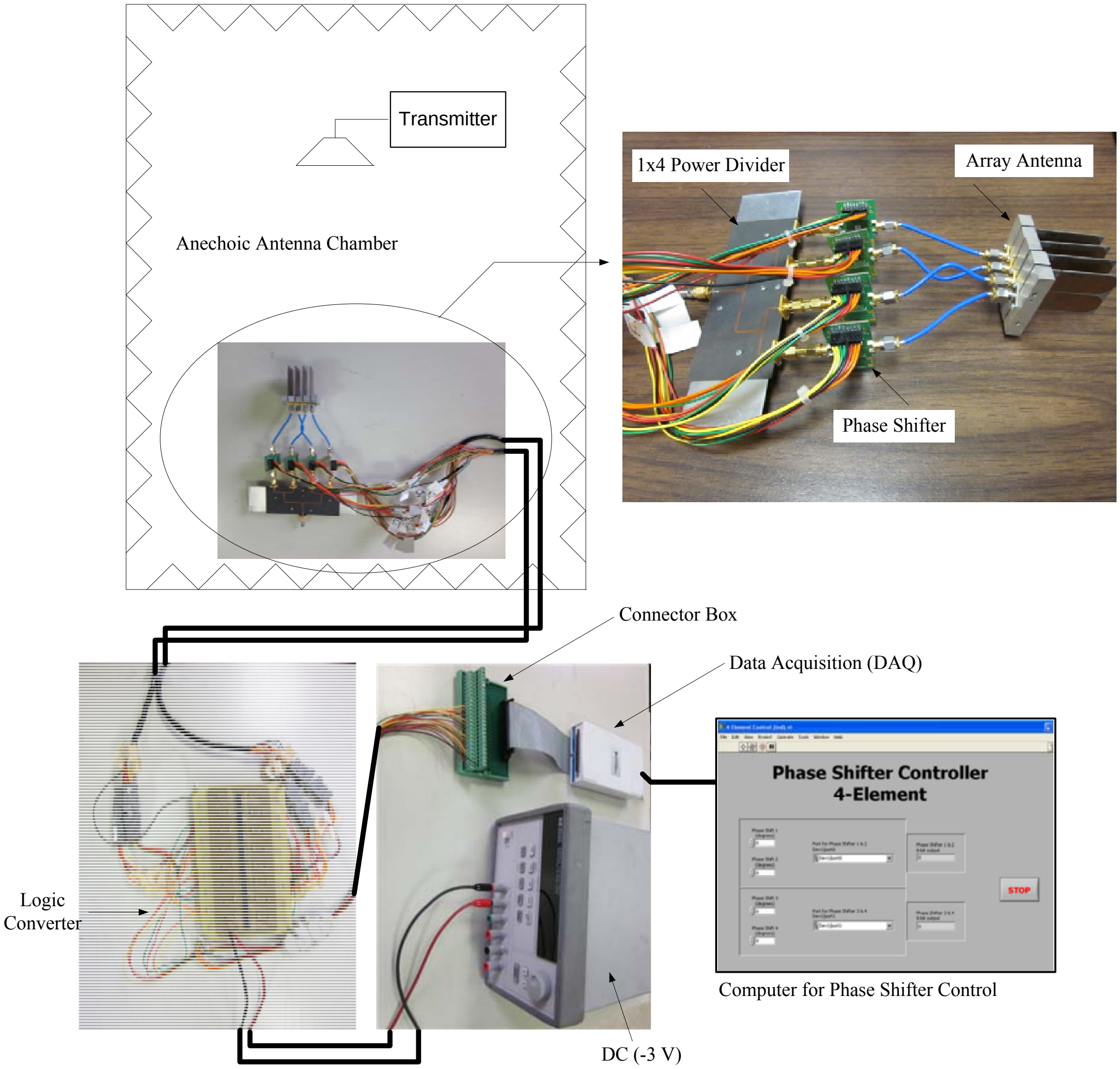

Fig. 8-23. Phased array measurement set up.

Fig. 8-24 shows the measured radiation patterns of the phased array, where the progressive phase difference is 0 º by selecting phase shifter 1= state 10, phase shifter 2= state 7, phase shifter 3= state 7, and phase shifter 4= state 7. Fig. 8-25 presents the measured radiation patterns of the phased array, where the progressive phase difference is 40 º by selecting phase shifter 1= state 12, phase shifter 2= state 7, phase shifter 3=

state 9, and phase shifter 4= state 12. From the expression in (8.11), the progressive phase shift of Φ=40º and *d*=10 mm result in the array's scanning angle of 19.5 º at 10 GHz. Fig. 8-26 presents the measured radiation patterns of the phased array, where the progressive phase difference is -50 º by selecting phase shifter 1= state 4, phase shifter 2= state 10, phase shifter 3= state 8, and phase shifter 4= state 6. From the expression in (8.11), the progressive phase shift of Φ=-50º and *d*=10 mm result in the array's scanning angle of -24.6 º at 10 GHz. The measured radiation patterns in the Figs. 8-24, 25, and 26 show good agreement to the expected results.

TABLE 8-1
MEASURED OUTPUT PHASE OF EACH PHASE SHIFTER AT 10 GHZ

State	Phase shifter 1	Phase shifter 2	Phase shifter 3	Phase shifter 4
State1 (0º)	127	-108	-120	-138
State2 (22.5º)	143	-83	-95	-122
State3 (45º)	158	-53	-62	-100
State4 (67.5º)	172	-23	-28	-55
State5 (90º)	-173	13	12	-10
State6 (112.5º)	-156	35	30	27
State7 (135º)	-148	59	57	65
State8 (157.5º)	-128	75	72	80
State9 (180º)	-94	103	97	105
State10 (202.5º)	-60	120	112	120
State11 (225º)	-15	135	127	132
State12 (247.5º)	27	150	143	140
State13 (270º)	60	170	164	162
State14 (292.5º)	75	-172	-180	175
State15 (315º)	98	-160	-168	-177
State16 (337.5º)	110	-140	-150	-165

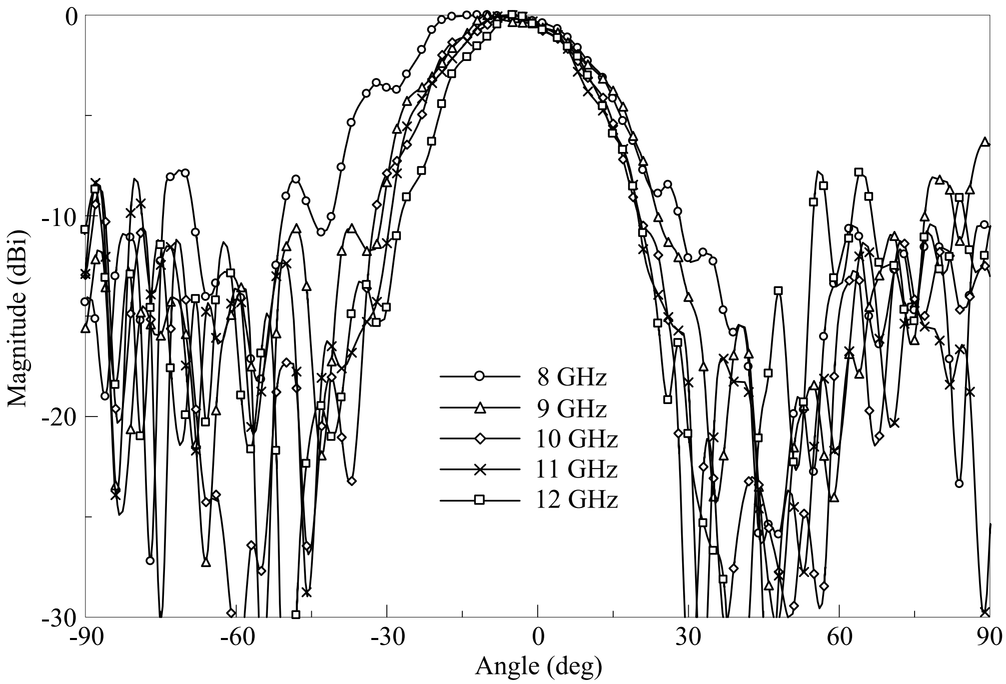

Fig. 8-24. Measured radiation patterns of progressive phase shift=0 º.

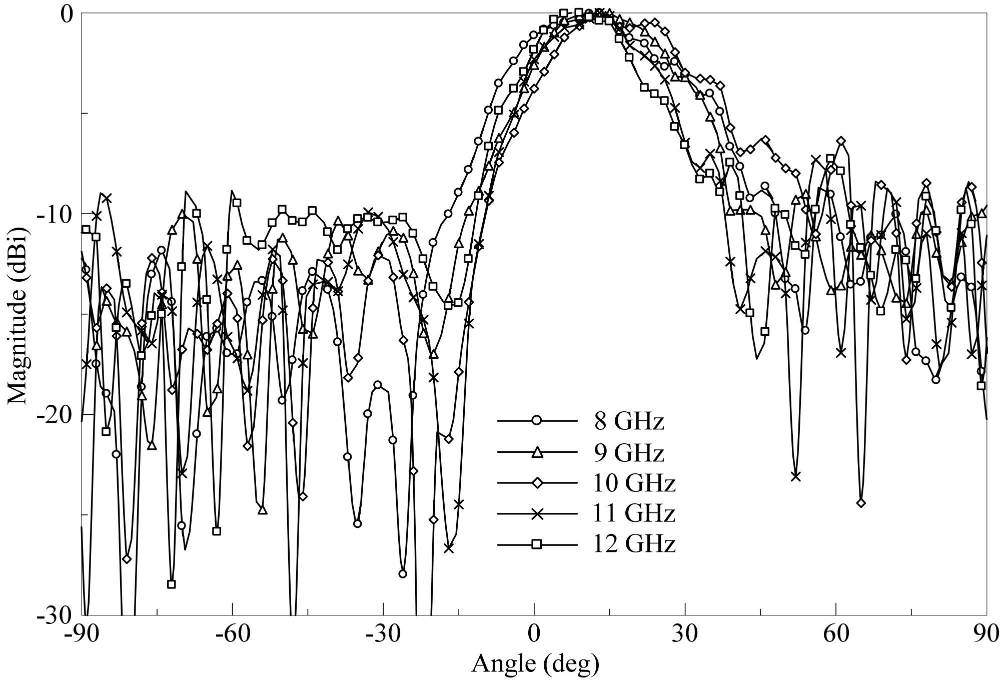

Fig. 8-25. Measured radiation patterns of progressive phase shift=40 º.

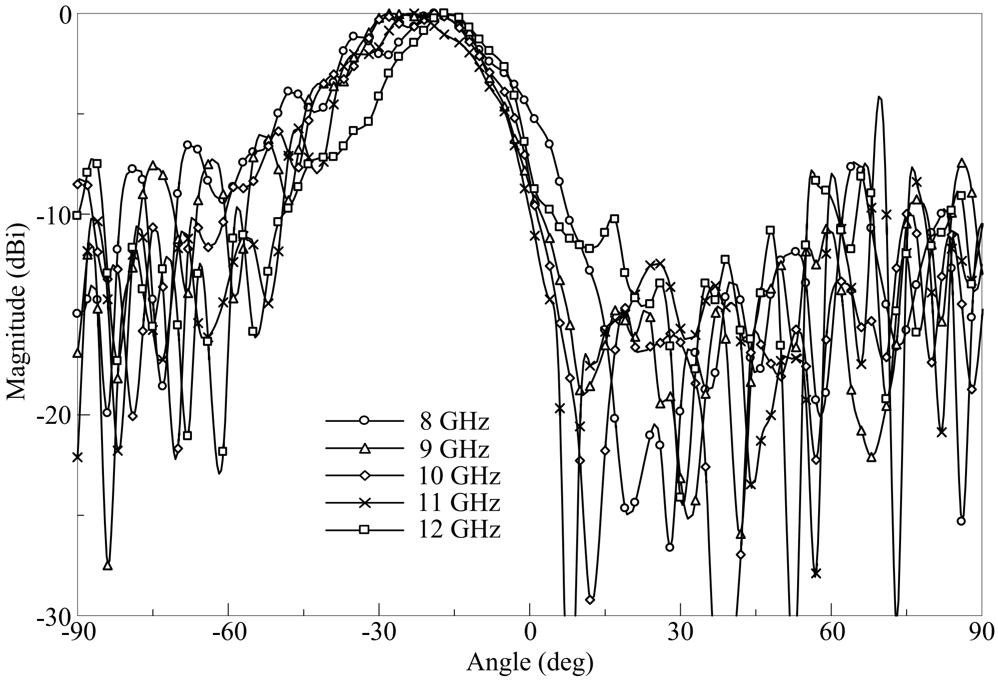

Fig. 8-26. Measured radiation patterns of progressive phase shift=-50 º.

The progressive phase shift of the PET phase shifter is achieved by a mechanical movement of a fixed free type PET cantilever beam. Since the response time of the PET beam is approximately 5 ms, a beam steering speed is slower than the phased array using MMIC phase shifters. However, a fabrication cost of the PET controlled phased array is lower.

CHAPTER IX

CONCLUSIONS

9.1 Summary

This dissertation covers the compact microstrip filter designs, dual-band/triple-band BPF designs, microstrip resonator modeling, and low cost phase array system designs.

In Chapter II, image parameters and inverter theory are reviewed. These fundamental backgrounds are necessitated to understand design concepts of microstrip filters. Impedance and admittance inverters based on the image parameters are commonly utilized for modeling of various coupled type bandpass filters (BPFs). Mathematical expressions and derivations for image impedance, image propagation constant and impedance/admittance inverters are also introduced.

In Chapter III, BPF designs using non-uniform arbitrary image impedances are presented. A parallel coupled line BPF, capacitive gap coupled BPF, and hairpin BPF are designed using the non-uniform arbitrary impedances. Using the proposed design method, a gap distance of parallel coupled line or capacitive gap coupled line can be controlled by a designer. By selecting high image impedance of the coupled lines, the proposed design ultimately results in a wider gap distance in low dielectric substrate.

In Chapter IV, a triple-band BPF (TBBPF) design is introduced. Three shunted parallel *LC* resonators are connected in series to produce a triple-bandpass response. In the proposed TBBPF design, each center frequency and fractional bandwidth (*FBW*) of low, mid, and high bands can separately be controlled. In order to demonstrate the design methodology, simulated results are compared with measured results.

In Chapter V, a coupled type complementary split ring resonator (CSRR) is introduced for a compact direct-coupled bandpass filter (BPF). The proposed unit cell of the resonator consists of two CSRRs, where gaps of outside rings face each other to achieve a strong cross coupling. For an analysis of the coupled CSRR, an equivalent circuit model is discussed and validated through circuit and EM simulations. Based on the coupled CSRR structure, two-/four- pole direct-coupled BPFs are designed, simulated, and measured. Their equivalent circuit models are also presented and validated from comparing simulated and measured results.

Chapter VI presents a dumbbell-shaped slot resonator (DSSR) for miniaturized lowpass filter (LPF) and bandpass filter (BPF) designs. Based on circuit theory and an electromagnetic (EM) simulation, the DSSR's lumped and distributed equivalent circuit models are presented and validated. Using the DSSRs, a miniaturized LPF and BPF are designed, simulated, and measured. The dimensions of the fabricated LPF are $0.27\lambda_g \times 0.17\lambda_g$ at a cutoff frequency of 3.4 GHz, and a measured insertion loss of less than 1 dB and a return loss of greater than18 dB have been achieved. The dimensions of the fabricated BPF are $0.37\lambda_g \times 0.27\lambda_g$ at a center frequency of 7.35 GHz, and an insertion loss of less than 3 dB and a return loss of greater than 15 dB have been achieved. The designed BPF provides a fractional bandwidth (FBW) of 2%. Both simulated and measured results of the designed filters show good agreement. The proposed filters do not utilize stubs or other circuit elements, so the filters are compact in size.

In Chapter VII, the isosceles triangle shaped patch resonator (ITSPR) is investigated using electromagnetic (EM) simulation and a curve fitting method. New design equations which determine the ITSPR dimensions are then proposed. Other equations which estimate fractional bandwidth (FBW), effective dielectric constant, and center frequency of an ITSPR are also introduced. Simple design techniques for a low loss BPF and diplexer using ITSPRs are presented to demonstrate its practical uses in RF/microwave applications.

In Chapter VIII, a phased array for multifunctional radar applications is discussed. As a background of the phased array, a basic linear array theory is reviewed. For a low cost phased array, two phased arrays using piezoelectric transducer (PET) phase shifters and monolithic microwave integrated circuit (MMIC) phase shifters are fabricated and tested in X-band.

9.2 Recommendations for Future Research

In this dissertation, compact microstrip BPFs, a triple-band BPF, and a phased array have been presented. A filter is one of the most essential components in RF/microwave system since it controls overall signal flows within a certain frequency band. Many filters have been developed to meet today's filter requirements including low-insertion loss, compact size, and low cost. For advanced RF/microwave and millimeter wave filter designs, the researches for the following areas are recommended:

filter miniaturization, integration with complementary metal oxide semiconductor (CMOS) circuits, substrate integrated waveguide (SIW) filter, dual-band/triple-band BPF, tunable filters, and reconfigurable filters. These filter designs should satisfy a low loss and high frequency selectivity.

In phased array design, the following subjects are remained for the future researches: a dual-polarized or circularly polarized phased array with electronically scanning capability, a phased array with wide scanning angle, and a phased array with wide bandwidth. Since antenna elements and phase shifters dominantly affects the phased array performance, the researches for the antenna and phase shifter designs are also required.

REFERENCES

[1] G. L. Matthaei, L. Young, and E. M. T. Jones, *Microwave Filters, Impedance-Matching Network, and Coupling Structures*. Norwood, MA: Artech House, 1980.

[2] J.-S. Hong and M. J. Lancaster, *Microstrip Filters for RF/microwave Applications*. New York: John Wiley & Sons, Inc., 2000

[3] K. Chnag and L.-H. Hsieh, *Microwave Ring Circuits and Related Structures.* New York: John Wiley & Sons, Inc., 2004.

[4] S. B. Cohn, "Parallel-coupled transmission-line-resonator filters," *IRE Trans. Microwave Theory Tech.*, vol. MTT-6, pp. 223 - 231, April 1958.

[5] S. B. Cohn, “Direct-coupled-resonator filters,” *Proc. IRE*, vol. 45, no. 2, pp. 187-196, Feb. 1957.

[6] D. Ahn, C. -S. Kim, M. -H. Chung, D. -H. Lee, D. -W. Lew, and H. -J. Hong, “The design of parallel coupled line filter with arbitrary image impedance,” *IEEE MTT-S Int. Microw. Symp. Dig.*, vol. 2, pp. 909-912, June 1998.

[7] H. Gan, D. Lou, and D. Yang, “Compact microstrip bandpass filter with sharp transition bands,” *IEEE Microw. Wireless Compon. Lett.*, vol. 16, no. 3, pp. 107–109, Mar. 2006.

[8] D. Ahn, J. S. Park, C. S. Kim, J. Kim, Y. Qian, and T. Itoh, “A design of the low-pass filter using the novel microstrip defected ground structure,” *IEEE Trans. Microw. Theory Tech.*, vol. 49, no. 1, pp. 86-93, Jan. 2001.

[9] D.-J. Jung and K. Chang, “Low-pass filter design through the accurate analysis of electromagnetic-bandgap geometry on the ground plane,” *IEEE Trans. Microw. Theory Tech.*, vol. 57, no. 7, pp. 1798-1805, Jul. 2009.

[10] T. -N. Kuo, S. -C. Lin, and C. H. Chen, “Compact ultra-wideband bandpass filters using composite microstrip-coplanar waveguide structure,” *IEEE Trans. Microw. Theory Tech.,* vol. 54, no. 10, pp. 3772-3778, Oct. 2006.

[11] D.-J. Jung and K. Chang, “Accurate modeling of microstrip dumbbell shaped slot resonator (dssr) for miniaturized tunable resonator and band-pass filter,” *Progress In Electromagnetics Research C*, vol. 23, pp. 137-150, Aug. 2011.

[12] M. Makimoto and S. Yamashita, “Bandpass filters using parallel coupled stripline stepped impedance resonators,” *IEEE Trans. Microw. Theory Tech.*, vol. 28, no. 12, pp. 1413-1417, Dec. 1980.

[13] J. Bonache , I. Gil , J. García-García and F. Martín, “Novel microstrip band pass filters based on complementary split rings resonators,” *IEEE Trans. Microw. Theory Tech.*, vol. 54, pp. 265-271, Jan. 2006.

[14] D.-J. Jung, J.-K. Lee, and K. Chang, “Wideband banpass filter using microstrip ring,” *Microw. Opt. Technol. Lett.*, vol. 53, no. 1, pp. 154-155, Jan. 2011.

[15] J.-S. Lim, Y.-T. Lee, C.-S. Kim, D. Ahn, and S. Nam, “A vertically periodic defected ground structure and its application in reducing the size of microwave circuits,” *IEEE Microw. Wireless Compon. Lett.*, vol. 12, no. 12, pp. 240-242, Dec. 2002.

[16] D.-J. Jung and K. Chang, “Microstrip diplexer design for X-band RF/microwave front-end applications,” *IEEE Int. Symp. on Antennas Propagat.*, pp.5-7, Aug. 2011.

[17] S.-W. Ting, K.-W. Tam, and R. P. Martins, “Miniaturized microstrip lowpass filter with wide stopband using double equilateral U-shaped defected ground structure,” *IEEE Microw. Wireless Compon. Lett.*, vol. 16, no. 5, pp. 240-242, May 2006.

[18] X.-H. Wang and B.-Z. Wang, “Compact broadband dual-band bandpass filters using slotted ground structure,” *Progress In Electronmagnetics Research*, vol. 82, pp. 151-166, 2008.

[19] K. Ma , K. S. Yeo , J.-G. Ma and M. A. Do, “An ultra-compact hairpin band pass filter with additional zero points,” *IEEE Microw. Wireless Compon. Lett.*, vol. 17, no. 4, pp. 262-264, April 2007.

[20] M. Sagawa, K. Takahashi, and M. Makimoto, “Miniaturized hairpin resonator filters and their application to receiver front-end MIC's,” *IEEE Trans. Microw. Theory Tech.*, vol. 37, no.12, pp. 1991-1997, Dec. 1989.

[21] M.-S. Chung; I.-S. Kim; and S.-W. Yun, “Varactor-tuned hairpin bandpass filter with an attenuation pole,” *Asia-Pacific Microw. Conf. Proc.*, vol. 4, Dec. 2005.

[22] S.-Y. Lee and C.-M. Tsai, “New cross-coupled filter design using improved hairpin resonator,” *IEEE Trans. Microw. Theory Tech.*, vol. 48, no. 12, pp. 2482-2490, Dec. 2000.

[23] H. Miyake, S. Kitazawa, T. Ishizaki, T. Yamada, and Y. Nagatomi, “A miniaturized monolithic dual-band filter using ceramic lamination technique for

dual mode portable telephones," *IEEE MTT-S Int. Microw. Symp. Dig.*, vol. 2, pp. 789–792, June 1997.

[24] L. C. Tsai and C. W. Hsue, "Dual-band bandpass filters using equal-length coupled serial-shunted lines and Z-transform technique," *IEEE Trans. Microw. Theory Tech.,* vol. 52, no. 4, pp. 1111-1117, April 2004.

[25] C. Quendo, E. Rius, and C. Person, "An original topology of dual-band filter with transmission zeros," *IEEE MTT-S Int. Microw. Symp. Dig*., vol. 2, pp. 1093-1096, June 2003.

[26] S. F. Chang, Y. H. Jeng and J. L. Chen, "Dual-band step-impedance bandpass filter for multimode wireless LANs," *IET Electron. Lett., vol.* 40, pp. 38-39, Jan. 2004.

[27] S. Sun and L. Zhu, "Novel design of microstrip bandpass filters with a controllable dual-passband response: description and implementation," *IEICE Trans. on Electron.*, vol. e89-c, no. 2, pp. 197-202, Oct. 2005.

[28] H.-Y. A. Yim and K.-K. M. Cheng "Novel dual-band planar resonator and admittance inverter for filter design and applications," *IEEE MTT-S Int. Microw. Symp. Dig.,* June 2005.

[29] Z. Ma, T. Shimizu, Y. Kobayashi, T. Anada, and G. Hagiwara, "Design and implementation of microwave dual-band bandpass filters using microstrip composite resonators," *Microw. Opt. Technol. Lett.***,** vol. 50, no. 6, pp. 1628-1632 June 2008.

[30] C.-W. Tang and L.-P. Lu, “Design of triple-passband bandpass filter with interdigital resonators,” *IEE Electron. Lett.*, vol. 44, no. 25, pp. 1472-1473, Dec. 2008.

[31] Q.-X. Chu and X.-M. Lin, “Advanced triple-band bandpass filter using tri-section SIR,” *IEE Electron. Lett.*, vol. 44, no. 4, pp. 295-296, Feb. 2008.

[32] S. Luo, L. Zhu, and S. Sun, “Compact dual-mode triple-band bandpass filters usig three pairs of degenerate modes in a ring resonator,” *IEEE Trans. Microw. Theory Tech.*, vol. 59, no. 5, pp. 1222-1229, May 2011.

[33] J. Bonache , I. Gil , J. García-García and F. Martín "Novel microstrip band pass filters based on complementary split rings resonators," *IEEE Trans. Microw. Theory Tech.*, vol. 54, no. 1, pp. 265-271, Jan. 2006.

[34] Q.-L. Zhang, W.-Y. Yin, S. He and L.-S. Wu, "Compact substrate integrated waveguide (SIW) bandpass filter with complementary split-ring resonators (CSRRs)," *IEEE Microw. Wireless Compon. Lett.*, vol. 20, no. 8, pp. 426 - 428, Aug. 2010.

[35] J. C. Liu, D. S. Shu, B. H. Zeng, and D. C. Chang, “Improved equivalent circuits for complementary split-ring resonator-based high-pass filter with C-shaped couplings,” *Proc. IET Microw. Antennas Propagat.*, vol. 2, no. 6, pp. 622-626, Sep. 2008.

[36] P. Mondal, M. K. Mandal, A. Chaktabarty, and S. Sanyal, “Compact bandpass filters with wide controllable fractional bandwidth,” *IEEE Microw. Wireless Compon. Lett.*, vol. 16, no. 10, pp. 540-542, Oct. 2006.

[37] J. D. Baena, J. Bonache, F. Martín, R. M. Sillero, F. Falcone, T. Lopetegi, M. A. G. Laso, J. G.-García, I. Gil, M. F. Portillo, and M. Sorolla, "Equivalent circuit models for split ring resonators and complementary split ring resonators coupled to planar transmission lines," *IEEE Trans. Microw. Theory Tech.*, vol. 53, no. 4, pp. 1451-1461, April 2005.

[38] Y. S. Wu and F. J. Rosenbaum, “Mode chart for microstrip ring resonators,” *IEEE Trans. Microw. Theory and Tech.,* vol. 21, no. 7, pp. 487-489, July 1973.

[39] I. Wolff and N. Knoppik,” Rectangular and circular microstrip disk capacitors and resonators,” *IEEE Trans. Microw. Theory and Tech.,* vol. 22, no. 10, pp. 857-864, Oct. 1974.

[40] A. Gorur, “Description of coupling between degenerate modes of a dual-mode microstrip loop resonator using a novel perturbation arrangement and its dual-mode bandpass filter applications,” *IEEE Trans. Microw. Theory and Tech.,* vol. 52, no. 2, pp. 671-677, Feb. 2004.

[41] T.-Y. Yun and K. Chang, “Uniplanar one-dimensional photonic-bandgap structures and resonators,” *IEEE Trans. Microw. Theory and Tech*., vol. 49, no. 3, pp. 549-553, Mar. 2001.

[42] M. Sagawa, M. Makimoto, and S. Yamashita, “Geometrical structures and fundamental characteristics of microwave stepped-impedance resonators,” *IEEE Trans. Microw. Theory and Tech.,* vol. 45, no. 7, pp. 1078-1085, July 1997.

[43] J. -S. Hong and S. Li, “Theory and experiment of dual-mode microstrip triangular patch resonators and filters,” *IEEE Trans. Microw. Theory and Tech.,* vol. 52, no. 4, pp. 1237-1243, April 2004.

[44] L. -H. Hsieh and K. Chang, “Compact, low insertion-loss, sharp-rejection, and wide-band microstrip bandpass filters,” *IEEE Trans. Microw. Theory and Tech.,* vol. 51, no. 4, pp. 1241-1246, April 2003.

[45] L. -H. Hsieh and K. Chang, “Compact elliptic-function low-pass filters using microstrip stepped-impedance hairpin resonators,” *IEEE Trans. Microw. Theory and Tech.,* vol. 51, no. 1, pp.193-199, Jan. 2003.

[46] M. Matsuo, H. Yabuki, and M. Makimoto, “Dual-mode stepped-impedance ring resonator for bandpass filter applications,” *IEEE Trans. Microw. Theory and Tech.,* vol. 49, no. 7, pp. 1235-1240, July 2001.

[47] J. -S. Park, J. -S. Yun, and D. Ahn, “A design of the novel coupled-line bandpass filter using defected ground structure with wide stopband performance,” *IEEE Trans. Microw. Theory and Tech.,* vol. 50, no. 9, pp. 2037-2043, Sep. 2002.

[48] C. -S. Kim, D. -H. Kim, I. -S. Song, K. M. K. H. Leong, T. Itoh, and D. Ahn, “A design of ring bandpass filters with wide rejection band using DGS and Spur-line coupling structures,” *IEEE MTT-S Int. Microw. Symp. Dig.*, June 2005.

[49] K. Chnag, *Microwave solid-state circuits and applications.* New York: John Wiley & Sons, Inc., 1994.

[50] A. Gopinath, “Maximum Q-factor of microstrip resonators,” *IEEE Trans. Microw. Theory Tech.*, vol. 29, no. 2, pp. 128-131, Sep. 1981.

[51] J. Sor, Y. Qian, and T. Itoh, "A novel low-loss slow-wave CPW periodic structure for filter applications," *IEEE MTT-S Int. Microw. Symp. Dig.*, vol. 1, pp. 307-310, May, 2001.

[52] Y. Rong, K. A. Zaki, J. Gipprich, M. Hageman, and D. Stevens, "LTCC wide-band ridge-waveguide bandpass filters," *IEEE Trans. Microw. Theory and Tech.*, vol. 47, no. 9, pp. 1836-1840, Sep. 1999.

[53] H. Gan, D. Lou, and D. Yang, "Compact microstrip bandpass filter with sharp transition bands," *IEEE Microw. Wireless Compon. Lett.*, vol. 16, no. 3, pp. 107–109, Mar. 2006.

[54] T. -N. Kuo, S. -C. Lin, and C. H. Chen, "Compact ultra-wideband bandpass filters using composite microstrip-coplanar waveguide structure," *IEEE Trans. Microw. Theory and Tech.*, vol. 54, no. 10, pp. 3772-3778, Oct. 2006.

[55] A. Görür and C. Karpuz, "Miniature dual-mode microstrip filters," *IEEE Microw. Wireless Compon. Lett.*, vol. 17, no. 1, pp. 37–39, Jan. 2007.

[56] P. –H. Deng, Y. –S. Lin, C. –H. Wang, and C. H. Chen, "Compact microstrip bandpass filters with good selectivity and stopband rejection," *IEEE Trans. Microw. Theory and Tech.*, vol. 54, no. 2, pp. 533-539, Feb. 2006.

[57] S. B. Cohn, "Parallel-coupled transmission-line resonator filters," *IRE Trans. Microw. Theory and Tech.*, vol. MTT-6, pp. 223-231, Apr. 1958.

[58] C. Nguyen and K. Chang, 'Design and performance of millimeter-wave end-coupled bandpass filters," *Int. Journal of Infrared and Millimeter Waves*, vol. 6, no. 7, pp. 497-509, July 1985.

[59] B. Strassner and K. Chang, “Wide-band low-loss high-isolation microstrip periodic-stub diplexer for multiple-frequency applications,” *IEEE Trans. Microw. Theory and Tech.*, vol. 49, no. 10, pp. 1818-1820, Oct. 2001.

[60] S. Hong and K. Chang, “A 10-35-GHz six-channel microstrip multiplexer for wide-band communication systems,” *IEEE Trans. Microw. Theory and Tech.*, vol. 54, no. 4, pp. 1370-1378, April 2006.

[61] R. R. Mansour, “Design of superconductive multiplexers using single-mode and dual-mode filters,” *IEEE Trans. Microw. Theory and Tech.*, vol. 42, no. 7, pp. 1411-1418, July 1994.

[62] C. Wang and K. Chang, “Microstrip multiplexer with four channels for broadband system applications,” *Int. Journal of RF Microwave CAE 11*, pp. 48-54, Nov. 2001.

[63] B. Strassner and K. Chang, “New wide-band DC-block cymbal bandpass filter,” *IEEE Trans*. Microw. *Theory and Tech.*, vol. 50, no. 5, pp. 1431-1432, May 2002.

[64] J. Helszajn and D. S. James, “Planar triangular resonators with magnetic walls,” *IEEE Trans. Microw. Theory and Tech.*, vol. 26, no. 2, pp. 95-100, Feb. 1978.

[65] R. Azadegan and K. Sarabandi, “Miniature high-Q double-spiral slot-line resonator filters,” *IEEE Trans. Microw. Theory and Tech.*, vol. 52, no. 5, pp. 1548-1557, May 2004.

[66] K. Chang, *RF and Microwave Wireless Systems*. New York: John Wiley & Sons, Inc., 2000.

[67] R. E. Collin, Foundations for Microwave Engineering, McGraw-Hill, New York, 1st ed., 1996, 2nd ed., 1992.

[68] M. Skolnik, Ed., Radar Handbook, 2nd ed., McGraw-Hill, New York, 1990, Ch. 7.

[69] T.-Y. Yun and K. Chang, "A low-cost 8 to 26.5 GHz phased array antenna using a piezoelectric transducer controlled phase shifter," *IEEE Trans. Antennas Propagat.*, vol. 49, no. 9, pp. 1290-1298, Sep. 2001.

[70] T.-Y. Yun, C. Wang, P. Zepeda, C. T. Rodenbeck, M. R. Coutant, M. L. Li, and K. Chang, "A 10- to 21- GHz, low-cost, multifrequency, and full-duplex phased-array antenna system," *IEEE Trans. Antennas Propagat.*, vol. 50, no. 5, pp. 641-650, May 2002.

[71] C. T. Rodenbeck, S.-G. Kim, W.-H. Tu, M. R. Coutant, S. Hong, M. L. Li, and K. Chang, "Ultra-wideband low-cost phased-array radars," *IEEE Trans. Microw. Theory and Tech.*, vol. 53, no. 12, pp. 3697-3703, Dec. 2005.

[72] S. Hong, S.-G. Kim, M. R. Coutant, C. T. Rodenbeck, and K. Chang, "A multiband, compact, and full-duplex beam scanning antenna transceiver system operating from 10 to 35 GHz," *IEEE Trans. Antennas Propagat.*, vol. 54, no. 2, pp. 359-367, Feb. 2006.

[73] T.-Y. Yun and K. Chang, "Analysis and optimization of a phase shifter controlled by a piezoelectric transducer," *IEEE Trans. Microw. Theory and Tech.*, vol. 50, no. 1, pp. 105-111, Jan. 2002.

APPENDIX A

K INVERTER DERIVATIONS

This section presents mathematical derivations for *K* inverters in Figs. 1-10 (a) and (c). Image parameters of other *K* inverter circuits can also be determined in similar manner.

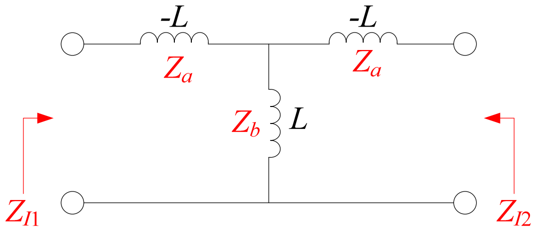

Fig. A-1. *K* inverter shown in Fig. 1-10 (a).

ABCD matrix of Fig. A1:

$$\begin{bmatrix} A & B \\ C & D \end{bmatrix} = \begin{bmatrix} 1 & Z_z \\ 0 & 1 \end{bmatrix} \begin{bmatrix} 1 & 0 \\ \frac{1}{Z_b} & 1 \end{bmatrix} \begin{bmatrix} 1 & Z_z \\ 0 & 1 \end{bmatrix} = \begin{bmatrix} 1+\frac{Z_a}{Z_b} & Z_a\left(1+\frac{Z_a}{Z_b}\right)+Z_a \\ \frac{1}{Z_b} & 1+\frac{Z_a}{Z_b} \end{bmatrix} \tag{A.1}$$

For symmetrical and reciprocal network, image impedance can be written as:

$$Z_{I1} = Z_{I2} = \sqrt{\frac{AB}{CD}} = \sqrt{\frac{BD}{AC}} = \sqrt{Z_a(Z_a + 2Z_b)} \; . \tag{A.2}$$

where Z_a=$-j\omega L$ and Z_b=$j\omega L$. Thus, (A.2) is:

$$Z_{I1} = Z_{I2} = \omega L = K \; . \tag{A.3}$$

where *K* is a real value. (A.3) represents the image impedance K of Fig. 1-10 (a). From (1-24), the propagation constant γ can be rewritten as:

$$\gamma = 2\sinh^{-1}\sqrt{\frac{Z_a}{2Z_b}}\ . \qquad \text{(A.4)}$$

For a lossless network, γ=$j\beta$. Then, (A.4) can be:

$$j\beta = 2\sinh^{-1}\sqrt{\frac{-j\omega L}{j2\omega L}} = j2\sin^{-1}\frac{1}{\sqrt{2}}\ . \qquad \text{(A.5)}$$

Therefore, from (A.5), the image phase constant β of Fig. A-1 has 90º phase shift.

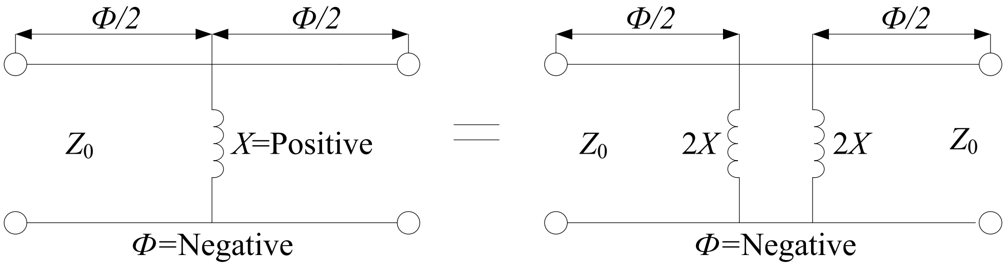

Fig. A-2. *K* inverter shown in Fig. 1-10 (c).

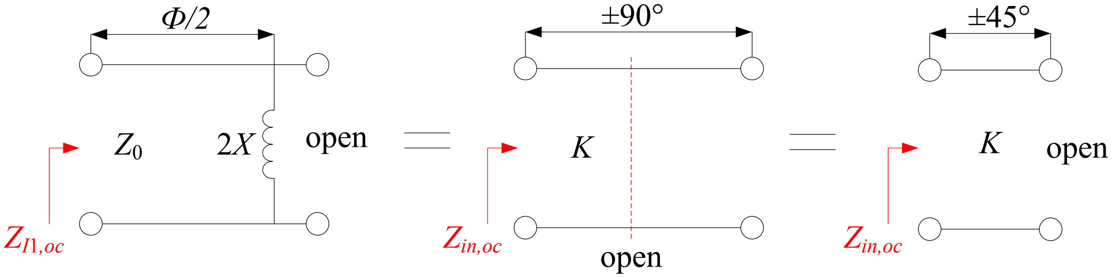

Fig. A-3. Equivalent circuits of Fig. A-2 and quarter-wavelength line, where circuits are cut in half and remained as open.

Fig. A-2 illustrates *K* inverter circuit in Fig. 1-10 (c). Fig. A-3 presents equivalent circuit models of Fig. A-2 and a quarter-wavelength line, where both circuits are cut in half and remained as open circuits. Because impedance inverters produce 90º phase shift and has image impedance K, they can simply be modeled as a transmission line where the line length is a quarter-wavelength and the characteristic impedance is K.

From Fig. A-3, image impedance $Z_{I1,oc}$ and input impedance of open circuited transmission line $Z_{in,oc}$ can be determined as:

$$Z_{I1,oc} = Z_0 \frac{j2X + jZ_0 \tan\left(\frac{\phi}{2}\right)}{Z_0 + j(j2X)\tan\left(\frac{\phi}{2}\right)} = jZ_0 \frac{2X + Z_0 \tan\left(\frac{\phi}{2}\right)}{Z_0 - 2X \tan\left(\frac{\phi}{2}\right)} \quad . \tag{A.6}$$

$$Z_{in,oc} = -jK \cot(45°) = -jK \quad . \tag{A.7}$$

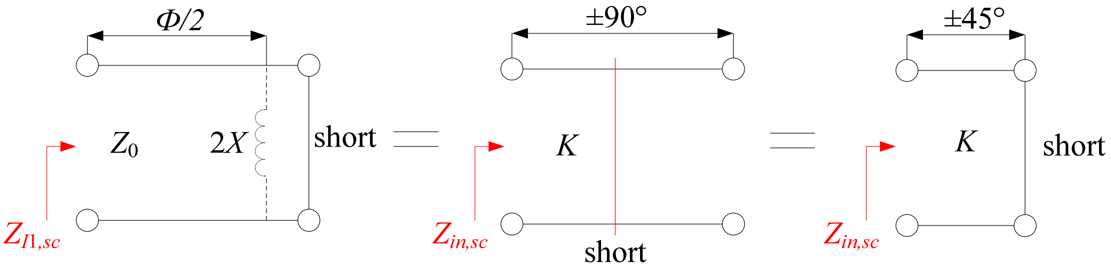

Fig. A-4. Equivalent circuits of Fig. A-2 and quarter-wavelength line, where circuits are cut in half and remained as short.

Fig. A-4 presents equivalent circuit models of Fig. A-2 and a quarter-wavelength line, where both circuits are cut in half and remained as short circuits. From Fig. A-4, image impedance $Z_{I1,sc}$ and input impedance of open circuited transmission line $Z_{in,sc}$ can be determined as:

$$Z_{I1,sc} = jZ_0 \tan\left(\frac{\phi}{2}\right) \quad . \tag{A.8}$$

$$Z_{in,sc} = jK \tan(45°) = jK \quad . \tag{A.9}$$

From (A.8) and (A.9), image impedance of the inverter in Fig. 1-10 (c) can be found as:

$$K = Z_0 \tan(\frac{\phi}{2}) \ . \tag{A.10}$$

From (A.6), (A.7), and (A.10),

$$jZ_0 \frac{2X + Z_0 \tan\left(\frac{\phi}{2}\right)}{Z_0 - 2X \tan\left(\frac{\phi}{2}\right)} = -jK = -jZ_0 \tan\left(\frac{\phi}{2}\right) \ . \tag{A.11}$$

Letting $2X/Z_0$=tanθ in (A.11) lead to:

$$\frac{\tan\theta + \tan\left(\frac{\phi}{2}\right)}{1 - \tan\theta \tan\left(\frac{\phi}{2}\right)} = \tan(\theta + \frac{\phi}{2}) = -\tan\left(\frac{\phi}{2}\right) \ . \tag{A.12}$$

where $\tan(\alpha \pm \beta) = \frac{\tan\alpha \pm \tan\beta}{1 \mp \tan\alpha \tan\beta}$ has been applied in (A.12).

Thus, $\theta + \phi/2 = -\phi/2$ and $\theta = -\phi$. As a result, the assumption, $2X/Z_0$=tanθ can be:

$$\phi = -\tan^{-1}\left(\frac{2X}{Z_0}\right) \ . \tag{A.13}$$

VITA

Dong Jin Jung was born in Asan, Korea. He received his B.S. degree in 2007 from Soonchunhyang University, South Korea. In the fall semester of 2007, he started his graduate study in the Electrical and Computer Engineering Department of Texas A&M University, USA, and received his M.S. in 2009. During the summer of 2008, he also worked at the Engineering Laboratory of MIMIX BROADBAND, Houston, Texas as a student intern. In the fall semester of 2009, he started his Ph. D study in the Electrical and Computer Engineering Department of Texas A&M University, USA. Since 2011, he has served as Lab Manager in the Electromagnetics and Microwave Laboratory, Texas A&M University. His present research interest includes microwave and millimeter-wave devices and circuits, microwave integrated circuits, antennas, phased array, microwave power transmission. Dong-Jin Jung's present address is 214 Zachry Engineering Center, College Station, TX 77843-3128. His email address is dongjin3558@tamu.edu.